U. S. DEPARTMENT OF THE INTERIOR
U. S. GEOLOGICAL SURVEY

MINERALOGICAL AND MICROSTRUCTURAL INVESTIGATIONS OF CORE SAMPLES FROM THE VICINITY OF THE GREAT SUMATRAN FAULT, INDONESIA

by

Diane E. Moore[1]

Open-File Report 97-694

[1]U. S. Geological Survey
345 Middlefield Road MS/977
Menlo Park, California 94025

Introduction

This paper is a summary of petrographic investigations of core samples from geothermal prospect wells drilled by Unocal in the vicinity of the Great Sumatran fault zone, Sumatra, Indonesia. The overall purpose of the project was to investigate the interplay between the geothermal system and the active fault zone. Specific topics to be considered can be separated into two general groups:

Geothermal Research

- Changes in mineralogy with location, depth, and time
- Dissolution versus precipitation
- What does the mineralogy say about fluid pressures, fluid compositions, and the amount of flow?
- Is fluid flow channeled within the fault zone or to the side?
- Episodicity of hydrothermal alteration and its relation to fracture history

Earthquake Research

- Determination of current stress orientations and sense of shear
- Any changes in fracture orientation with time or proximity to the fault?
- Dilational versus compressional features

Obviously, the two groups of topics are interrelated. Knowledge of the controls of faulting on fluid flow is important for siting future drilling operations. In addition, recent models of earthquake cycles place considerable emphasis on the effects of fluid flow along faults, in particular the development of mineral seals through hydrothermal reactions and their subsequent effects on fluid pressure and effective stress.

Given the limitations on time and on the scope of the investigation, some of the specific goals listed above are treated much less thoroughly in this report than others. The fault-related research described here should be considered as the preliminary results of an on-going study.

Geologic Background

The island of Sumatra is situated along the southwest margin of the Sundaland cratonic block. The oldest well-dated rocks are Late Carboniferous continental shelf and platform facies sedimentary deposits, now somewhat metamorphosed (Hamilton, 1979). As suggested by numerous workers, Sumatra may have formed part of a convergent plate margin since the early Mesozoic and perhaps as early as the Permian. Evidence supporting this hypothesis has been provided by the work of McCourt et al. (1996) on the plutonic rocks of Sumatra. They found evidence for five major periods of plutonic activity between Late Triassic and Pliocene time and possibly an additional event in the Permian. All of the examined granitoids are calc-alkaline, subduction-related bodies that may correlate with rocks in Thailand and Burma. The older belts of plutonic rocks all have a roughly northwest-southeast trend sub-parallel to the present magmatic arc (Fig. 1a), suggesting that the configuration of this part of the subduction system has remained approximately the same throughout its history. The various breaks in plutonic activity are attributed to collision and accretion events, changes in the direction of plate convergence, or changes in the rate of subduction (McCourt et al., 1996).

Widespread andesitic volcanism and plutonism associated with the present period of subduction were established in Sumatra by Late Oligocene time, following a mid-Oligocene collision event (McCourt et al., 1996). The current phase of subduction involves northward motion of the Indian Ocean plate at about 6-7 cm per year (Hamilton, 1979). Subduction is oblique (≈50–65°; Simandjuntak and Barber, 1996) along this part of the Java trench (Fig. 1a), and Fitch (1972) was the first to propose the widely accepted hypothesis that the plate motion is partitioned into a component of convergence and a component of strike-slip faulting. The Great Sumatran fault zone is a right-lateral strike-slip fault trending northwest-southeast along the axis of the island of Sumatra, coincident with the magmatic arc (Fig. 1a). Eleven active volcanoes occur along the fault (Hochstein and Sudarman, 1993). The slip rate on the fault increases from ≤10 mm/yr in the south to 28 mm/yr in the north (Bellier et al., 1991;

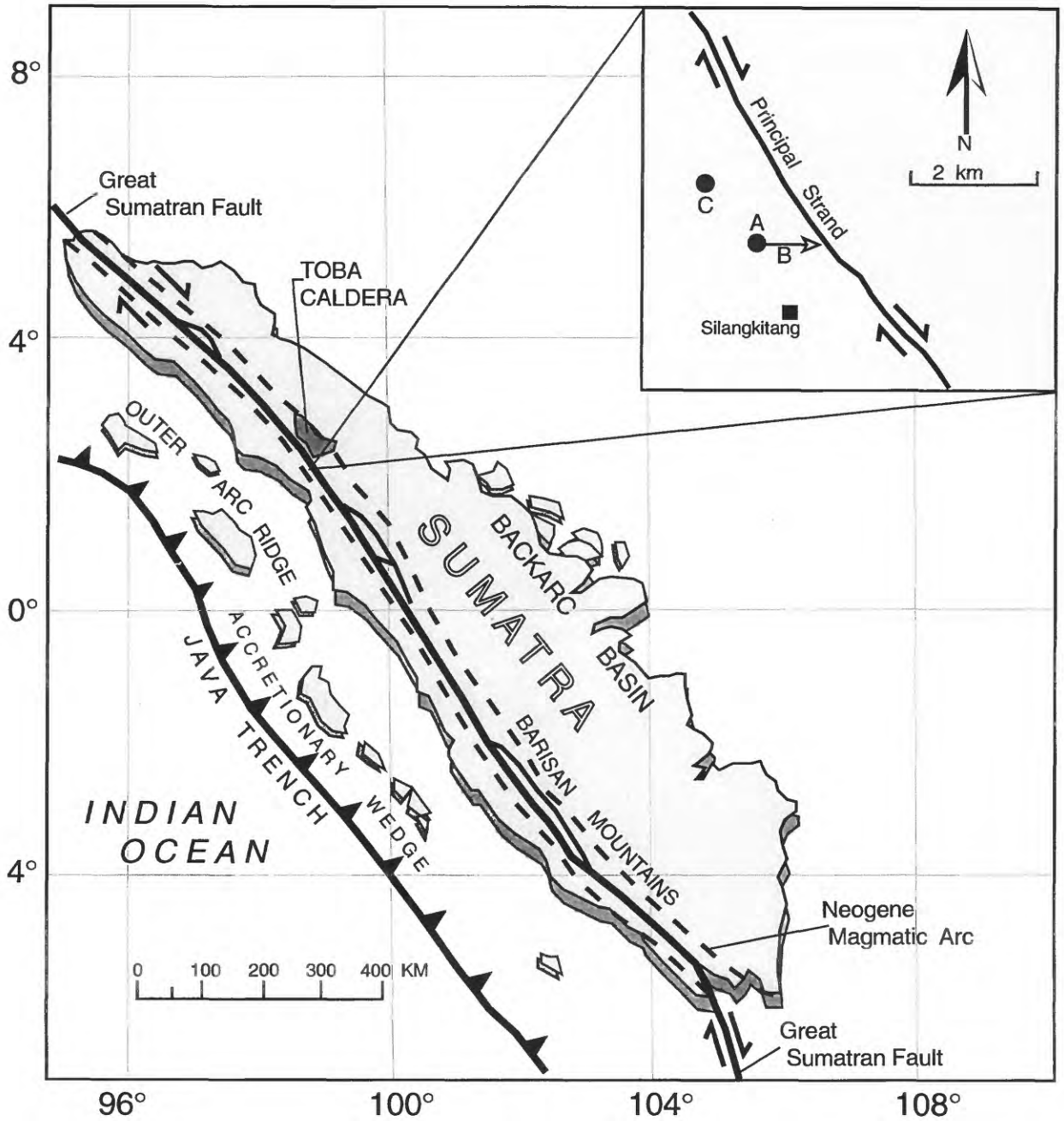

Figure 1a. Tectonic setting of Sumatra. The Great Sumatran fault zone lies within the active magmatic arc along the entire length of the island (map modified from Hamilton, 1979; position of the Great Sumatran fault from Simandjuntak and Barber, 1996). The locations of the three wells investigated in this study relative to the principal strand of the Great Sumatran fault are indicated in the inset. Wells A and C were drilled nearly vertically, and they are represented by the small circles. Well B was drilled at about a 60° angle from the position of well A towards the principal strand of the fault, in the direction indicated by the arrow.

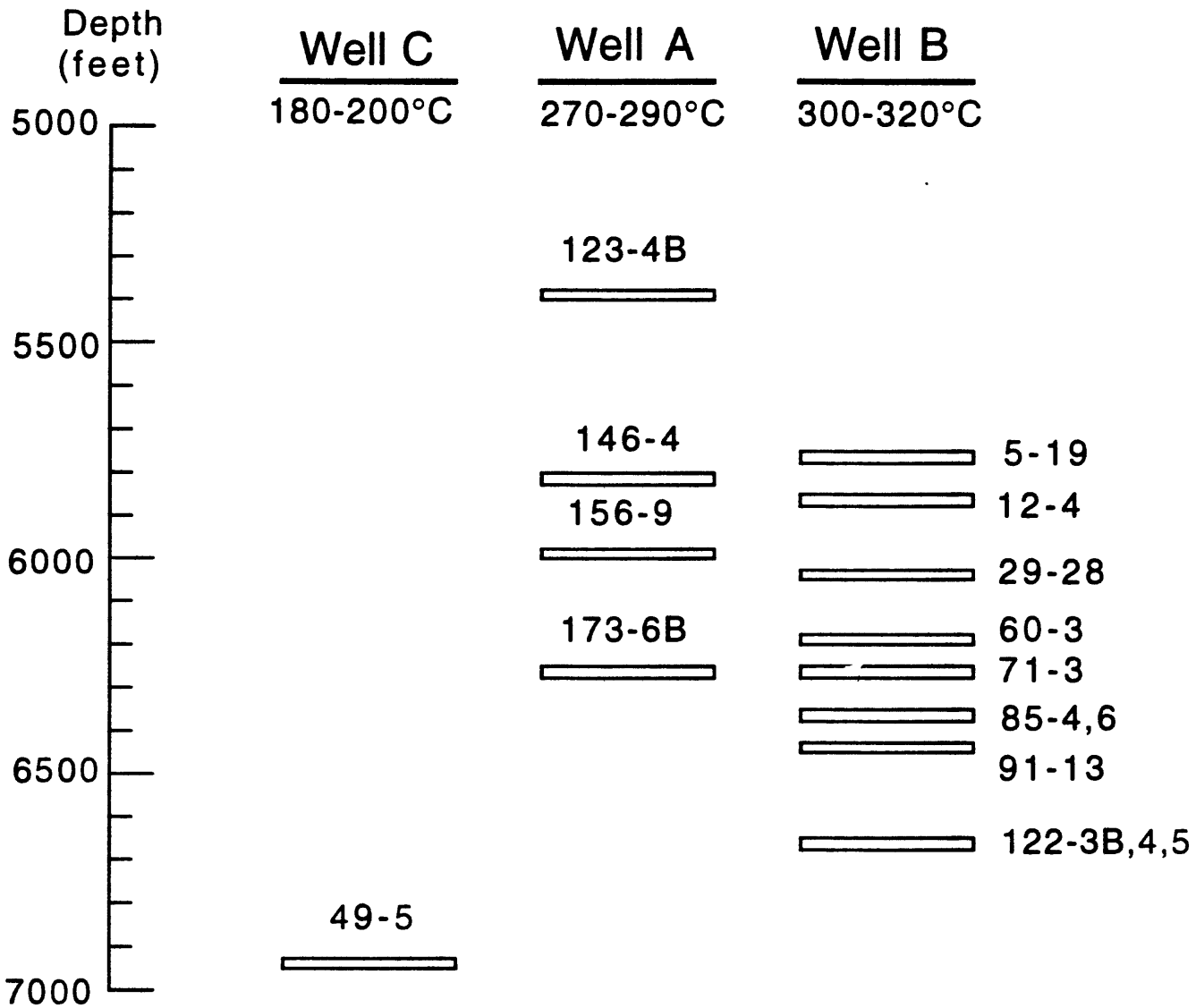

Figure 1b. Depth intervals and measured temperatures of the thirteen core samples examined in this study.

Sieh et al., 1994). Based on the analysis of well bore breakouts from wells in the central and southern oil fields of Sumatra, Mount and Suppe (1992) determined that the maximum horizontal stress direction is oriented at a large angle (70–80°) to the strike of the fault. According to Mount and Suppe (1992), such stress orientations imply that a low shear stress is acting on the fault, similar to the situation proposed for the San Andreas fault (however, for an alternative view of relative fault strength see Tikoff and Teyssier, 1994).

Both compressional and extensional features may have formed within the Great Sumatran fault zone at different times. Mid-Miocene movement on the fault was transpressive, coincident with uplift of the Barisan Mountains (Simandjuntak and Barber, 1996), which the fault traverses (Fig. 1a). In contrast, Pleistocene movement was at least locally transtensional, leading to the formation of a series of lake-filled basins in an array of right-stepping fault traces (see Fig. 4 of Simandjuntak and Barber, 1996). The present main trace of the fault is associated with a series of graben-like structures, and Hamilton (1979) has suggested that the Barisan Mountains may be undergoing extension perpendicular to the volcanic arc. However, based on recent earthquake activity, Simandjuntak and Barber (1996) infer that transpressional movement may be occurring in the northern and central parts of Sumatra.

Gunderson et al. (1995) described the geology of a roughly 15 x 63 km section straddling the Great Sumatran fault in northern Sumatra, that comprises the Unocal contract area. The examined core samples come from holes drilled near Silangkitang, in the northern half of the section (Fig. 1a). The basement rocks include Upper Paleozoic quartzite, phyllite, and limestone, and Gunderson et al. (1995) suggested that these rocks may be the local reservoir rock for the geothermal systems. Some granitic and hornfelsic intrusions of possible Mesozoic or Early Tertiary age may also be present, evidenced by inclusions occurring in some of the volcanic rocks. The surface rocks are principally Quaternary arc volcanics ranging in age from 0.1 to 1.8 Ma (see Table 1 of Gunderson et al., 1995). The volcanic rocks include lava flows and breccias, silicic domes, and rhyolite to basaltic-andesite ash flow and airfall tuffs. No currently active volcanoes are found in the contract area, but Gunderson et al. (1995)

identified four groups of active geothermal features that may each be associated with a different Quaternary eruptive center. The three wells examined in this study (Fig. 1a) were drilled in the 1 x 4 km area of hydrothermal activity located along the Great Sumatran fault in the vicinity of Silangkitang. The surface hydrothermal features observable near Silangkitang include fumaroles and boiling springs. Analyses of fluids collected from this hydrothermal center (see Table 3 of Gunderson et al., 1995, and also Hochstein and Sudarman, 1993) indicate that the fluids rose rapidly from a high-temperature reservoir; geothermometers based on cation concentrations yield a temperature of 260–270°C for those waters (Gunderson et al., 1995).

Scope of Study

Thirteen core samples from three wells were examined; their depths and the corresponding temperature ranges at those depths are indicated in Figure 1b. All of the core samples were logged as rhyolite ash-flow tuffs. The well C and A drillholes are located about 1 km from the principal strand of the Great Sumatran fault. Both wells were drilled nearly vertically; well C has an 80° dip and well A an 87.5° dip. Drilling of well B began at the site of well A, but this hole was drilled eastwards (S84°E) at a 57–65° angle (Fig. 1b). The deepest core sample examined from well B (122-3,4,5; Fig. 1b) may have been located within tens of meters of the principal strand of the Great Sumatran fault. In addition, the shallowest well B sample (5-19; Fig. 1b) was collected about 40 meters east of a subsidiary fault strand.

One to three polished thin sections were prepared from each core sample; most of the sections cut one or more of the fractures visible on the core surface. All of the sections are oriented perpendicular to the axis of the core sample such that the viewer is looking downwards into the well. The polished sections were examined with a petrographic microscope and a scanning electron microscope equipped with a high-resolution backscattered electron (BSE) detector and an energy dispersive X-ray (EDX) spectrometer, the latter for qualitative

determinations of element abundances. At least one thin section from each core sample was examined by SEM techniques. Quantitative mineral analyses were obtained from selected thin sections with an automated, 5-channel JEOL model 8900L electron microprobe, at operating conditions of 15 kV accelerating voltage, 25 μA beam current, and beam diameters of 10 to 15 μm diameter. Natural and synthetic minerals were used both for initial standardization and as internal standards during analysis.

The report consists of two main sections. The first section covers the mineralogical investigations, which were focused on the hydrothermal assemblages, and the second section deals with the fracture data and the microstructural studies.

Mineralogical Investigations

Hydrothermal Minerals

The minerals in Table 1 are all considered to be part of the hydrothermal assemblage. Many are found in veins, but several occur as replacements of igneous feldspars or mafic minerals (biotite and amphibole). The occurrences and compositions of these minerals are described below, and the overall assemblages in different wells are compared with respect to their physical and chemical conditions of crystallization.

Quartz. Quartz is a vein-filling mineral in every piece of core (Table 1). It is the principal mineral deposited on the walls of major well C fractures (Fig. 2a), as well as in the topmost well B core sample (5-19). Although still abundant at deeper levels in well B, quartz becomes subordinate to adularia in the major veins (Fig. 2b). Narrow quartz veinlets, one or two crystals wide and one to several mm in length, are relatively abundant in well A and C samples; many of the smaller veinlets also contain K-mica.

Calcite. Calcite is as ubiquitous as quartz in the cores (Table 1), and it is even more common than quartz in well A. Its occurrence ranges from narrow, en echelon vein sets to large patches of coarse-grained calcite. Calcite fills cracks and occurs as a patchy replacement of

Table 1. Hydrothermal Mineral Assemblages

Mineral	Well A				Well C
	123-4B	146-4	156-9	173-6B	49-5
Quartz	X	X	X	X	X
Calcite	X	X	X	X	X
Albite	X	X		X	X
Adularia	x			x	x
Epidote					
Allanite	x	x	Tr	x	x
Titanite	X	X	X	X	X
K-Mica	X	X	X	X	X
Chlorite	X	X	x	X	Tr
TiO_2	x			x	x
Hematite		x	x	X	
Anhydrite					
Apatite	x	x	x	x	x
Pyrite		Tr			x
Sphalerite					Tr
Galena	Tr		Tr		Tr
Ilmenite		x	Tr		
Zircon		Tr	x		Tr
Pseudobrookite?			Tr	Tr	

Mineral	Well B							
	5-19	12-4	29-28	60-3	71-3	85-4,6	91-13	122-3B,4,5
Quartz	X	x	X	X	X	X	X	X
Calcite	X	X	X	X	X	X	X	X
Albite		x	X	x	x	x	x	X
Adularia	x	X	X	X	X	X	X	X
Epidote		x	x		x	x	x	x
Allanite		x	x	x	x	x	x	x
Titanite	X	X	X	X	X	X	X	X
K-Mica	X	X		x	x	x	x	x
Chlorite	X	X	X	X	X	X	X	X
TiO_2	Tr		x			Tr	x	
Hematite	x		x		x		Tr	
Anhydrite	X	x	X	X	X	X	X	X
Apatite	Tr	x	x	x	x	x	x	x
Pyrite	X	X	X	X	X	X	X	X
Sphalerite								Tr
Galena		Tr				Tr	Tr	Tr
Ilmenite								
Zircon			x			x	x	
Pseudobrookite?								

X = relatively abundant; x = minor; Tr = only one or two crystals found.

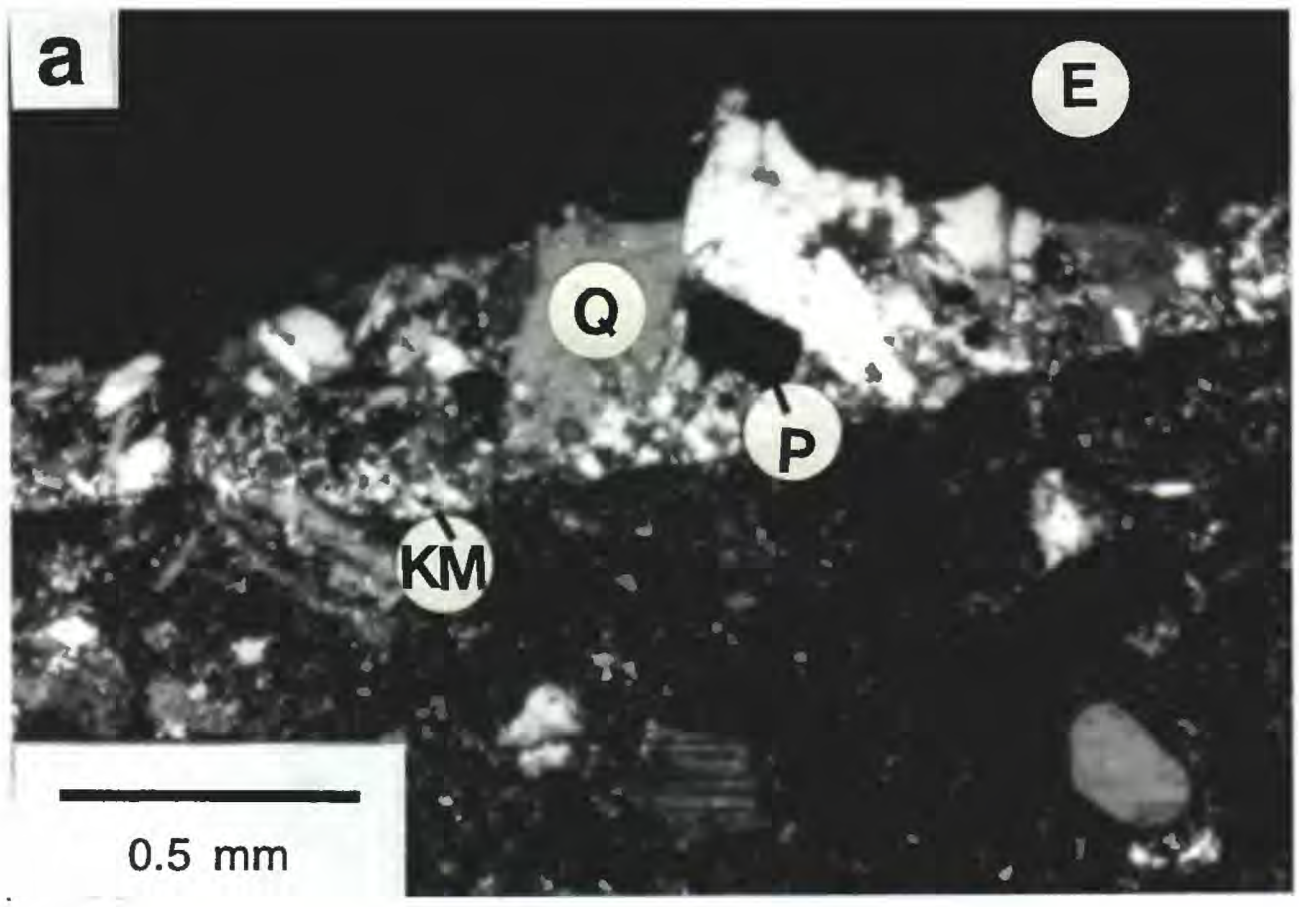

Figure 2. Quartz textures. a) Euhedral quartz (Q) and pyrite (P) crystals in well C vein (49-5). Fine-grained K-mica (KM) extends into the vein from the margins; crossed polarizers. E = epoxy. b) Band of fine-grained adularia (Ad) intergrown with lesser amounts of euhedral quartz in 60-3, well B. Back-scattered electron SEM photograph.

feldspar phenocrysts in the tuffs. Brecciated zones in well A typically are cemented with calcite. Many veins and sheared-looking zones in well A consist of calcite + chlorite + titanite, and this is also a major hydrothermal assemblage of the shallowest well B core samples 5-19 and 12-4. These latter occurrences probably correspond to the green- and white-filled veins visible on the surface of many pieces of core. Calcite becomes progressively less important at deeper levels in well B. In the fragmented parts of well B core samples such as 91-13, in which pieces of tuff are cemented together by fine-grained adularia + quartz assemblages, the calcite occurs in veins that are confined to the interiors of the tuff fragments. Calcite crystals in a major fracture of the lowermost well B sample, 122-3,4,5, have a corroded appearance, and they are partly rimmed by titanite.

Element spectra of calcite obtained during SEM analysis generally have a modest Mn peak, and two microprobe analyses of calcite (one each from well B and well A) yield about 0.25–0.30 wt% Mn and 0.05–0.15 wt% Fe.

K-Feldspar. Hydrothermal K-feldspar, adularia, is overall the predominant vein and replacement mineral in well B core, but it is considerably less important in wells A and C. In well B, its occurrence varies from fine-grained anhedral masses that fill veins in combination with quartz, chlorite, and titanite (Fig. 2b), to medium- to coarse-grained euhedral crystals lining open veins (Fig. 3a). It also occurs with quartz and some chlorite as a patchy replacement of the groundmass. During SEM examination of the well C core, K-feldspar was identified as inclusions in coarse-grained vein quartz and in intergrowths with white mica + allbite + quartz in the fine-grained matted area behind the veins. On the other hand, K-feldspar phenocrysts in well C are partly replaced by albite + K-mica along the rims and internal cracks (Fig. 3b).

K-feldspar textures in well A are characteristically ones of dissolution. Many of the igneous K-feldspar phenocrysts in the well A core samples have been partly dissolved, leaving large internal voids (Fig. 3c). Characteristically, however, the remaining fragments of K-feldspar commonly have euhedral form where they project into the cavities, suggesting some

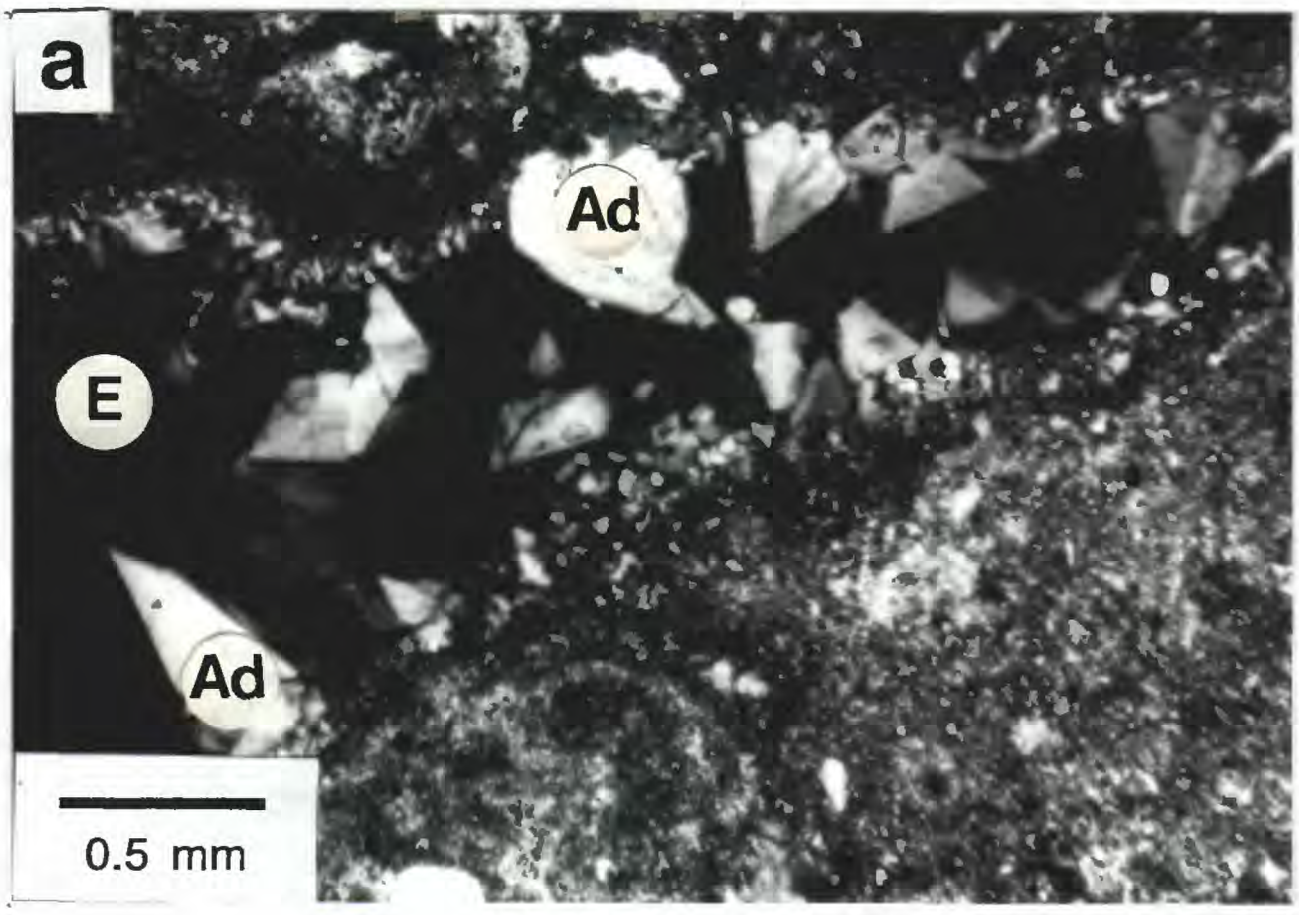

Figure 3. K-feldspar textures. a) Medium-grained, euhedral adularia (Ad) crystals, some of them cracked, extend into open vein in 85-4, well B. Vein walls are lined with fine-grained adularia + quartz; crossed polarizers. E = epoxy.

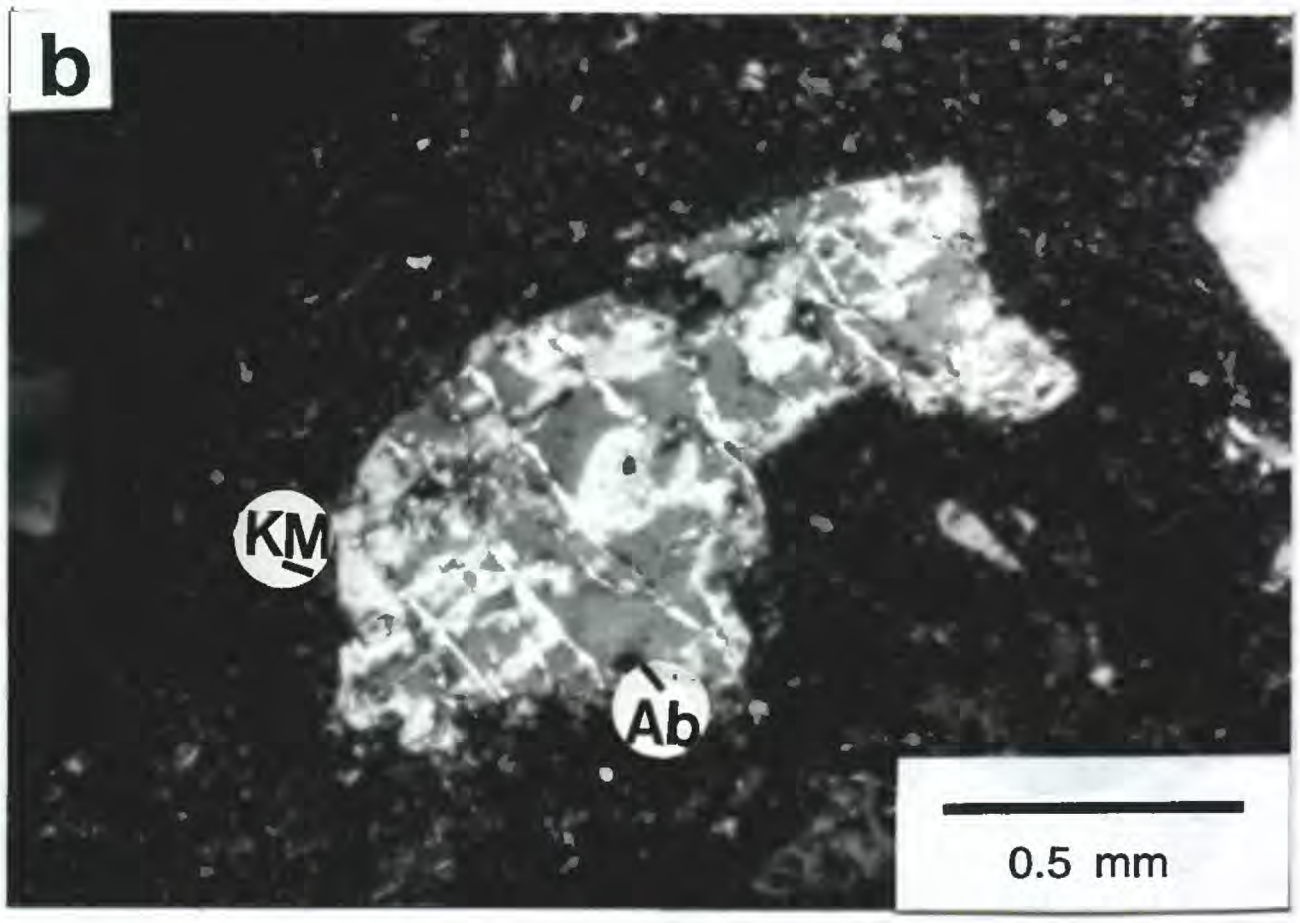

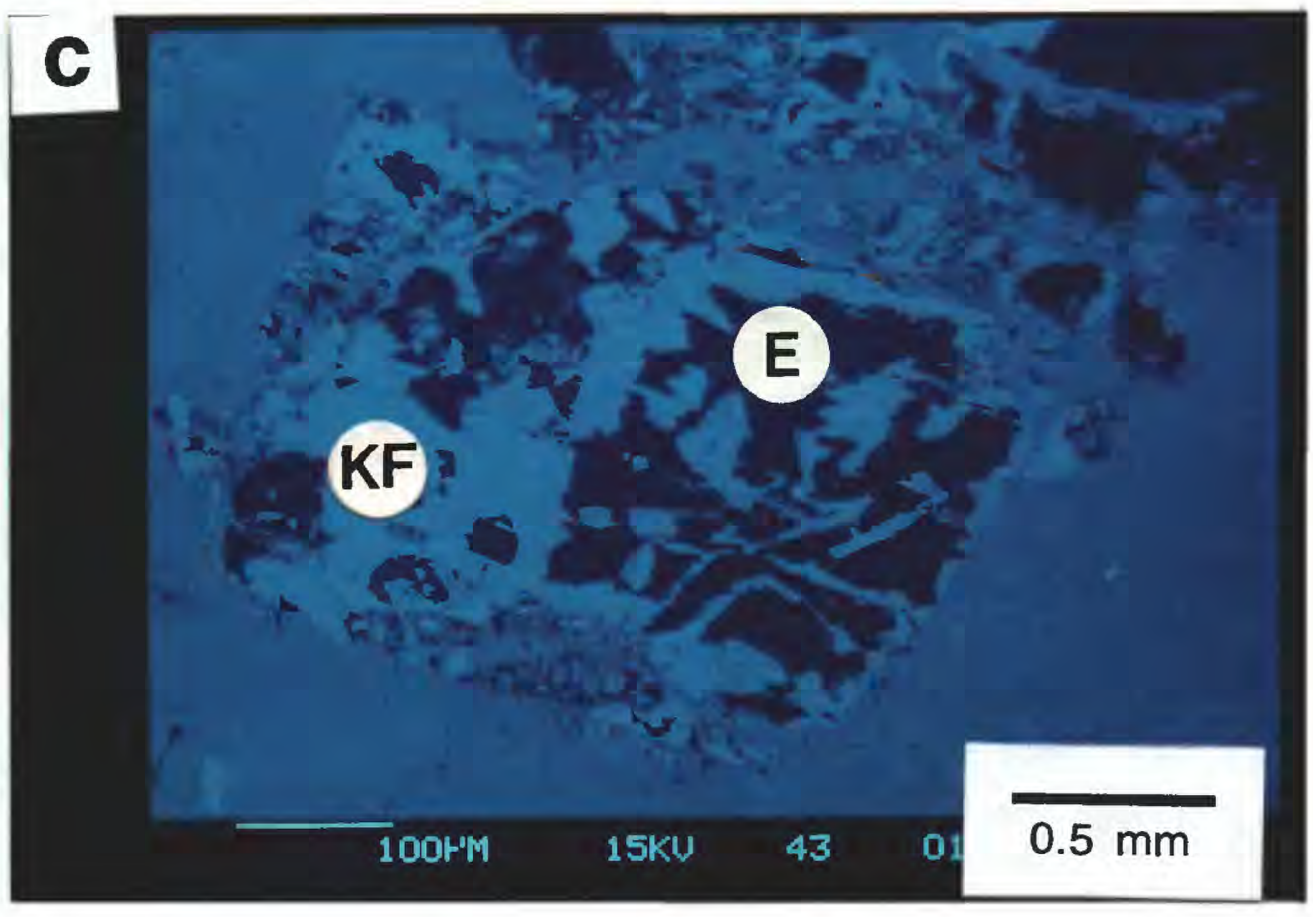

Figure 3, continued. b) K-feldspar phenocryst partly replaced along the margin and interior cracks by K-mica (KM) + albite (Ab) with composition An_{1-6}; crossed polarizers. c) Partly dissolved K-feldspar phenocryst from 123-4B, well A. The remnants of K-feldspar (KF) commonly have euhedral terminations into the void spaces. Back-scattered electron SEM photograph.

recrystallization and/or new growth of the K-feldspar (Fig. 3c). These dissolution features are most abundant in the shallowest well A core sample (123-4B) and least abundant in the deepest one (173-6B).

The igneous K-feldspar composition (Table 2) corresponds to a sodium-rich sanidine ($Ab_{20}Or_{80}$ to $Ab_{30}Or_{70}$) with moderate amounts of barium (≈0.5-1.0 wt% BaO), typical of volcanic K-feldspars. In wells A and B, this Na-rich feldspar is partly altered to a low-Na (Ab_5Or_{95}) composition along veins and recrystallized areas; in well C, all of the analyzed K-feldspar phenocrysts have the low-Na composition. The hydrothermal adularia from well B is nearly identical in composition to the low-Na altered phenocrysts, except that the vein-filling K-feldspars all have <0.1 wt% BaO.

Plagioclase. Hydrothermal plagioclase, usually albite (Table 3), occurs as an alteration product of igneous plagioclase and to a lesser extent as a vein mineral in core from all three wells. Similar to K-feldspar, the plagioclase phenocrysts in well A appear to have been partly dissolved; a phenocryst from 123-4B containing many void spaces is shown in Figure 4a. The crystal remnants along the voids commonly have euhedral terminations, suggesting that they have been recrystallized or are newly crystallized. Voids in plagioclase are less frequently observed in the deeper well A core samples. Plagioclase phenocrysts from well B also show some evidence for partial dissolution; however, most of those voids have been re-filled, giving the crystals a mosaic texture (Fig. 4b). The filling assemblages include aggregates of fine-grained feldspar ± quartz, calcite + chlorite, or chlorite alone. Well C feldspars display modest evidence for such dissolution reactions.

Plagioclase compositions vary considerably from well to well (Table 3). The most calcium-rich phenocrysts are andesines ($An_{40}Ab_{60}$ to $An_{50}Ab_{50}$) from well A samples. Andesine compositions were obtained both from intact phenocrysts and from small fragments of ground-up plagioclase in a narrow sheared zone (see 173-6B analyses in Table 3). In contrast, plagioclases from well B are no more calcic than oligoclase ($An_{\leq 30}$), and all the analyzed well C plagioclase phenocrysts are albite. The well C plagioclase phenocrysts probably

Table 2. K-Feldspar Analyses

	Well A					Well C	
	123-4B	146-4		173-6B		49-5	
		(1)	(2)	(1)	(2)	(1)	(2)
SiO_2	64.86	65.58	64.63	65.33	64.53	64.79	64.90
TiO_2	0.13	0.03	0.01	0.03	0.01	--	0.01
Al_2O_3	18.59	18.92	18.52	18.69	18.47	18.41	18.27
Fe_2O_3	--	0.14	0.03	0.16	0.02	0.01	0.01
MgO		--	--	--	--	--	--
MnO	0.01	0.01	--	0.01	--	0.01	--
CaO	0.10	0.22	--	0.20	--	--	--
Na_2O	0.34	3.61	0.53	3.19	0.46	0.49	0.55
K_2O	16.05	10.93	15.78	11.60	15.71	15.97	16.03
BaO		0.64	0.46	0.82	0.92	0.49	0.12
Total	100.08	100.08	99.96	100.03	100.12	100.17	99.89
Si	2.99	2.99	2.99	2.99	2.99	3.00	3.00
Al^{IV}	0.01	0.01	0.01	0.01	0.01	--	--
Al^{VI}	1.00	1.00	1.00	1.00	1.00	1.00	1.00
Ti	--	--	--	--	--	--	--
Fe^{+3}	--	0.01	--	--	--	--	--
Mg		--	--	--	--	--	--
Mn	--	--	--	--	--	--	--
Ca	0.01	--	--	0.01	--	--	--
Na	0.03	0.32	0.05	0.28	0.04	0.04	0.04
K	0.96	0.64	0.93	0.68	0.93	0.94	0.95
Ba		0.01	0.01	0.01	0.02	0.01	--
# Analyses	2	16	20	12	9	9	8
An	1.0	--	--	1.0	--	--	--
Ab	3.0	33.3	5.1	28.9	4.1	4.1	4.0
Or	96.0	66.7	94.9	70.1	95.9	95.9	96.0

Structural formula calculations assume O = 8.

This Page — 123-4B: crystal intergrown with titanite along large void in groundmass. 146-4: (1) probably represents the igneous K-feldspar composition; (2) altered parts of K-feldspar phenocrysts. 173-6B: (1) high-Na phenocryst composition; (2) altered patches in K-feldspar phenocrysts. 49-5: (1) K-feldspar phenocryst compositions, all are low-Na; (2) phenocryst and vein-mineral compositions.

Next Page — 5-19: K-feldspar in patch with chlorite + calcite. 12-4: Part of crystal in center of white-mica-rich band; other half of crystal is plagioclase. 29-28: (1) K-feldspar phenocryst composition; (2) fine-grained adularia in veins. 60-3: (1) general K-feldspar phenocryst composition; (2) rims and altered patches to some K-feldspar phenocrysts; (3) fine-grained vein adularia. 91-13: adularia cement in brecciated zone. 122-5: Vein adularia.

Table 2, continued. K-Feldspar Analyses

	Well B								
	5-19	12-4	29-28		60-3			91-13	122-5
			(1)	(2)	(1)	(2)	(3)		
SiO_2	65.32	66.33	65.46	65.19	65.33	64.57	64.97	65.08	65.37
TiO_2	0.01	--	--	0.01	0.03	0.02	0.01	0.01	--
Al_2O_3	17.93	17.94	18.64	18.16	18.49	18.41	18.15	18.24	18.03
Fe_2O_3	0.18	--	0.09	0.03	0.13	0.03	0.04	0.02	0.03
MgO	--		0.02	0.01	0.01	--	--	--	--
MnO	0.01	--	--	--	0.01	0.01	--	--	--
CaO	--	--	0.15	--	0.25	0.01	--	--	--
Na_2O	0.53	0.55	2.08	0.56	3.41	0.71	0.57	0.56	0.56
K_2O	15.38	16.37	13.39	15.82	11.49	15.75	16.16	16.19	15.94
BaO	0.52		--	0.04	0.32	0.64	0.03	0.01	0.05
Total	99.88	101.19	99.83	99.82	99.47	100.15	99.93	100.11	99.98
Si	3.02	3.02	3.00	3.01	3.00	2.99	3.01	3.01	3.01
Al^{IV}	--	--	--	--	--	0.01	--	--	--
Al^{VI}	0.97	0.97	1.00	0.99	1.00	1.00	0.99	0.99	0.99
Ti	--	--	--	--	--	--	--	--	--
Fe^{+3}	0.01	--	--	--	--	--	--	--	--
Mg	--		--	--	--	--	--	--	--
Mn	--	--	--	--	--	--	--	--	--
Ca	--	--	0.01	--	0.01	--	--	--	--
Na	0.05	0.05	0.19	0.05	0.30	0.07	0.05	0.05	0.05
K	0.92	0.95	0.78	0.94	0.67	0.92	0.95	0.95	0.94
Ba	0.01		--	--	0.01	0.01	--	--	--
# Analyses	2	1	1	11	3	5	14	5	18
An	--	--	1.0	--	1.0	--	--	--	--
Ab	5.2	5.0	19.4	5.1	30.6	7.1	5.0	5.0	5.1
Or	94.8	95.0	79.6	94.9	68.4	92.9	95.0	95.0	94.9

Structural formula calculations assume O = 8.

Table 3. Plagioclase Analyses

	Well A											
	123-4B							146-4				
	(1)	(2)	(3)	(4)	(5)	(6)	(7)	(1)	(2)	(3)	(4)	(5)
SiO_2	62.87	64.38	66.44	67.03	67.86	68.66	64.02	57.40	59.77	61.73	65.60	66.94
TiO_2	0.02	--	--	--	0.01	--	0.13	0.02	0.02	0.01	0.01	--
Al_2O_3	23.03	22.23	21.12	20.65	20.11	19.64	21.82	26.93	25.04	23.79	21.45	20.58
Fe_2O_3	0.19	0.12	0.03	0.03	0.02	0.03	0.04	0.38	0.28	0.27	0.04	0.03
MgO	--	--	--	--	--	--	0.01	--	--	--	--	--
MnO	--	--	--	--	--	--	--	0.01	0.02	--	0.01	--
CaO	4.56	3.28	1.77	1.25	0.61	0.15	3.30	8.99	6.84	5.44	2.19	1.32
Na_2O	8.33	9.23	10.68	10.92	11.23	11.58	9.49	5.92	7.10	7.77	10.33	10.85
K_2O	0.77	0.55	0.08	0.10	0.09	0.08	0.22	0.45	0.71	0.97	0.23	0.11
BaO	0.03	0.02	0.01	0.02	0.01	0.02	0.02	0.05	0.05	0.03	0.01	0.01
Total	99.80	99.81	100.13	100.00	99.94	100.16	99.09	100.15	99.83	100.01	99.87	99.84
Si	2.79	2.84	2.91	2.94	2.96	2.99	2.85	2.57	2.67	2.75	2.89	2.93
Al^{IV}	0.21	0.16	0.09	0.06	0.04	0.01	0.15	0.43	0.33	0.25	0.11	0.07
Al^{VI}	1.00	1.00	1.00	1.00	1.00	1.00	1.00	0.99	0.99	0.99	1.00	1.00
Ti	--	--	--	--	--	--	--	--	--	--	--	--
Fe^{+3}	0.01	0.01	--	--	--	--	--	0.01	0.01	0.01	--	--
Mg	--	--	--	--	--	--	--	--	--	--	--	--
Mn	--	--	--	--	--	--	--	--	--	--	--	--
Ca	0.21	0.16	0.08	0.06	0.04	0.01	0.16	0.44	0.33	0.26	0.11	0.07
Na	0.72	0.79	0.91	0.93	0.95	0.98	0.82	0.54	0.62	0.67	0.88	0.92
K	0.04	0.03	0.01	0.01	0.01	0.01	0.01	0.03	0.04	0.06	0.01	0.01
Ba	--	--	--	--	--	--	--	--	--	--	--	--
# Analyses	2	1	22	14	10	4	1	1	9	25	6	9
An	21.7	16.3	8.0	6.0	4.0	1.0	16.2	43.9	33.3	26.2	11.0	7.0
Ab	74.2	80.6	91.0	93.0	95.0	98.0	82.8	53.1	62.6	67.7	88.0	92.0
Or	4.1	3.1	1.0	1.0	1.0	1.0	1.0	3.0	4.1	6.1	1.0	1.0

Structural formula calculations assume O = 8.

Table 3, continued. Plagioclase Analyses

	Well A						Well C			Well B
	173-6B						49-5			12-4
	(1)	(2)	(3)	(4)	(5)	(6)	(1)	(2)	(3)	
SiO_2	55.47	57.66	59.74	61.83	66.52	67.30	67.15	68.12	68.38	62.98
TiO_2	--	0.02	0.01	0.01	--	--	0.01	--	0.01	--
Al_2O_3	27.84	26.50	25.05	23.60	20.81	20.51	20.41	19.84	19.56	23.22
Fe_2O_3	0.26	0.23	0.25	0.25	0.05	0.02	0.01	0.01	0.01	0.02
MgO	--	--	0.01	--	--	--	--	--	--	
MnO	0.03	0.02	--	--	--	0.01	0.01	--	0.01	--
CaO	10.34	8.74	7.00	5.51	1.77	1.22	1.07	0.46	0.20	4.69
Na_2O	5.46	6.36	7.19	7.86	10.54	11.13	11.11	11.40	11.49	8.59
K_2O	0.34	0.49	0.67	0.93	0.19	0.16	0.14	0.14	0.21	0.20
BaO	0.03	0.02	0.01	0.05	0.03	0.01	0.02	0.02	0.02	
Total	99.77	100.04	99.93	100.04	99.91	100.36	99.93	99.99	99.89	99.70
Si	2.51	2.59	2.67	2.75	2.92	2.94	2.95	2.98	2.99	2.79
Al^{IV}	0.49	0.41	0.33	0.25	0.08	0.06	0.05	0.02	0.01	0.21
Al^{VI}	0.99	0.99	0.99	0.99	1.00	1.00	1.00	1.00	1.00	1.01
Ti	--	--	--	--	--	--	--	--	--	--
Fe^{+3}	0.01	0.01	0.01	0.01	--	--	--	--	--	--
Mg	--	--	--	--	--	--	--	--	--	
Mn	--	--	--	--	--	--	--	--	--	--
Ca	0.50	0.42	0.33	0.26	0.08	0.05	0.05	0.02	0.01	0.22
Na	0.48	0.55	0.63	0.68	0.91	0.95	0.94	0.97	0.98	0.74
K	0.02	0.02	0.04	0.05	0.01	0.01	0.01	0.01	0.01	--
Ba	--	--	--	--	--	--	--	--	--	
# Analyses	2	2	6	27	3	3	4	29	14	1
An	50.0	42.4	33.0	26.3	8.0	4.9	5.0	2.0	1.0	22.9
Ab	48.0	55.6	63.0	68.7	91.0	94.1	94.0	97.0	98.0	77.1
Or	2.0	2.0	4.0	5.0	1.0	1.0	1.0	1.0	1.0	--

Structural formula calculations assume O = 8.

Table 3, continued. Plagioclase Analyses

	Well B												
	29-28				60-3			91-13		122-5			
	(1)	(2)	(3)	(4)	(1)	(2)	(3)	(1)	(2)	(1)	(2)	(3)	(4)
SiO_2	67.41	68.34	66.80	66.46	61.27	67.69	65.73	68.21	66.04	61.10	61.66	67.59	66.24
TiO_2	0.01	--	0.01	--	--	0.01	0.01	0.01	0.03	--	0.01	0.01	0.02
Al_2O_3	20.10	19.56	20.69	21.13	24.12	20.04	21.50	19.74	21.16	23.89	23.73	20.36	21.22
Fe_2O_3	0.02	0.01	0.03	0.01	0.25	0.02	0.02	0.02	0.06	0.25	0.24	0.05	0.01
MgO	--	--	--	--	--	--	--	--	0.04	--	--	--	--
MnO	0.01	--	0.01	--	--	0.01	0.01	--	--	--	--	--	0.01
CaO	0.76	0.28	1.48	1.97	5.74	0.58	2.18	0.42	1.99	6.04	5.58	1.10	2.12
Na_2O	11.07	11.58	10.74	10.44	7.60	11.26	10.30	11.37	10.29	7.44	7.69	10.47	10.41
K_2O	0.18	0.12	0.23	0.20	0.98	0.15	0.29	0.14	0.35	0.92	1.02	0.21	0.21
BaO	0.02	0.03	0.01	0.03	0.03	--	0.02	0.02	--	0.03	0.03	0.01	0.01
Total	99.58	99.92	100.00	100.24	99.99	99.76	100.06	99.93	99.96	99.67	99.96	99.80	100.25
Si	2.96	2.99	2.93	2.91	2.73	2.97	2.89	2.99	2.90	2.73	2.75	2.95	2.90
Al^{IV}	0.04	0.01	0.07	0.09	0.27	0.03	0.11	0.01	0.10	0.27	0.25	0.05	0.10
Al^{VI}	1.00	1.00	1.00	1.00	0.99	1.00	1.00	1.00	1.00	0.99	0.99	1.00	1.00
Ti	--	--	--	--	--	--	--	--	--	--	--	--	--
Fe^{+3}	--	--	--	--	0.01	--	--	--	--	0.01	0.01	--	--
Mg	--	--	--	--	--	--	--	--	--	--	--	--	--
Mn	--	--	--	--	--	--	--	--	--	--	--	--	--
Ca	0.04	0.01	0.07	0.09	0.27	0.03	0.10	0.02	0.10	0.29	0.26	0.05	0.10
Na	0.95	0.98	0.91	0.89	0.66	0.96	0.88	0.97	0.88	0.64	0.67	0.93	0.89
K	0.01	0.01	0.01	0.01	0.06	0.01	0.02	0.01	0.02	0.05	0.06	0.01	0.01
Ba	--	--	--	--	--	--	--	--	--	--	--	--	--
# Analyses	13	10	9	3	6	11	13	27	2	2	14	10	10
An	4.0	1.0	7.1	9.1	27.3	3.0	10.0	2.0	10.0	29.6	26.3	5.1	10.0
Ab	95.0	98.0	91.9	89.9	66.6	96.0	88.0	97.0	88.0	65.3	67.7	93.9	89.0
Or	1.0	1.0	1.0	1.0	6.1	1.0	2.0	1.0	2.0	5.1	6.0	1.0	1.0

Structural formula calculations assume O = 8.

Table 3, continued. Plagioclase Analyses

Legend

Well A — 123-4B: (1) and (2) are the most calcic plagioclase compositions, which are restricted to small patches in plagioclase phenocrysts; (3)–(6) are remnants of plagioclase phenocrysts surrounding voids, probably recrystallized, many with euhedral terminations along the voids; (7) a small, euhedral crystal intergrown with titanite along the edge of a void. 146-4: (1) calcium-rich core of a plagioclase phenocryst; (2) other relict andesine compositions; (3) the principal composition of plagioclase phenocrysts in the sample; (4) and (5) are altered patches in plagioclase, some adjacent to cavities in the crystals. 173-6B: (1) fragments in a sheared zone; (2) and (3) are other relatively calcic plagioclase compositions, obtained from phenocrysts and grains in shears; (4) the most common plagioclase composition in this core sample; (5) and (6) are altered patches in the phenocrysts, generally surrounding small voids.

Well C — 49-5: The three analyses, all albites, are all representative of the compositions of plagioclase phenocrysts, vein minerals, and albitic alteration of K-feldspar phenocrysts.

Well B — 12-4: In white-mica-rich patch, possibly overgrown by K-feldspar. 29-28: (1) and (2) are the present compositions of plagioclase phenocrysts; (3) clear rims to plagioclase crystals in and adjacent to fine-grained adularia + quartz bands; (4) small crystal growing into an open space in one of the adularia + quartz veins. 60-3: (1) relict plagioclase phenocryst compositions; (2) present composition of many plagioclase phenocrysts, particularly those caught up in or adjacent to the fine-grained adularia + quartz band; (3) rims and overgrowths on plagioclase phenocrysts in the fine-grained adularia + quartz band. 91-13: (1) present composition of plagioclase phenocrysts in tuff fragments of a brecciated zone; (2) overgrowth on plagioclase phenocryst into adularia band. 122-5: (1) most calcic plagioclase composition, restricted to small patches in phenocrysts; (2) principal composition of plagioclase phenocrysts; (3) rims and overgrowths on plagioclase phenocrysts adjacent to an adularia-bearing vein; (4) vein-filling minerals where the vein crosses plagioclase phenocrysts.

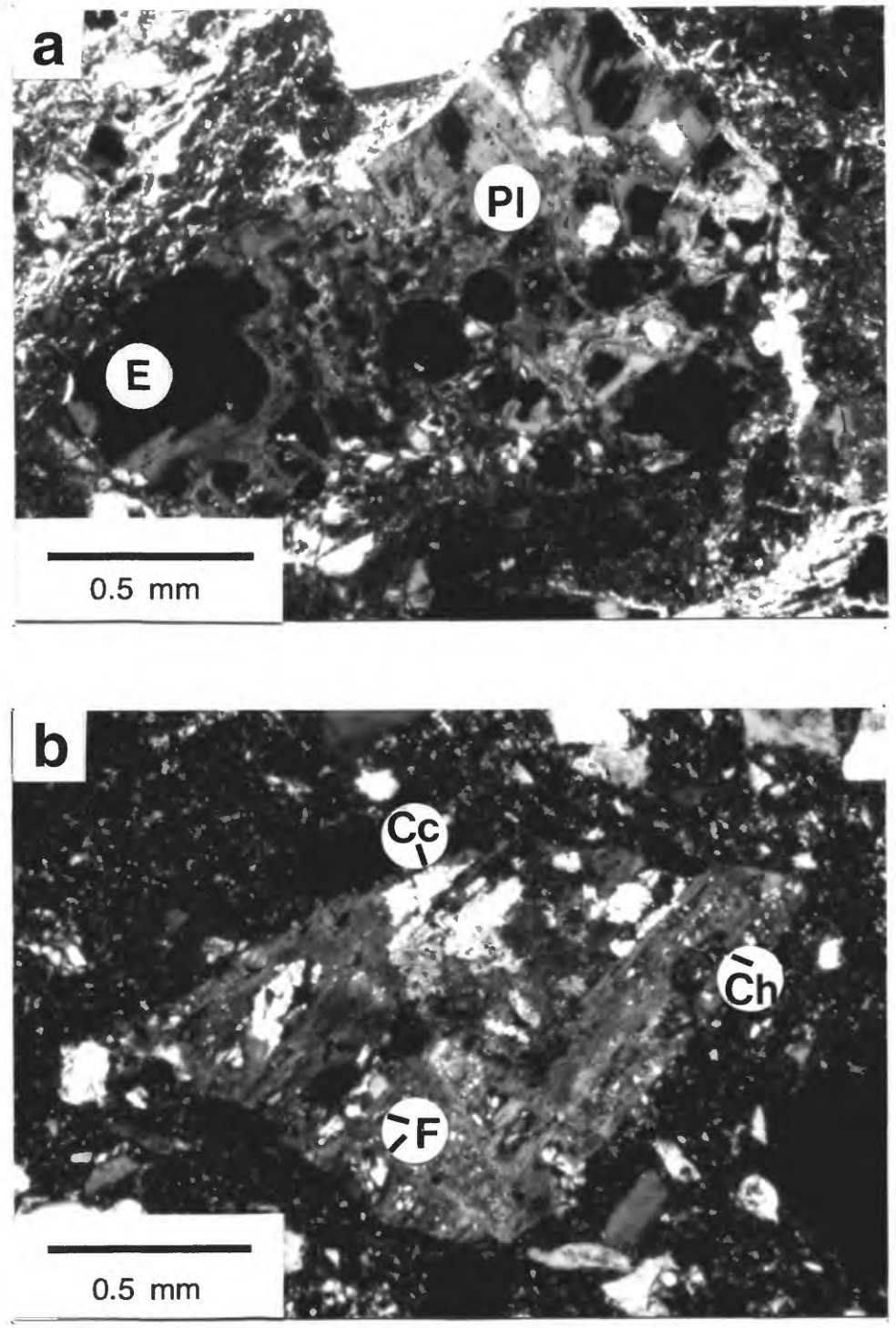

Figure 4. Plagioclase textures. a) Plagioclase (Pl) phenocryst containing numerous dissolution cavities, 123-4B, well A. The remaining feldspar is albite (An_1); crossed polarizers. E = epoxy. b) Plagioclase phenocryst from 71-3, well B, containing several oval patches, possibly former dissolution cavities, that are now filled with chlorite (Ch), calcite (Cc) + chlorite, and aggregates of fine-grained feldspar (F); crossed polarizers.

were initially more calcic but have been thoroughly albitized under hydrothermal conditions. The chemistry of the minor elements supports this idea, because the "igneous" plagioclases generally contain ≈0.2–0.3 wt% Fe_2O_3 and 0.5–1.0 wt% K_2O, whereas the "hydrothermal" plagioclases contain ≤0.05 wt% Fe_2O_3 and ≤0.25 wt% K_2O. The well B oligoclases may also represent partly altered andesines, but these crystals retain the igneous content of minor elements.

The compositions of partly dissolved plagioclase phenocrysts from well A have also been modified. Small patches within the crystal relics have oligoclase compositions (≈$An_{20}Ab_{80}$), but the euhedral crystals lining the voids are albites with "hydrothermal" Fe_2O_3 and K_2O contents.

Some of the younger hydrothermal plagioclase crystals in well B core samples have slightly higher Ca-contents than the older ones. Plagioclase phenocrysts caught up in the extensive vein systems in 29-28 have been albitized to a composition of An_{1-4}. These crystals have rims and overgrowths of composition An_7, and a small euhedral plagioclase growing into a void space as part of the latest hydrothermal mineralization event has the composition An_9. Similarly, plagioclase phenocrysts in the fine-grained adularia + quartz band in 60-3 are albites of composition $An_3Ab_{96}Or_1$, whereas later overgrowths on these crystals have the composition $An_{11}Ab_{88}Or_1$. A corresponding situation may occur in 122-5. There, a series of plagioclase phenocrysts cut by a medium-grained adularia vein have rims of albite (An_5) along the vein walls, whereas the center of the vein is filled with separate plagioclase crystals of composition An_{10}. One possible additional example comes from well A sample 123-4B. The remnants of a partly dissolved plagioclase crystal are principally albite, but a titanite crystal that grows into one of the voids is intergrown with a small, possibly separate crystal of oligoclase (An_{16}).

Chlorite. Chlorite is an important vein and replacement mineral of wells A and B, but almost no chlorite was found in the well C thin sections. During SEM study of the well C sample, one spot analysis yielded a chlorite spectrum with only minor K contamination, but the spot was

too small to identify with a petrographic microscope. Chlorites in wells A and B have four principal types of occurrence: (1) chlorite replaces mafic phenocrysts and grains in the tuff. The outlines of the original phenocrysts suggest that the chlorite has replaced both biotite and amphibole. The chlorite replacing biotite is generally intergrown with large amounts of titanite and some K-mica. (2) Sheared bands and veins of calcite + chlorite + titanite are found throughout well A and in core samples 5-19 and 12-4 of well B. (3) Chlorite is commonly intergrown with K-mica in veins and altered mafic minerals, and in at least some cases the chlorite appears to be replacing the white mica. (4) Chlorite forms aggregates of vermicular crystals in the adularia veins of well B. In this occurrence, the chlorite partly fills void spaces in the veins.

Because of the close association between chlorite and K-mica, several of the microprobe analyses obtained in this study are mixtures of the two minerals. Only chlorite analyses with ≤0.3 wt% K_2O are reported in Table 4. Most of the chlorites in wells A and B have similar compositions, whatever their occurrence. They generally have Si contents in the range 5.4–5.9 (out of a possible total of 8 Si), iron-to-magnesium ratios [Fe/(Fe + Mg)] between 0.40 and 0.65, and less than 2 wt% MnO (Table 4). The chlorites from well A sample 146-4 are the major exception, being the most siliceous and magnesian, with Si = 5.97–6.09 and Fe/(Fe+ Mg) ≈ 0.2. This core sample contains many fractures and brecciated zones lined with the ferric-iron mineral hematite, whereas most of the iron in chlorite is ferrous. The very low Fe-contents may therefore result from the abundance of ferric iron in that sample. High silica contents, in turn, are closely correlated with high Mg contents of chlorite (Bevins et al., 1991). The chlorites from 146-4 also contain relatively large amounts of Mn, in the range 2.4–2.8 wt% MnO.

K-Mica. K-mica (white mica) is a very important constituent of wells A and C, but it is only sporadically abundant in well B. In well C, K-mica is present instead of chlorite: white mica and TiO_2 replace biotite phenocrysts, and K-mica grows into a major open vein from the sides. In addition, K-feldspar phenocrysts in well C typically are partly altered to white mica

Table 4. Chlorite Analyses

	Well A						
	123-4B		146-4		173-6B		
	(1)	(2)	(1)	(2)	(1)	(2)	(3)
SiO_2	26.01	25.23	30.37	30.94	25.53	26.24	26.73
TiO_2	0.07	0.03	0.04	0.02	--	0.14	0.08
Al_2O_3	19.92	20.25	19.59	19.42	21.29	20.92	20.82
FeO	27.00	26.62	10.70	9.44	27.02	25.48	24.48
MgO	11.93	12.29	22.37	24.65	12.04	13.42	12.41
MnO	1.00	1.05	2.82	2.51	1.47	1.08	1.29
CaO	0.09	0.08	0.18	0.30	0.04	0.09	0.10
Na_2O	0.06	0.07	0.11	0.11	0.04	0.03	0.04
K_2O	0.06	0.10	0.16	0.10	0.07	0.08	0.09
Total	86.14	85.72	86.34	87.49	87.50	87.48	86.04
Si	5.66	5.52	6.06	6.04	5.47	5.57	5.73
Al^{IV}	2.34	2.48	1.94	1.96	2.53	2.43	2.27
Al^{VI}	2.77	2.74	2.66	2.51	2.85	2.79	2.99
Ti	0.01	0.01	--	--	--	0.02	0.01
Fe^{+2}	4.91	4.87	1.79	1.54	4.85	4.52	4.39
Mg	3.87	4.00	6.64	7.17	3.85	4.24	3.97
Mn	0.18	0.20	0.48	0.42	0.27	0.19	0.24
Ca	0.02	0.02	0.04	0.06	0.01	0.02	0.02
Na	0.02	0.02	0.03	0.03	0.01	0.01	0.01
K	0.01	0.02	0.04	0.02	0.01	0.02	0.03
# Analyses	1	6	4	16	7	5	1
T (°C)	315	337	250	254	347	328	302
Fe/(Fe + Mg)	0.56	0.55	0.21	0.18	0.56	0.52	0.53

Structural formula calculations assume anhydrous O = 28.
Temperatures were calculated using the chlorite geothermometer of Cathelineau (1988).
123-4B: (1) chlorite filling spaces in brecciated quartz; (2) groundmass chlorite. 146-4: (1) chlorite in shears; (2) vein chlorite, intergrown with calcite + titanite. 173-6B: (1) chlorite associated with shears; (2) and (3) chlorite-rich clasts adjacent to shears.

Table 4, continued. Chlorite Analyses

	Well B						
	5-19			12-4			
	(1)	(2)	(3)	(1)	(2)	(3)	(4)
SiO_2	25.04	26.68	26.99	24.46	25.16	25.92	25.62
TiO_2	0.01	0.02	0.05	0.06	0.01	0.07	0.01
Al_2O_3	21.87	20.12	20.23	21.54	20.40	21.54	19.79
FeO	30.80	28.24	27.99	30.49	25.92	28.15	24.76
MgO	9.13	11.56	11.31	9.12	12.91	10.34	13.70
MnO	0.50	0.64	0.64	1.43	1.75	1.23	1.71
CaO	0.30	0.19	0.17	0.05	0.03	0.06	0.09
Na_2O	0.09	0.07	0.08	0.02	0.03	0.05	0.04
K_2O	0.20	0.16	0.28	0.07	0.08	0.23	0.12
Total	87.94	87.78	87.74	87.24	86.29	87.59	85.84
Si	5.43	5.72	5.77	5.37	5.46	5.57	5.56
Al^{IV}	2.57	2.28	2.23	2.63	2.54	2.43	2.44
Al^{VI}	3.02	2.79	2.86	2.94	2.69	3.03	2.62
Ti	--	--	0.01	0.01	--	0.01	--
Fe^{+2}	5.60	5.06	4.99	5.60	4.71	5.06	4.49
Mg	2.95	3.69	3.60	2.99	4.18	3.31	4.43
Mn	0.09	0.12	0.12	0.27	0.32	0.22	0.32
Ca	0.07	0.05	0.04	0.01	0.01	0.02	0.02
Na	0.04	0.03	0.03	0.01	0.01	0.02	0.02
K	0.05	0.04	0.08	0.02	0.02	0.06	0.04
# Analyses	1	5	6	2	8	3	6
T (°C)	350	305	299	360	347	328	331
Fe/(Fe + Mg)	0.66	0.58	0.58	0.65	0.53	0.60	0.50

Structural formula calculations assume anhydrous O = 28.

Temperatures were calculated using the chlorite geothermometer of Cathelineau (1988).

5-19: (1) is chlorite from rim of chlorite + calcite + titanite patch; (2) chlorite in titanite bands in groundmass; (3) chorite replacing biotite phenocrysts. 12-4: (1)–(3) are small crystals adjacent to void spaces in recrystallized groundmass; (4) chlorite intergrown with epidote + allanite + titanite + adularia + quartz.

Table 4, continued. Chlorite Analyses

	Well B								
	29-28								
	(1)	(2)	(3)	(4)	(5)	(6)	(7)	(8)	(9)
SiO_2	25.66	26.75	27.53	24.92	26.32	27.51	24.52	25.59	27.28
TiO_2	0.01	0.13	0.02	0.02	0.17	0.48	0.01	0.08	0.10
Al_2O_3	20.85	19.20	19.45	20.06	20.35	19.62	21.20	20.80	19.77
FeO	27.88	23.17	20.21	30.53	26.68	23.70	33.09	28.79	24.50
MgO	12.18	15.82	17.44	9.42	12.71	14.69	7.89	10.92	14.80
MnO	1.42	1.57	1.75	1.13	1.22	1.52	1.11	1.14	1.48
CaO	0.02	0.07	0.04	0.22	0.07	0.11	0.07	0.03	0.03
Na_2O	0.01	0.05	0.01	0.06	0.04	0.06	0.05	0.03	0.04
K_2O	0.06	0.09	0.14	0.06	0.20	0.19	0.07	0.10	0.11
Total	88.09	86.85	86.59	86.42	87.76	87.88	88.01	87.48	88.02
Si	5.48	5.67	5.75	5.53	5.61	5.76	5.40	5.53	5.72
Al^{IV}	2.52	2.33	2.25	2.47	2.39	2.24	2.60	2.47	2.28
Al^{VI}	2.74	2.47	2.54	2.78	2.72	2.60	2.91	2.83	2.61
Ti	0.01	0.02	--	--	0.03	0.08	--	0.01	0.01
Fe^{+2}	4.99	4.11	3.53	5.67	4.76	4.16	6.10	5.22	4.29
Mg	3.88	5.00	5.44	3.12	4.04	4.58	2.59	3.52	4.63
Mn	0.25	0.28	0.31	0.21	0.22	0.27	0.21	0.21	0.26
Ca	--	0.01	0.01	0.05	0.01	0.02	0.02	--	--
Na	--	0.01	0.01	0.02	0.01	0.02	0.01	0.01	0.02
K	0.02	0.03	0.04	0.01	0.04	0.04	0.02	0.03	0.03
# Analyses	2	6	7	2	6	3	5	10	4
T (°)	344	312	299	334	321	299	357	334	305
Fe/(Fe + Mg)	0.56	0.45	0.39	0.65	0.54	0.48	0.70	0.60	0.48

Structural formula calculations assume anhydrous O = 28.

Temperatures were calculated using the chlorite geothermometer of Cathelineau (1988).

29-28: (1)–(3) are fine-grained chlorites in adularia + quartz patches; (4) chlorite adjacent to vein calcite; (5) and (6) are chlorites associated with titanite bands; (7) chlorite as a replacement mineral in small clasts and a plagioclase crystal; (8) and (9) are chlorites replacing biotite phenocrysts.

Table 4, continued. Chlorite Analyses

	Well B								
	60-3						122-5		
	(1)	(2)	(3)	(4)	(5)	(6)	(1)	(2)	(3)
SiO_2	24.74	26.18	27.19	27.72	27.02	26.93	26.31	25.47	28.56
TiO_2	0.04	0.08	0.02	0.02	0.04	0.03	0.16	0.04	0.01
Al_2O_3	20.81	20.49	19.03	18.97	19.55	18.90	20.28	18.65	18.86
FeO	31.65	26.25	22.52	21.80	23.10	29.00	27.83	34.67	19.66
MgO	9.25	12.77	16.50	16.05	14.75	10.34	12.45	8.30	18.44
MnO	0.69	0.94	1.47	1.38	0.70	0.71	0.86	0.95	1.39
CaO	0.02	0.07	0.04	0.08	0.07	0.08	0.04	0.13	0.05
Na_2O	0.09	0.05	0.03	0.11	0.14	0.19	0.02	0.01	0.06
K_2O	0.12	0.14	0.10	0.21	0.10	0.11	0.09	0.03	0.11
Total	87.41	86.97	86.90	86.34	85.47	86.29	88.04	88.25	87.14
Si	5.44	5.61	5.73	5.85	5.78	5.89	5.60	5.64	5.89
Al^{IV}	2.56	2.39	2.27	2.15	2.22	2.11	2.40	2.36	2.11
Al^{VI}	2.83	2.78	2.46	2.58	2.71	2.77	2.71	2.51	2.48
Ti	0.01	0.02	--	--	0.01	0.01	0.02	0.01	--
Fe^{+2}	5.82	4.70	3.98	3.85	4.14	5.31	4.96	6.44	3.39
Mg	3.03	4.08	5.17	5.04	4.70	3.37	3.95	2.74	5.67
Mn	0.13	0.17	0.27	0.25	0.13	0.13	0.16	0.18	0.24
Ca	--	0.01	0.01	0.02	0.01	0.02	0.01	0.03	0.01
Na	0.04	0.02	0.01	0.04	0.06	0.08	0.01	--	0.02
K	0.13	0.03	0.02	0.05	0.03	0.03	0.02	0.01	0.03
# Analyses	1	5	5	5	2	1	21	6	14
T (°C)	350	321	302	283	295	279	324	318	279
Fe/(Fe + Mg)	0.66	0.54	0.44	0.43	0.47	0.61	0.56	0.70	0.37

Structural formula calculations assume anhydrous O = 28.

Temperature calculations were made using the chlorite geothermometer of Cathelineau (1988).

60-3: (1) and (2) are chlorites replacing biotite phenocrysts; (3) and (4) are small crystals in fine-grained adularia + quartz band; (5) and (6) are small crystals in groundmass. 122-5: (1) chlorite after mafic phenocrysts (amphiboles?); (2) chlorite with calcite in clast; (3) small, vermicular crystals in adularia vein.

+ albite along cracks. White mica is a common vein-filling mineral in well A core, where it generally is associated with calcite or quartz; it also is closely mixed with chlorite in veins and altered mafic minerals. White mica is variably distributed among the well B core samples; it is a relatively abundant hydrothermal mineral in the two shallowest samples, 5-19 and 12-4, but at deeper levels it is concentrated in particular clasts and is not closely associated with hydrothermal vein assemblages.

The basic muscovite mineral formula, $K_2Al_4(Si_6Al_2)O_{20}(OH)_4$, can be modified through a series of exchange reactions to produce illite, phengite, or hydromuscovite compositions (Deer et al., 1962): illite, $KAl^{IV} = \square Si$, where $\square$ denotes a lattice vacancy; phengite, $Al^{IV}Al^{VI} = Si(Fe^{+2}, Mg)$; hydromuscovite, $K = (H_3O)^+$ or $KO^{-2} = \square(OH)^-$. For the most part these minerals appear to be well crystallized and to have only moderate phengite- and illite-type substitutions (Table 5). The K_2O contents generally exceed 9 wt% and the oxide sums tend to fall between 95 and 96 wt%, indicating a low hydromuscovite component. The mineral formula for each analysis in Table 5 was calculated twice, once with all iron considered to be ferric, and the second time with all iron as ferrous. The ferric-iron formulae had the best distribution of octahedral ions in all cases, and they are presented in Table 5.

In well C, white mica has essentially the same composition whatever its mode of occurrence, although the white micas replacing feldspars have slightly reduced Mg-contents compared to the others. These analyses are characterized by a predominance of illite-type substitutions. White micas from well A generally have higher Mg and lower Al^{VI} contents than those from well C, indicating larger amounts of phengite-type substitution. All of the well A and C analyses probably represent hydrothermal compositions; in contrast, several of the well B micas may be relict crystals. Possibly relict igneous micas are those with low Si and high Al contents, approaching the ideal muscovite composition, along with comparatively high Na_2O and TiO_2 contents. The first two analyses reported for 122-5 are for crystals from metasedimentary clasts. Based on their textures, these crystals probably were part of the

Table 5. K-Mica Analyses

	Well A					Well C		
	123-4B		146-4		173-6B	49-5		
	(1)	(2)	(1)	(2)		(1)	(2)	(3)
SiO_2	51.55	50.21	50.60	51.19	51.64	51.60	52.05	51.38
TiO_2	0.17	0.24	0.09	0.05	0.10	0.14	0.27	0.16
Al_2O_3	28.73	28.74	28.21	29.76	28.11	30.65	30.62	30.02
Fe_2O_3	4.21	6.25	2.61	2.87	3.75	2.71	2.50	2.73
MgO	1.66	2.20	2.15	2.12	2.81	1.39	1.78	1.73
MnO	0.05	0.12	0.10	0.16	0.05	0.01	0.02	0.02
CaO	0.15	0.11	0.12	0.15	0.18	0.08	0.05	0.12
Na_2O	0.15	0.12	0.15	0.18	0.17	0.15	0.05	0.14
K_2O	8.63	8.09	9.33	8.15	9.13	9.45	8.98	9.37
Total	95.30	95.96	93.36	94.63	95.94	96.18	96.32	95.67
Si	6.78	6.60	6.80	6.74	6.77	6.72	6.74	6.73
Al^{IV}	1.22	1.40	1.20	1.26	1.23	1.28	1.26	1.27
Al^{VI}	3.23	3.05	3.27	3.36	3.12	3.42	3.41	3.36
Ti	0.02	0.02	0.01	--	0.01	0.01	0.03	0.02
Fe^{+3}	0.42	0.62	0.26	0.28	0.37	0.27	0.24	0.27
Mg	0.33	0.43	0.43	0.42	0.55	0.27	0.34	0.34
Mn	--	0.01	0.01	0.02	0.01	--	--	--
Ca	0.02	0.02	0.02	0.02	0.02	0.01	0.01	0.01
Na	0.04	0.03	0.04	0.05	0.04	0.04	0.01	0.03
K	1.45	1.36	1.61	1.37	1.53	1.57	1.48	1.57
# Analyses	11	6	6	3	11	22	9	22

Structural formula calculations assume anhydrous O = 22.

123-4B: Small groundmass crystals and replacement of biotite phenocrysts. 146-4: (1) is representative of recrystallized patches in groundmass and sericitic alteration of plagioclase; (2) K-micas associated with chlorite in shears. 173-6B: White mica in and adjacent to shears. 49-5: (1) alteration of feldspars, especially K-feldspar; (2) replacement of biotite phenocrysts; (3) small crystals in groundmass.

Table 5, continued. White Mica Analyses

	Well B									
	5-19	12-4		60-3			122-5			
		(1)	(2)	(1)	(2)	(3)	(1)	(2)	(3)	(4)
SiO_2	49.71	49.24	50.55	51.55	46.53	50.31	52.26	51.57	48.31	48.90
TiO_2	0.15	0.21	0.31	0.38	0.42	0.07	0.18	0.36	0.10	0.06
Al_2O_3	31.76	36.02	33.80	27.79	33.02	32.30	28.01	27.59	28.94	34.34
Fe_2O_3	3.90	0.56	0.19	2.64	1.70	1.71	4.60	4.34	4.14	1.42
MgO	1.10	0.95	2.42	2.94	0.75	1.34	2.56	3.08	2.08	0.55
MnO	0.02	--	--	0.01	0.05	0.03	0.09	--	0.06	0.03
CaO	0.12	--	--	0.06	0.05	0.04	0.07	--	0.04	0.01
Na_2O	0.15	0.25	0.27	0.12	0.32	0.12	0.10	0.11	0.13	0.10
K_2O	9.34	9.74	9.35	8.99	10.43	9.81	8.87	9.98	9.83	9.99
Total	96.25	96.97	96.89	94.48	93.27	95.73	96.74	97.03	93.64	95.40
Si	6.51	6.34	6.49	6.83	6.31	6.58	6.79	6.74	6.55	6.42
Al^{IV}	1.49	1.66	1.51	1.17	1.69	1.42	1.21	1.26	1.45	1.58
Al^{VI}	3.41	3.80	3.60	3.17	3.59	3.56	3.08	2.99	3.18	3.74
Ti	0.01	0.02	0.03	0.04	0.04	0.01	0.02	0.03	0.01	0.01
Fe^{+3}	0.38	0.05	0.02	0.27	0.17	0.17	0.45	0.43	0.42	0.14
Mg	0.22	0.18	0.46	0.58	0.15	0.26	0.50	0.60	0.42	0.10
Mn	--	--	--	--	0.01	--	0.01	--	0.01	--
Ca	0.02	--	--	0.01	0.01	--	0.01	--	0.01	--
Na	0.04	0.06	0.07	0.03	0.09	0.03	0.03	0.03	0.03	0.03
K	1.56	1.60	1.53	1.52	1.81	1.64	1.47	1.66	1.70	1.67
# Analyses	11	7	4	1	1	5	6	2	1	4

Structural formula calculations assume anhydrous O = 22.

5-19: K-mica surrounding chlorite and calcite. 12-4: (1) narrow, euhedral K-micas adjacent to pyrite crystals; (2) white mica associated with myrmekite patch. 60-3: (1) and (2) are from small, K-mica-rich clasts in groundmass; (3) sericitic alteration of large plagioclase phenocryst. 122-5: (1) coarse-grained, K-mica + titanite-rich clast; (2) white micas in quartz-rich metasedimentary clast; (3) K-mica associated with titanite- or pyrite-rich bands in groundmass; (4) sericitic alteration of plagioclase.

metasedimentary assemblage, although their compositions are indistinguishable from those of the hydrothermal minerals.

Titanite. Titanite is moderately abundant in every piece of core. Narrow, irregular bands or veinlets consisting solely of titanite are found in most thin sections. Titanite is an important constituent of veins and sheared bands containing chlorite + calcite, and it is intergrown with quartz in the prominent well C veins. In well B, bands of titanite are concentrated along the sides of the numerous adularia veins (Fig. 5a), where it forms clear, brownish, lumpy crystals that appear to grow out into the vein from the adjoining country rock. This suggests that at least one of the elements needed for titanite is derived from the tuff; titanium is a likely possibility, because it tends to be an immobile element during metamorphism. Similarly, some of the narrow titanite-rich veinlets are surrounded by bands of relatively clean-looking rock, that is, tuff containing lesser amounts of minute, disseminated dark grains. Titanite also occurs as a replacement mineral in feldspars; crystals of titanite commonly grow into the void spaces in the partly dissolved feldspars of well A.

The titanite in these core samples is distinctive in having unusually high Al contents, to 10.4 wt% Al_2O_3 (Table 6). However, titanites nearly as aluminous as this have been reported from the geothermal fields at Cerro Prieto, Mexico (Schiffman et al., 1985; they found a maximum of 10.2 wt% Al_2O_3) and the Salton Sea, California (Cho et al., 1988). The maximum Al content is higher for well A (10.4 wt% Al_2O_3) than for well B (8.3 wt% Al_2O_3). No titanite crystals from well C have as yet been analyzed, but spectra for well C titanites made during SEM analysis contain Al peaks of comparable size to those from the other wells. Some of the titanite crystals are compositionally zoned with respect to Ti and Al; in Figure 5b the brighter wedges of titanite have higher Ti-contents and lower Al-contents than the darker areas. In some of the crystals the darker, Al-rich titanite seems to surround the brighter wedges of Ti-rich titanite, but in the largest crystal the brighter and darker areas occur side by side.

Aluminum substitutes for Ti in titanite according to the coupled exchange: $Ti^{+4}O^{-2} = (Al,Fe^{+3})(F,OH^{-})$ (Higgins and Ribbe, 1976). Although Higgins and Ribbe (1976) inferred

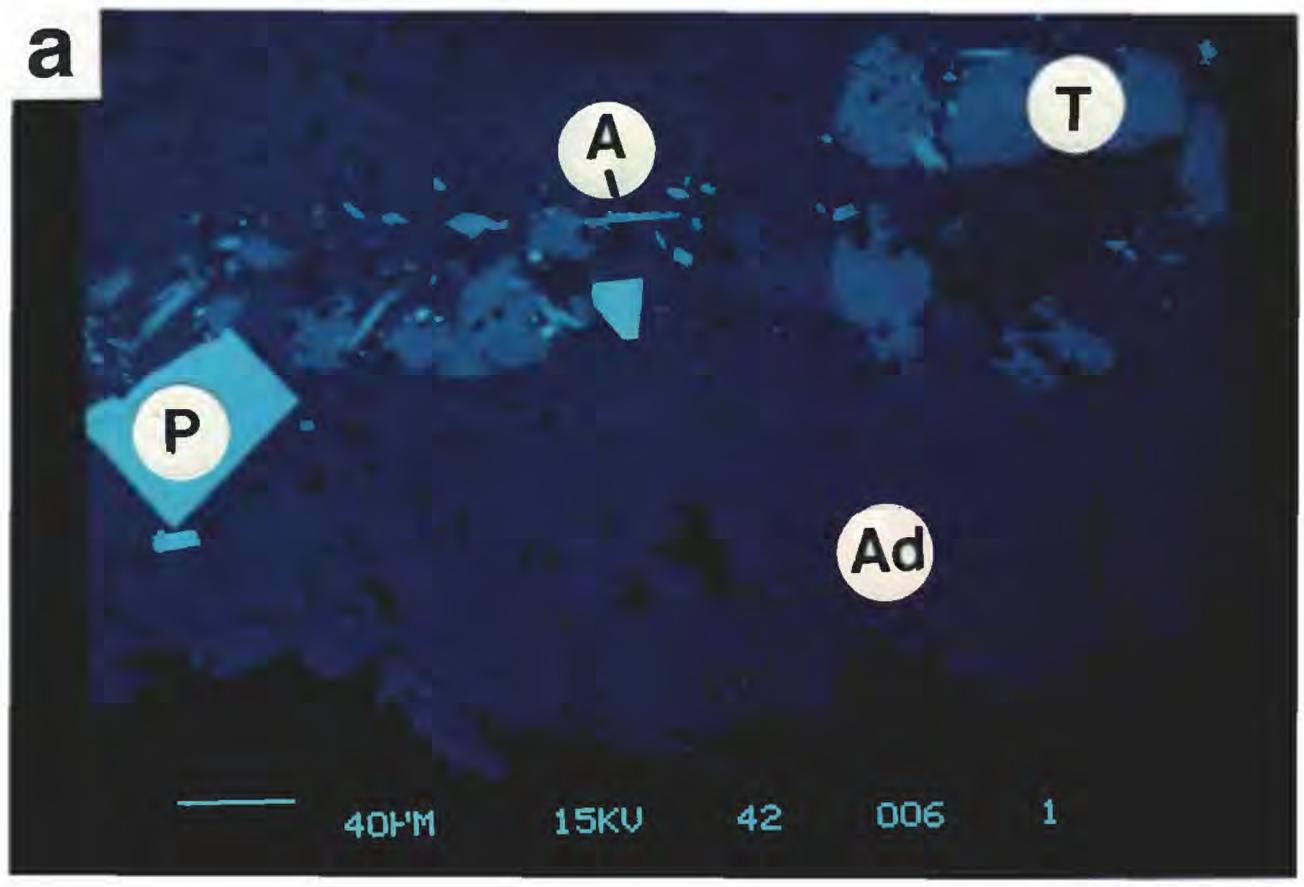

Figure 5. Back-scattered electron SEM images of titanite and epidote-group minerals. a) Open vein lined with fine-grained adularia (Ad). Concentrated along the vein-tuff boundary is a band rich in medium-grained titanite (T), surrounded and partly intergrown with narrow, bright blades of allanite (A) and euhedral pyrite (P) crystals.

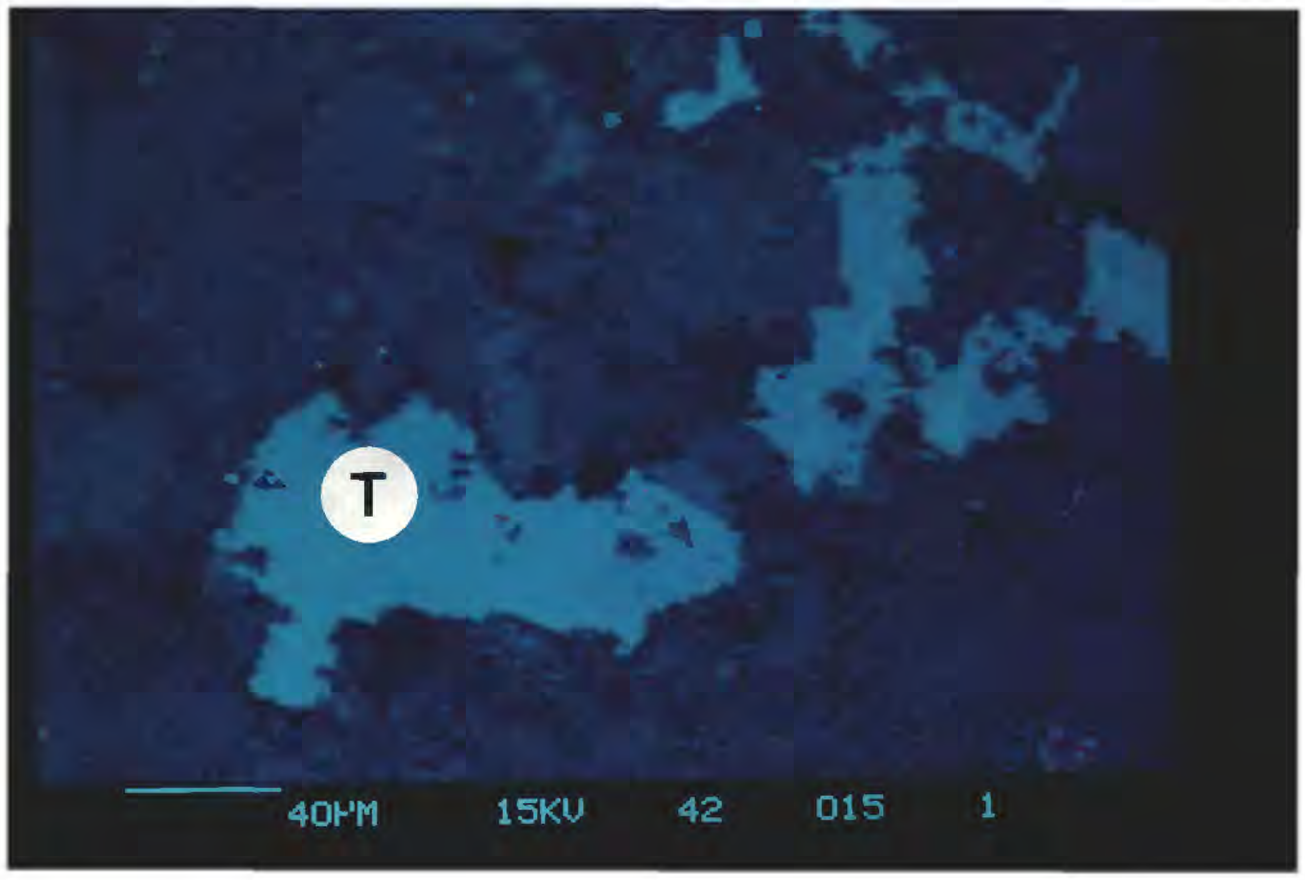

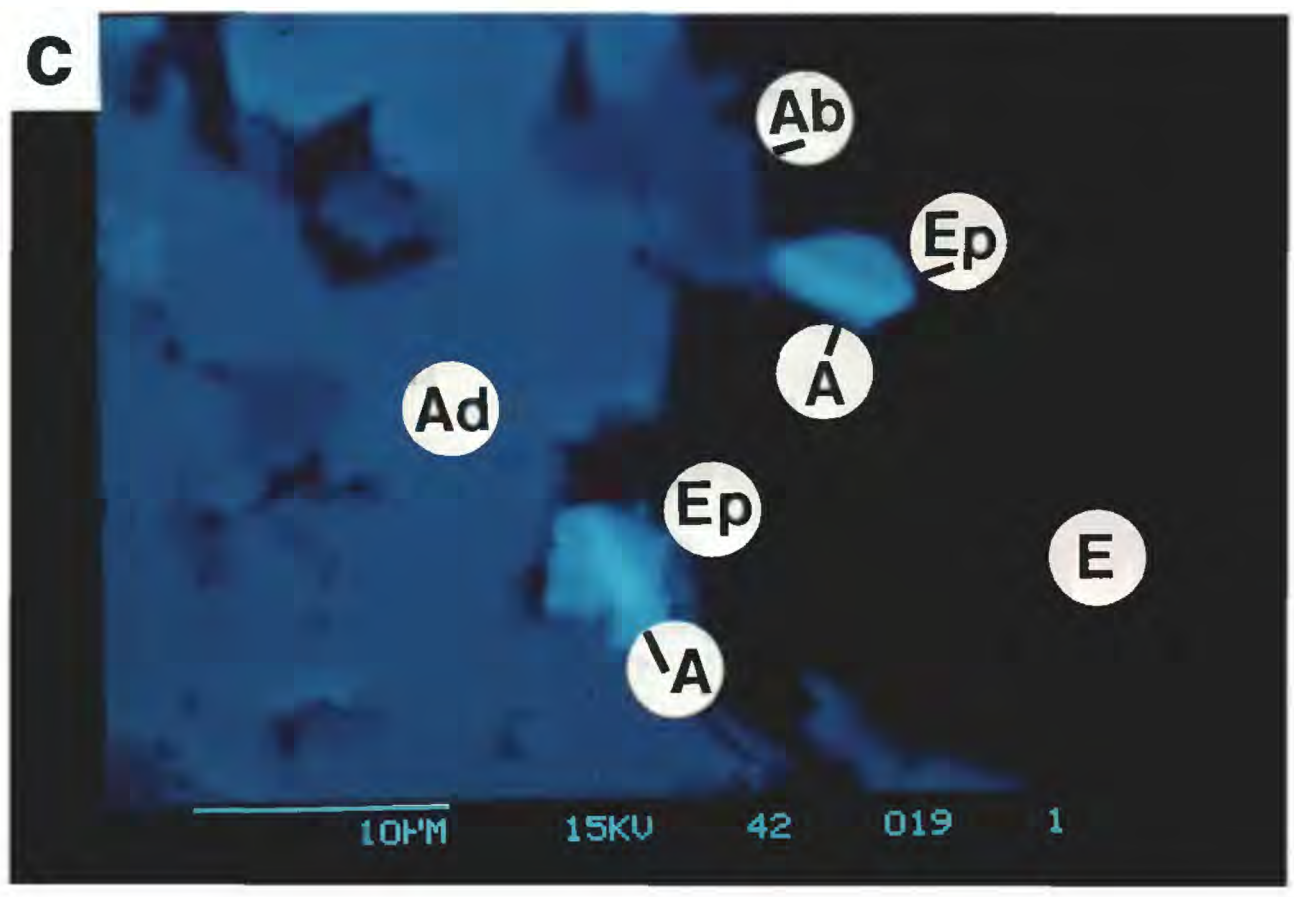

Figure 5, continued. b) Compositionally zoned titanite crystals; brighter wedges have higher Ti and correspondingly lower Al contents than darker zones. c) Small, composite crystals with brighter allanite cores and darker epidote (Ep) rims, that extend from a hydrothermal deposit of adularia + albite (Ab). E = epoxy.

Table 6. Titanite Analyses

	Well A										
	123-4B				146-4				173-6B		
	(1)	(2)	(3)	(4)	(1)	(2)	(3)	(4)	(1)	(2)	(3)
SiO_2	30.30	30.03	30.38	30.97	30.65	30.84	31.85	31.69	31.09	31.46	31.44
TiO_2	35.65	31.81	29.81	27.82	31.82	28.88	25.79	23.35	28.64	26.90	26.65
Al_2O_3	3.16	5.00	6.57	7.96	5.14	6.77	8.53	10.38	6.92	8.28	9.16
Fe_2O_3	0.32	0.42	0.63	0.60	0.04	0.89	0.92	0.90	1.00	0.98	1.23
MgO	--	--	--	--		0.04					
MnO	0.02	0.01	0.01	0.02	0.05	0.09	0.10	0.04	0.07	0.03	0.06
CaO	28.80	27.88	28.42	27.74	28.79	28.60	28.58	29.31	28.43	28.31	29.37
Na_2O	--	0.05	0.01	0.04	--	0.01	0.03	0.02	0.03	0.04	--
K_2O	0.02	0.04	0.05	0.04	0.03	0.11	0.09	0.11	0.08	0.10	0.05
BaO		0.12		0.07	0.21	0.20	0.18	0.13			
Total	98.27	95.36	95.88	95.26	96.73	96.43	96.07	95.93	96.16	96.20	97.84
Si	4.00	4.00	4.00	4.00	4.00	4.00	4.00	4.00	4.00	4.00	4.00
Al^{IV}	--	--	--	--	--	--	--	--	--	--	--
Al^{VI}	0.49	0.79	1.02	1.21	0.80	1.04	1.26	1.55	1.05	1.24	1.37
Ti	3.54	3.19	2.95	2.70	3.13	2.82	2.44	2.22	2.77	2.57	2.55
Fe^{3+}	0.03	0.04	0.06	0.06	0.06	0.08	0.09	0.09	0.10	0.09	0.12
Mg	--	--	--	--		0.01					
Mn	--	--	--	--	--	0.01	0.01	--	0.01	--	0.01
Ca	4.07	3.98	4.01	3.84	4.02	3.98	3.84	3.96	3.92	3.86	4.00
Na	--	0.01	--	0.01	--	--	--	--	0.01	0.01	--
K	--	--	--	0.01	--	0.01	0.01	0.02	0.01	0.02	0.01
Ba		0.01		--	0.01	0.01	0.01	0.01			
# Anals.	1	3	6	1	2	10	9	1	2	9	1

Structural formula calculations assume Si = 4.00.

123-4B: All analyses are of titanite crystals growing into voids in feldspars. 146-4: Includes titanites in plagioclase crystals, in shears and brecciated zones, averaged together. 173-6B: (1) narrow band of titanite in groundmass; (2) bladelike crystals associated with plagioclase or chlorite; (3) with chlorite, replaces small clast.

Table 6, continued. Titanite Analyses

	Well B										
	5-19			12-4			29-28		60-3		
	(1)	(2)	(3)	(1)	(2)	(3)	(1)	(2)	(1)	(2)	(3)
SiO_2	30.02	30.56	30.14	29.86	30.20	30.42	30.80	31.01	31.38	30.96	31.44
TiO_2	35.94	30.79	27.75	34.53	30.33	27.83	29.82	27.70	33.58	31.12	27.39
Al_2O_3	2.17	5.78	8.09	3.84	5.75	7.59	5.99	6.99	4.06	5.33	7.66
Fe_2O_3	0.78	1.02	0.78	0.67	1.00	0.84	1.47	1.84	0.41	0.49	0.71
MgO	--	0.01	--	--	0.04	0.05	0.13	0.30			
MnO	0.03	0.01	0.03	0.02	0.09	0.15	0.13	0.14	0.04	0.05	0.08
CaO	29.08	28.27	28.08	28.58	28.00	28.61	27.68	27.18	28.34	28.45	28.99
Na_2O	--	0.01	--	--	0.01	--	0.03	0.04	--	0.01	--
K_2O	0.02	0.06	0.07	0.04	0.11	0.06	0.22	0.22	0.13	0.19	0.24
BaO									0.27	0.22	0.18
Total	98.04	96.50	94.94	97.54	95.93	95.55	96.27	95.42	98.21	96.82	96.69
Si	4.00	4.00	4.00	4.00	4.00	4.00	4.00	4.00	4.00	4.00	4.00
Al^{IV}	--	--	--	--	--	--	--	--	--	--	--
Al^{VI}	0.34	0.89	1.27	0.61	0.90	1.18	0.91	1.06	0.61	0.81	1.15
Ti	3.60	3.03	2.77	3.48	3.03	2.76	2.92	2.69	3.22	3.02	2.62
Fe^{3+}	0.08	0.10	0.08	0.07	0.10	0.08	0.14	0.18	0.04	0.05	0.07
Mg	--	--	--	--	--	0.01	0.03	0.06			
Mn	--	--	--	--	0.01	0.01	0.02	0.02	--	0.01	0.01
Ca	4.15	3.97	3.99	4.10	3.98	4.03	3.85	3.76	3.87	3.94	3.95
Na	--	--	--	--	0.01	--	0.01	0.01	--	--	--
K	--	0.01	0.01	0.01	--	0.01	0.04	0.04	0.02	0.03	0.04
Ba									0.01	0.01	0.01
# Anals.	1	6	1	1	4	2	3	3	1	3	1

Structural formula calculations assume Si = 4.00.

5-19: All analyses are of small crystals in feldspars. 12-4: (1) titanite associated with chlorite + epidote + allanite; (2) and (3) are associated with white mica, chlorite, or chlorite + allanite + epidote, averaged together. 29-28: Titanites associated with chlorite-filled veinlets. 60-3: Titanite-rich bands in groundmass.

that the replacement of Ti by Al and Fe^{+3} does not exceed 30 mole percent, many of the analyses in Table 6 have somewhat larger amounts of substitution. The low oxide sums of several titanite analyses probably reflect the substitution of $(OH)^-$ for oxygen, in combination with the Ti-Al exchange. The titanite crystals contain ≈0.3–1.8 wt% Fe_2O_3, and the crystals with the highest Fe contents are usually intergrown with chlorite. Potentially, titanite can contain large amounts of rare-earth elements (REE) (e.g., Exley, 1980; Hughes et al., 1997). However, SEM examination of many titanite crystals in the three wells yielded no evidence of REE in these crystals (Fig. 6a).

The substitution of Al into titanite has been correlated with various physical and chemical parameters. Of most significance to this study, Coombs et al. (1976) and Kawachi et al. (1983) reported elevated Al-contents for titanites from low-grade metamorphic rocks of the pumpellyite-actinolite and greenschist facies. They proposed that the stability of the $CaAlSiO_4(OH)$ component in the titanite structure might be expected to decrease with increasing temperature and/or decreasing P_{H2O}. The generally higher Al contents of well A titanites would be consistent with the slightly lower measured temperatures of well A compared to well B. This suggests the possibility that the Al content of titanite might have some potential as a geothermometer, if all other competing controls on composition, such as mineral assemblage, fluid pressure, and overburden pressure can be identified and quantified. For example, Cho et al. (1988) suggested that the coexistence of titanite with a TiO_2 mineral should maximize the Ti-content of titanite. The most Al-rich analysis in Table 6 does come from a sample (146-4) in which TiO_2 was not observed (Table 1); even so, the TiO_2-bearing core sample 173-6B has titanite containing >9 wt% Al_2O_3.

Epidote-group Minerals. Both allanite and epidote have been found in the core samples. Allanite is the epidote-group mineral that contains at least 10 wt% rare-earth elements (REE). Allanite has been identified in nearly every core sample. It is nearly always associated with titanite, generally occurring as tiny, bladed crystals scattered around the edges of the titanite (Fig. 5a). Minute, rounded crystals of allanite occur as inclusions in vein quartz in well C and

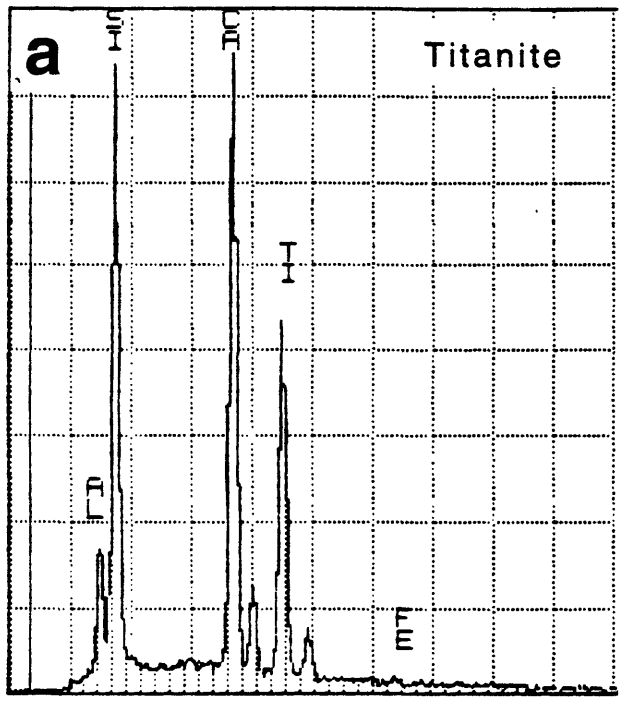

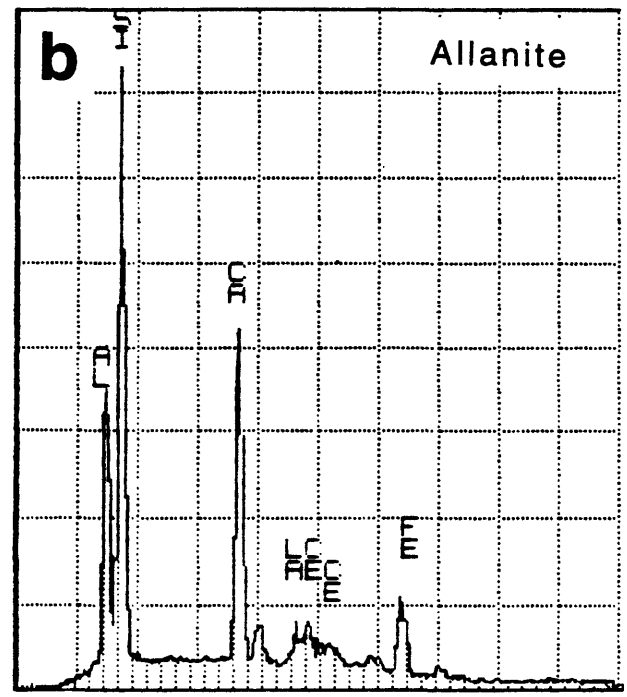

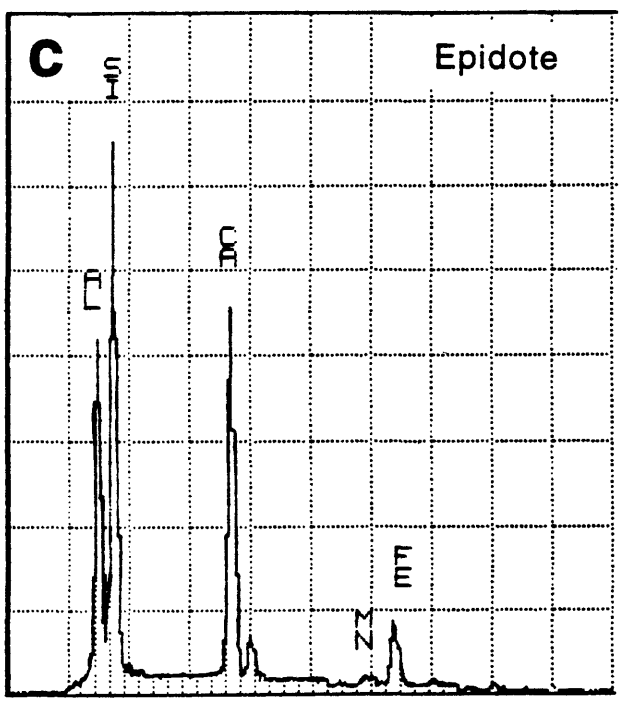

All element spectra are from minerals in 12-4, well B.

Figure 6. Element spectra of a) titanite, b) allanite, and c) epidote obtained during SEM analysis. Allanite alone has measurable amounts of REE, principally cerium and lanthanum; the titanite has a pronounced Al peak, and the epidote a strong Fe peak.

they extend into void spaces from the adularia-rich deposits of well B (Fig. 5c). Some of the dissolution cavities in feldspars from well A have small, irregularly shaped allanite crystals along the edges. Cerium (Ce) and lanthanum (La) are the principal rare-earth elements in the allanites, as indicated by SEM analysis, with Ce consistently more abundant than La (Fig. 6b). Such REE abundances appear to be characteristic of allanite (Deer et al., 1986). Epidote and allanite are related by the coupled substitution: Ca Fe^{+3} = $REE^{+3}Fe^{+2}$, and allanite is the only epidote-group mineral to contain significant amounts of ferrous iron. The anhydrous totals of the allanite analyses in Table 7 range between ≈74 and ≈88 wt%. The low oxide sums may be largely attributable to the missing REE contents, but the lowest sums may additionally reflect the very small size of some crystals. Partial structural formulas for the allanite analyses were calculated assuming Si = 3.0 atoms, because there is characteristically little substitution of Al or other elements for Si. The Ca and Al contents decrease with decreasing oxide sums, but the Fe-contents are relatively uniform between ≈0.7 and 0.8 atoms in the structural formula. Manganese and Ti are common minor elements, at 0.5–2.0 wt% MnO and 0.2–1.0 wt% TiO_2.

Epidote is considerably less abundant than allanite; its occurrence is restricted to several of the well B core samples. Where it has crystallized, the epidote is characteristically intergrown with allanite, in textures sometimes suggestive that epidote rims the allanite (Fig. 5c). Other associated minerals include titanite and patches of adularia ± quartz ± chlorite. Most of the epidote occurrences are too small for microprobe analysis, but moderate-sized crystals from 12-4 and 71-3 gave reasonable results (Table 8). Their compositions are similar overall, with about 12.5–13.3 wt% Fe_2O_3 (0.75–0.80 atoms of Fe in the structural formula or ≈25 mole % of the Fe end member $Ca_2Fe_3Si_3O_{12}(OH)$) and 0.3–0.8 wt% MnO. Both the anhydrous totals and the SEM spectra (Fig. 6c) suggest that the epidotes have a negligible rare earth element content. Coexisting allanite and epidote have been reported from other geothermal fields (e.g., Bird et al., 1988), but in those occurrences the epidote is much more abundant than the allanite.

Table 7. Allanite Analyses

	Well A		Well B					
	146-4	173-6B	12-4		60-3			71-3
			(1)	(2)	(1)	(2)	(3)	
SiO_2	34.32	34.43	33.91	32.58	35.54	34.23	31.05	32.05
TiO_2	0.39	0.06	1.04	0.17	0.31	0.26	0.54	0.43
Al_2O_3	19.90	22.16	19.86	21.06	20.92	19.51	16.75	17.21
FeO	10.50	10.55	10.84	9.77	9.73	9.43	10.24	10.31
MgO			0.09	0.07				0.23
MnO	1.94	0.52	0.61	2.06	1.07	1.31	0.91	1.88
CaO	15.73	19.14	19.45	15.50	18.71	15.86	12.74	13.69
Na_2O	0.02	--	--	--	--	0.07	0.01	--
K_2O	0.06	0.06	0.03	0.02	0.29	0.29	0.24	0.04
BaO	--				--	--	--	0.03
Total	82.86	85.79	85.83	81.23	86.57	80.96	72.48	75.87
Si	3.00	3.00	3.00	3.00	3.00	3.00	3.00	3.00
Al^{IV}	--	--	--	--	--	--	--	--
Al^{VI}	2.05	2.28	2.07	2.29	2.08	2.02	1.91	1.90
Ti	0.03	--	0.07	0.01	0.02	0.02	0.04	0.03
Fe^{2+}	0.77	0.77	0.80	0.75	0.69	0.69	0.83	0.81
Mg			--	0.01				0.03
Mn	0.14	0.04	0.03	0.16	0.08	0.10	0.07	0.15
Ca	1.47	1.79	1.84	1.53	1.69	1.49	1.32	1.38
Na	--	--	--	--	--	0.01	--	--
K	0.01	0.01	--	--	0.03	0.03	0.03	--
Ba	--				--	--	--	--
# Analyses	1	1	1	1	1	2	1	3

Structural formula calculations assume Si = 3.00.
Allanites from well C were too small to analyze.

Table 8. Epidote Analyses

	Well B			
	12-4			71-3
	(1)	(2)	(3)	
SiO_2	37.08	37.49	37.12	38.25
TiO_2	0.60	0.11	--	0.06
Al_2O_3	22.58	27.24	24.47	23.06
Fe_2O_3	13.26	9.31	12.47	12.91
MgO	0.10	0.03	--	0.03
MnO	0.33	0.79	0.33	0.66
CaO	23.32	22.87	23.59	22.82
Na_2O	--	--	--	0.02
K_2O	0.04	0.04	0.03	0.02
BaO				0.01
Total	97.31	97.88	96.76	97.84
Si	2.98	2.95	2.95	3.05
Al^{IV}	0.02	0.05	0.05	--
Al^{VI}	2.12	2.47	2.25	2.16
Ti	0.04	0.01	--	--
Fe^{3+}	0.80	0.55	0.75	0.77
Mg	0.01	--	--	--
Mn	0.03	0.05	0.02	0.05
Ca	2.01	1.93	2.01	1.95
Na	--	--	--	--
K	--	--	--	--
Ba				--
# Analyses	4	1	1	5

Structural formula calculations assume anhydrous O = 12.5.
All analyzed epidotes are associated with allanite + chlorite + titanite + adularia.

Anhydrite. The identity of the mineral was confirmed by X-ray-diffraction analysis of large crystals pried from some well B veins. Anhydrite only appears in well B (Table 1), where it is generally one of the latest minerals to crystallize and also one of the coarsest grained. It is contemporaneous with adularia. The large anhydrite crystals that span the open veins generally mantle the medium-grained, euhedral adularia crystals lining vein walls; but concentric arrays of tiny adularia crystals are contained in the anhydrite, and the surfaces of some anhydrite crystals are partly coated with adularia. Narrow veins of anhydrite cut through some of the wide bands of fine-grained adularia + quartz. A few, relatively small, anhedral crystals of anhydrite are scattered along the edges of the adularia veins and so may be slightly older than the very large crystals.

Fe and Ti oxides. Each well has a distinctive assemblage of Fe and Ti oxides. In well C, presumably igneous Fe-oxide crystals, probably magnetite, have a corroded appearance, and no new Fe-oxides have formed in association with the hydrothermal alteration. No ilmenite was found, but TiO_2 is a vein-filling mineral and also is associated with the white mica that replaces biotite phenocrysts. As seen in Figure 7a, TiO_2 also forms a partial border along the sides of well C calcite veins. The identity of the TiO_2 mineral is not certain, but the larger crystals have a reddish-brown color and the blocky habit suggestive of a tetragonal mineral. Both of these features are consistent either with the polymorph anatase, which has been reported in other geothermal areas (e.g., Yau, 1986) or, alternatively, with rutile.

In well A, igneous magnetite is partly dissolved or reacted, but several of the fracture sets and associated breccia zones in the three deepest core samples are lined with a red-tinged Fe oxide, probably hematite (Fig. 7b). Based on SEM analysis, the hematite coatings contain almost no impurities, whereas the relict igneous magnetites have a noticeable Ti peak. Microprobe analyses of some of the magnetite crystals confirm the presence of 5–7 wt% TiO_2 and as much as 1.5 wt% Al_2O_3. The two intermediate-depth well A core samples contain an Fe-Ti oxide that was identified as ilmenite on the basis of equal Fe and Ti peak heights in SEM spot analyses. Ilmenite is relatively abundant in 146-4, where it is principally associated with

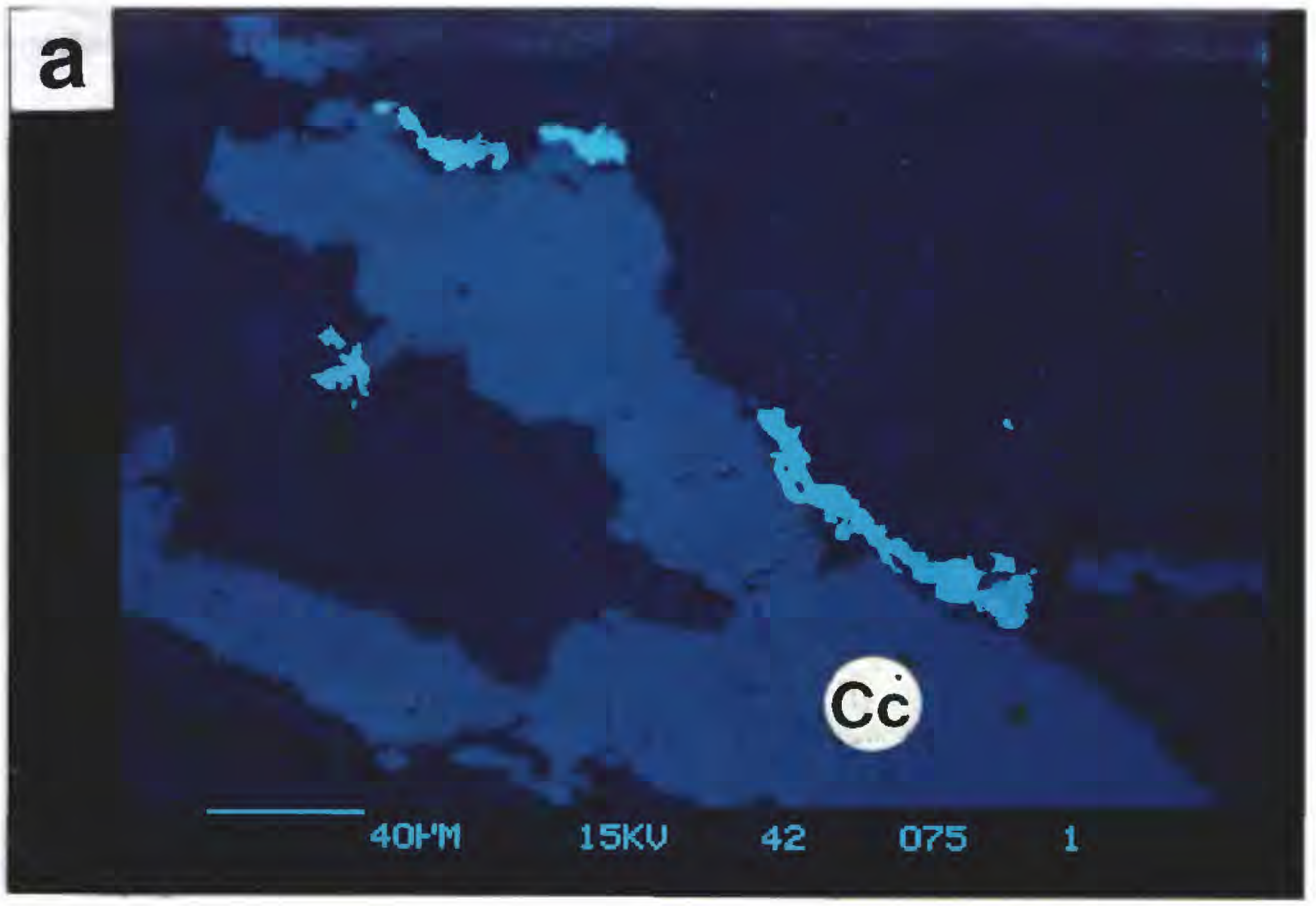

Figure 7. Back-scattered electron SEM images of Fe and Ti oxides. a) Calcite (Cc) vein in 49-5, well C, partly rimmed by TiO_2. b) Brecciated tuff adjacent to a fracture in 146-4, well A; the bright mineral filling the cracks is hematite (H). Q = quartz; E = epoxy.

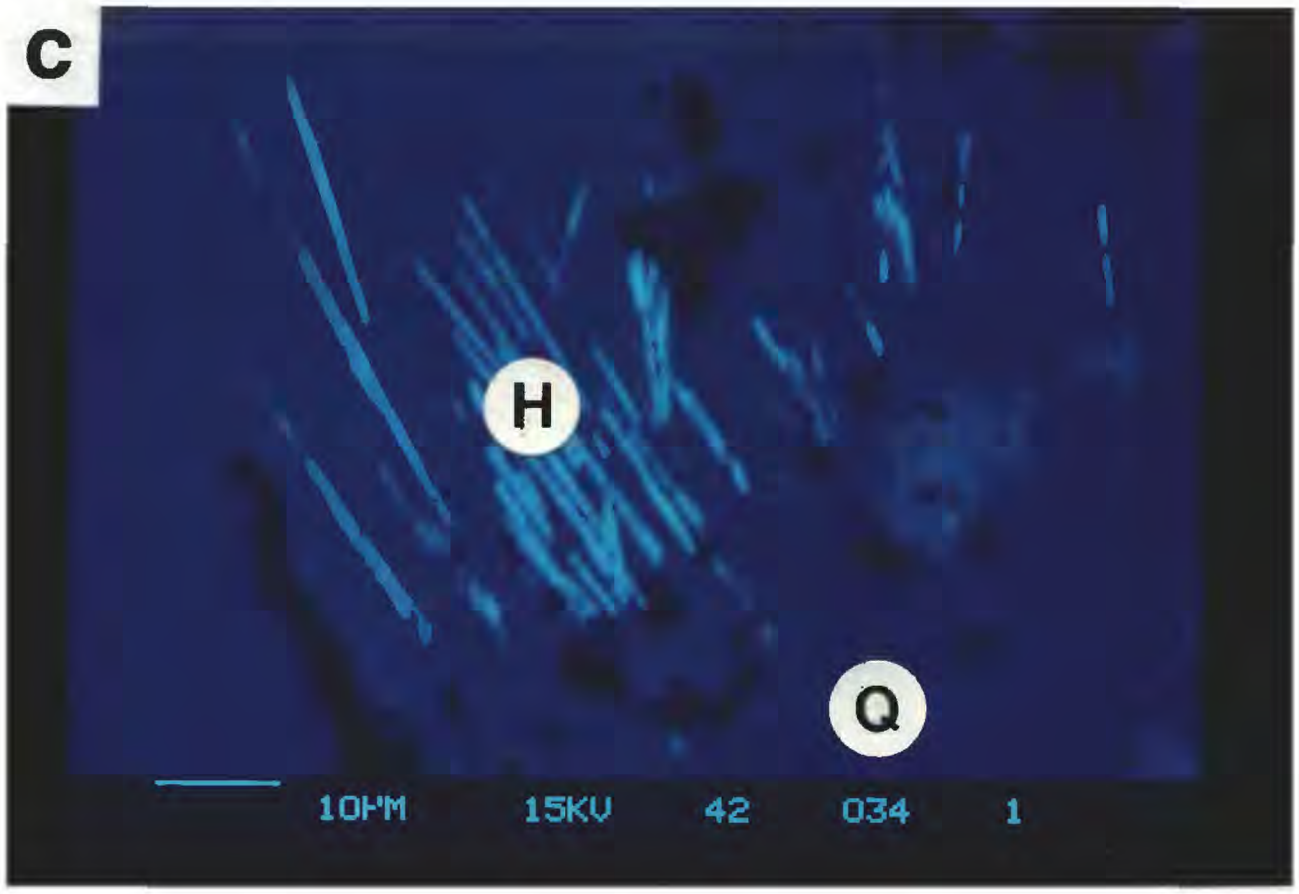

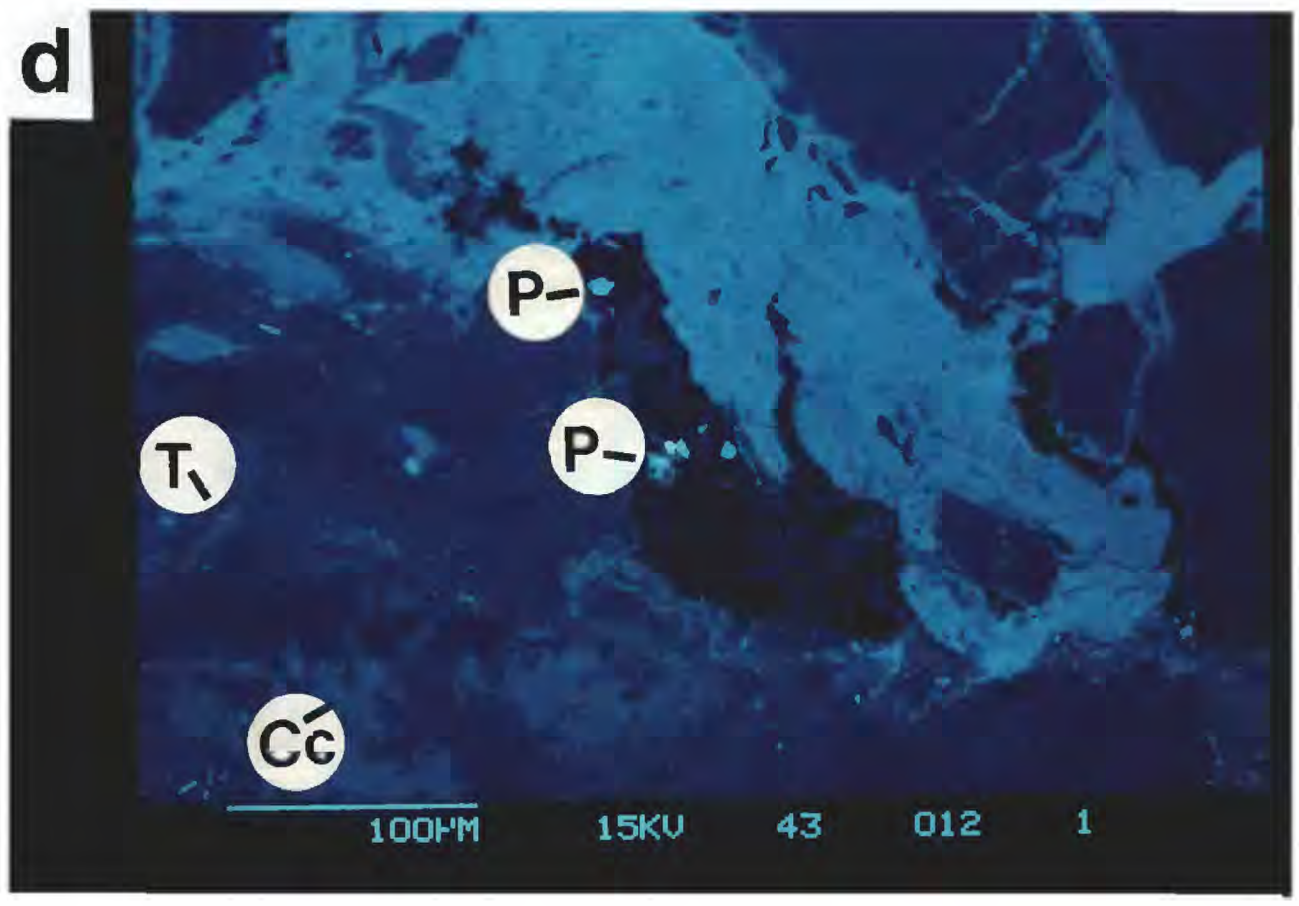

Figure 7, continued. c) Rods of Fe-oxide (H) in hydrothermal quartz crystal near void in 5-19, well B. d) Brecciated zone in fracture, 146-4, well A, cemented with Fe-oxide, calcite, and some titanite (T). Bright specks in cavity are pyrite (P) and an unknown Cu-Sn±S phase. Bright spots in the tuff are Fe-oxides containing some Ti.

chlorite or white mica but also occurs as tiny rods extending out from apatite crystals. The shallowest and deepest well A samples contain TiO_2. Two well A core pieces also have Fe-Ti oxides in which the Fe peak is about twice the size of the Ti peak in SEM spot analyses. This mineral was tentatively identified as pseudobrookite, Fe_2TiO_5 (Deer et al., 1966) (Table 1).

Although pyrite is the principal Fe-bearing accessory mineral in well B, small crystals of Fe-oxide form inclusions in quartz that has crystallized in veins (Fig. 7c) and altered patches in four of the well B core samples (Table 1). One microprobe analysis from 5-19 was essentially pure Fe-oxide, similar to the hydrothermal Fe-oxides of well A. No ilmenite was identified in well B, but scattered occurrences of TiO_2 were found. Only a few TiO_2 analyses were obtained, because of their very small grain size. The best analysis is nearly pure TiO_2, with about 0.5 wt% each Fe_2O_3 and BaO as the principal substitutions.

Sulfides. The principal sulfide mineral is pyrite, which is abundant in all the well B samples, relatively abundant in the well C sample, but found only in trace amounts in well A (Fig. 7d). Pyrite is common in veins and also is scattered throughout the surrounding rock. Concentrations of pyrite occur in some clasts as well as in some sheared-looking bands. In one sheared zone in well B (122-5), some of the pyrite crystals are partly rimmed by titanite.

The occurrence of pyrite in well A is notable. Trace amounts of pyrite were found in 146-4 in association with equally small amounts of a Cu-Sn±S phase. As illustrated in Figure 7d, the pyrite and the copper-tin minerals may have been among the latest to crystallize. They are found in the large, brecciated fracture zone and in narrow, open, subsidiary fractures that extend outwards at large angles to that fracture zone. The breccia in Figure 7d has been cemented principally with hematite and calcite, and the pyrite and Cu-Sn minerals are tiny crystals scattered in the remaining unfilled areas.

Minor occurrences of galena (PbS), consisting of one or two crystals per thin section, were found in core from all three wells. Single sphalerite (ZnS) crystals were found in core from wells B and C, and traces of chalcopyrite or some other Fe-Cu-S mineral were identified in 5-19 (well B).

Apatite. Apatite may be an accessory igneous mineral in the tuffs, but it also is a relatively common hydrothermal mineral. Euhedral apatites are associated with other calcium-bearing minerals such as titanite, epidote-group minerals, or calcite. Apatite is also found with other vein minerals such as adularia and chlorite, and it grows along some of the open veins of wells B and C. Many of the partly altered igneous magnetites are surrounded by numerous small apatite crystals. Apatite is generally less abundant than titanite in these samples but probably more abundant than allanite.

Zircon. A few scattered zircon crystals are present in the core samples. As with apatite, at least some occurrences are clearly hydrothermal in origin. Some zircons form small, euhedral crystals in vein-filling assemblages.

Other Minerals. The core samples are notable for some of the index minerals that they lack, namely actinolite, biotite, garnet, and clinopyroxene. One small biotite crystal was found in well B sample 71-3; however, this crystal is probably a relict mineral in a metasedimentary clast in which the other phyllosilicates have been chloritized. During SEM examination of a thin section from 60-3 (well B), a single tiny crystal containing Si, Ca, Fe, Mg, and Al in descending order of peak heights was found in one of the fine-grained adularia + quartz bands. This crystal could be garnet, actinolite, or clinopyroxene, but it was too small to analyze with the microprobe.

Summary and Comparison of Wells

The rhyolite ash-flow tuffs comprising the core samples contain large phenocrysts of plagioclase and quartz and generally smaller phenocrysts of K-feldspar. The igneous plagioclase composition is as calcic as $Ab_{50}An_{50}$, and the igneous K-feldspar is a sodium-rich sanidine ($\approx Ab_{30}Or_{70}$). The very large quartz phenocrysts of 123-4B (well A) are heavily fractured, but the pieces remain close together and define a crude crystal outline. The feldspar and quartz crystals of other samples are also variably fractured or broken, but not nearly as dramatically

as those in 123-4B. Mafic igneous phenocrysts have all been pseudomorphically replaced by alteration minerals; based on their crystal outlines and some examples of preserved cleavage planes, they originally were biotite and amphibole. Small euhedral magnetites are scattered throughout the samples. The tuffs also contain a wide variety of lithic fragments of volcanic rock, a few possible plutonic igneous crystals and rock fragments, and fragments of foliated, quartz- and mica-rich metasedimentary rock. The fine-grained groundmass generally has a very dark, grainy appearance. The groundmass of a few samples has a spherulitic character, and in several samples the outlines of former glass shards are visible.

The hydrothermal vein assemblages and the types of wall rock alteration vary from well to well, with depth within a given well, and with time. The hydrothermal assemblage of well C is distinctive. The predominant vein minerals are quartz and calcite, with moderate amounts of white mica and minor pyrite, apatite, TiO_2, titanite, allanite, and sphalerite ± albite ± K-feldspar. The plagioclase phenocrysts have been thoroughly albitized. K-feldspar phenocrysts are partly replaced by albite + white mica along cracks, and unreplaced K-feldspar has a low-Na composition of Ab_4Or_{96}. White mica is also the major replacement of mafic phenocrysts such as biotite; only a trace amount of chlorite is present. A TiO_2 mineral occurs with white mica in altered biotites and forms bands in the country rock adjacent to calcite veins. Igneous magnetites are partly dissolved, and pyrite — but no hematite — has crystallized. The few tiny allanite crystals present generally occur as inclusions in vein quartz or in association with calcite. The prominent fractures and many of the minor fractures in the well C sample are only partly filled, leaving considerable void space.

Calcite and chlorite are important fracture-filling minerals in well A. Quartz is also a common vein mineral, but its most common occurrence is in the smaller veins. Many phenocrysts of plagioclase and K-feldspar have been largely dissolved, particularly in the shallowest sample. The amount of dissolution decreases progressively with increasing depth in the well. The dissolution may have initially involved inclusions in the feldspars, but the large jagged outlines of many of the cavities suggest that a considerable amount of feldspar was also

removed. Numerous titanite, some allanite, and a few quartz crystals grow into the solution cavities from the edges. Remnants of the original plagioclase and K-feldspar crystals appear to have recrystallized, because they have euhedral terminations along the voids. In addition, a few small, possibly separate crystals of feldspar are intergrown with the titanite crystals lining the cavities. These textures suggest that over time the fluids became saturated or supersaturated with respect to both feldspars. The plagioclase remnants have albite compositions, but a small, newly crystallized plagioclase in one cavity has an oligoclase composition.

The variety of iron- and titanium-rich minerals is greatest in well A. Igneous magnetite crystals are partly resorbed, but hematite is an abundant fracture-filling mineral, often associated with calcite. Ilmenite commonly is intergrown with the K-mica replacing some biotite phenocrysts. Other biotites that were replaced by chlorite + titanite + allanite have ilmenite occurring just outside the phenocryst outlines. TiO_2 and Fe-rich TiO_2 are also present; some of these crystals are associated with calcite veins and also with apatite, titanite, and chlorite. Various other ratios of Fe and Ti in these oxides were found during SEM examination, including Ti = 2Fe and Ti = 3Fe. Those with Fe = 2Ti may be pseudobrookite (Fe_2TiO_5). The well A samples contain almost no sulfide minerals but, notably, a few late-formed, very small crystals of pyrite along with a copper-tin mineral containing variable amounts of sulfur were encountered in the remaining void spaces of a hematite-lined, brecciated zone. The pyrite and the Cu-Sn phase are also the only hydrothermal minerals in very fresh-looking, elongate cracks that intersect one of the main hematite-lined fractures at nearly right angles.

Well A core samples display the best evidence for shearing, characterized by bands of granulated phenocrysts (Fig. 8a). Fine-grained plagioclase pieces in sheared zones of 173-6B (Fig. 8a) retain their very calcic compositions; either the shearing was quite recent or few fluids moved through the shear to albitize the feldspars. These granulated, relatively narrow shears may represent one end of a spectrum of fracturing/shearing, of which the other end

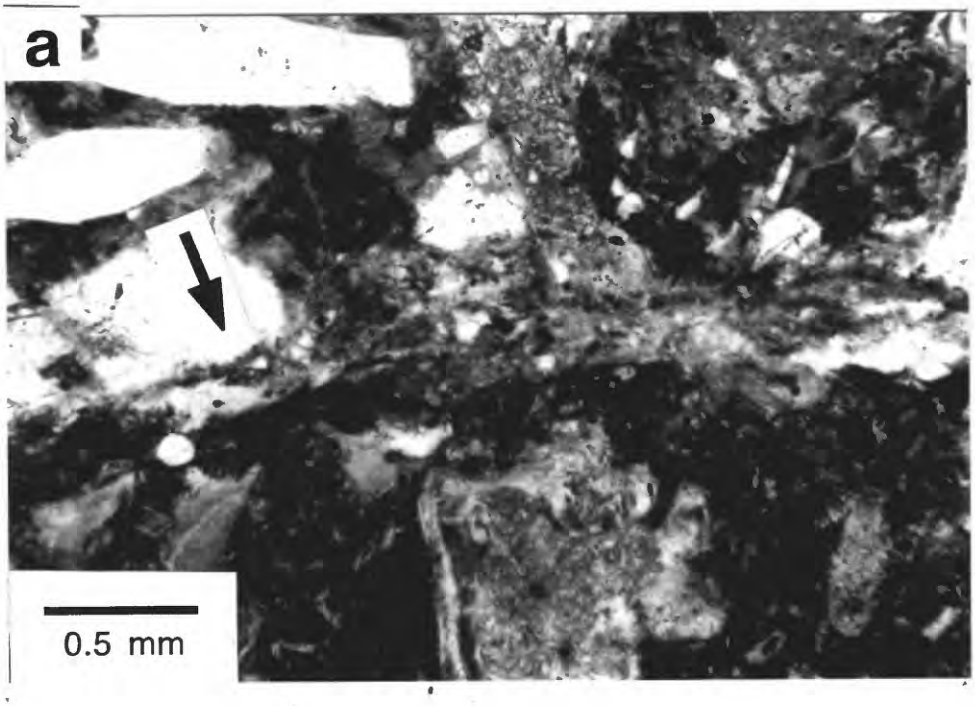

Figure 8. a) In 173-6B, well A, a sheared zone of moderate width (indicated by arrow) extends from left to right across center of photo. Quartz and feldspar crystals cut by such shears are granulated, but the feldspar fragments retain their igneous compositions; plane-polarized light.

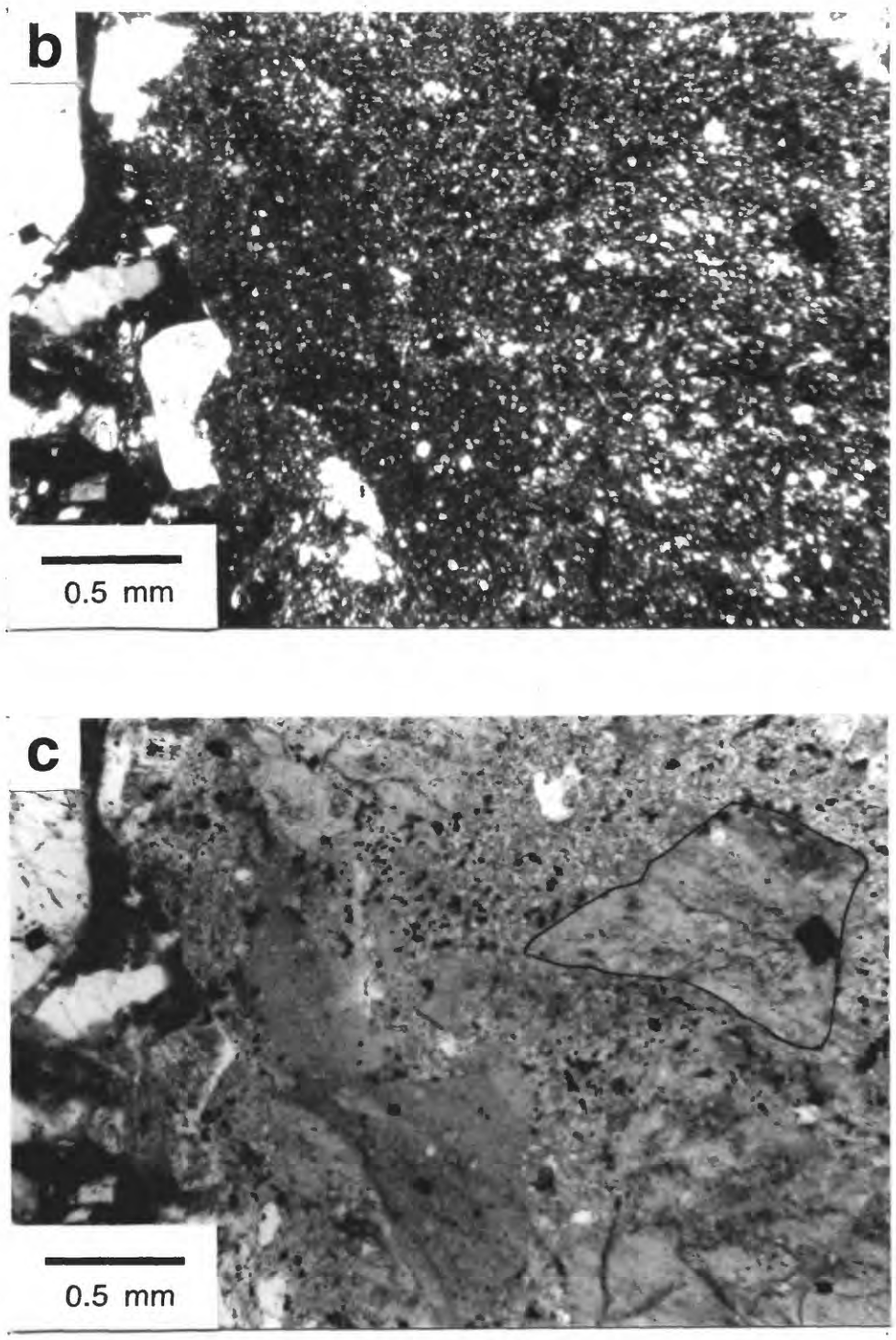

Figure 8, continued. b) and c) Brecciated and heavily cemented zone in 29-28, well B, viewed b) under crossed polarizers and c) in plane-polarized light. The phenocryst-rich tuff on the left is part of a large fragment encased in hydrothermal cement that is itself brecciated. As better seen in c), more uniform-looking, angular fragments (one has been outlined) are suspended in a mottled matrix of the same authigenic minerals.

comprises the commonly much wider zones of brecciated tuff that have well-defined boundaries with the adjoining, undeformed rock. Mineral deposits line cracks and voids across the entire width of some breccia zones, whereas in others the deposits of hematite and calcite — and by inference the fluid flow — are concentrated along the outer edges. By contrast, neither brecciated nor granulated zones are much in evidence in the one well C core sample.

The mineralization in well B varies with depth and with time. Quartz and calcite are the principal vein- and cavity-filling minerals in the two shallowest samples (5-19 and 12-4), whereas adularia is the dominant hydrothermal mineral at greater depths. Some adularia is present in the shallowest samples, and moderate amounts of anhedral to euhedral quartz are found in all the deeper-level adularia veins. Most of the deeper well B core samples also contain numerous calcite veins, but they may have developed at an earlier stage. Several of these calcite veins are cross-cut by adularia veins, and in a brecciated zone of 91-13 the calcite only occurs within the fragments of tuff that are cemented together by adularia + quartz + chlorite + titanite. Euhedral calcite crystals in an intermediate-stage vein in 122-5 may be breaking down; the crystal outlines are embayed by small crystals of adularia, quartz, and chlorite and also partly rimmed by titanite, which may be taking up the liberated calcium.

Modest dissolution of feldspar phenocrysts may have occurred similar to that described for well A, but most of the cavities are now filled with aggregates of feldspar + quartz and/or chlorite-bearing assemblages. As a result, several plagioclase phenocrysts have a mosaic appearance. The most calcic plagioclase composition from this well is $Ab_{65}An_{30}Or_5$; assuming that well B and well A plagioclase compositions were similar initially, all the well B plagioclase phenocrysts have been at least somewhat modified. Plagioclase phenocrysts caught up in or occurring alongside veins have been more thoroughly albitized, and some of them also have an overgrowth of adularia. Although subordinate to adularia, albite or a slightly more calcic plagioclase does occur as a hydrothermal mineral in some of the adularia veins. Of these, the more anorthite-rich plagioclase crystals may be younger than the more albite-rich ones.

Chlorite is the principal phyllosilicate mineral throughout well B. In the shallowest samples, chlorite is generally associated with calcite, and it is a moderately abundant mineral in the deeper-level, adularia-rich veins and patches. Chlorite is also the main replacement mineral of mafic igneous crystals. Although K-mica is moderately abundant in the smaller veins of the two shallowest core samples, at deeper levels it usually is confined to particular clasts. The K-mica in metasedimentary rock fragments is probably a relict mineral. Pyrite is a common accessory mineral in veins and sheared zones, and concentrations of pyrite are found in some lithic fragments. Small igneous magnetites may be pseudomorphically replaced by clusters of tiny pyrite crystals. In addition to pyrite, hydrothermal Fe-oxides, probably hematite, also occur as inclusions in vein- and cavity-filling quartz.

True epidote was found only in well B. Relationships among titanite, allanite, and epidote suggest that titanite formed first and epidote last. Titanite is especially abundant along the edges of veins, and the crystals can be relatively large. Titanite crystals in 29-28 have cores of TiO_2. Allanites generally are present as bladed crystals scattered around the titanite, but several are intergrown with the outer parts of the titanite crystals. In turn, the epidote may rim the allanite crystals. Most of the allanite + epidote groupings occur with titanite, but a small number of composite crystals grow into void spaces from the edges of adularia veins.

The well B samples seem to contain a larger proportion of unfilled cavities and partly open veins than the samples from the other two wells. Several wide veins are only partly filled with minerals; characteristically large anhydrite crystals traverse the openings and the vein walls are lined with medium-grained, euhedral adularia crystals. Anhydrite appears only in well B, where it is one of the latest — as well as one of the largest — minerals to crystallize. Some fractures alternate between narrow, filled, fractured or sheared-looking segments and open spaces several millimeters wide. The well B samples, especially those from greater depths than 29-28, also contain a number of bands, some several millimeters wide, that consist of a matrix of fine-grained adularia + quartz + chlorite + titanite + pyrite with a scattering of relict igneous phenocrysts and lithic fragments. The sides of the bands are marked by coarse-

grained titanite + pyrite + allanite, and next to the sides the groundmass of the bands is somewhat coarser-grained and contains numerous open spaces. These fine-grained bands are interpreted to represent more thoroughly recrystallized versions of the brecciated and/or sheared bands common in well A.

Some well B samples show evidence of brecciation. The most extreme example is the entire 15-cm long 29-28 sample, which is an agglomeration of fragments of tuff up to 3 cm in length that are cemented together by wide, adularia-rich deposits (Fig. 8b, c). The cement, in turn, is itself brecciated — it consists of very fine-grained adularia assemblages in a slightly coarser-grained cement of the same minerals (Fig. 8c). More restricted zones of large tuff fragments, cement, and voids are found in other samples, such as 91-13 and 122-5. All of these zones are notable for containing a large amount of pore space. Either a considerable amount of tuff has been somehow removed, or the volume of these zones has increased. These episodes of brecciation and cementation are very probably tied to earthquakes centered on the Great Sumatran fault.

Estimates of Physical Conditions of Hydrothermal Alteration

Chlorite Geothermometer

In many studies, the composition of chlorite has been shown to vary with the pressure-temperature conditions of its formation. Cathelineau and Nieva (1985) studied the relationships between chlorite composition and temperature in the Los Azufres geothermal field of Mexico and constructed an empirical geothermometer based on the Al^{IV} content of chlorite. Cathelineau (1988) subsequently modified the geothermometer by incorporating additional data from the Salton Sea geothermal field. Crystallization temperatures were calculated for the chlorite analyses in Table 4, and the results are listed there and plotted in Figure 9. Most of the temperature estimates for wells A and B are in the range 280-360°C, but the two well A chlorite compositions from 146-4 yield temperatures of ≈250°C. If the data for the two

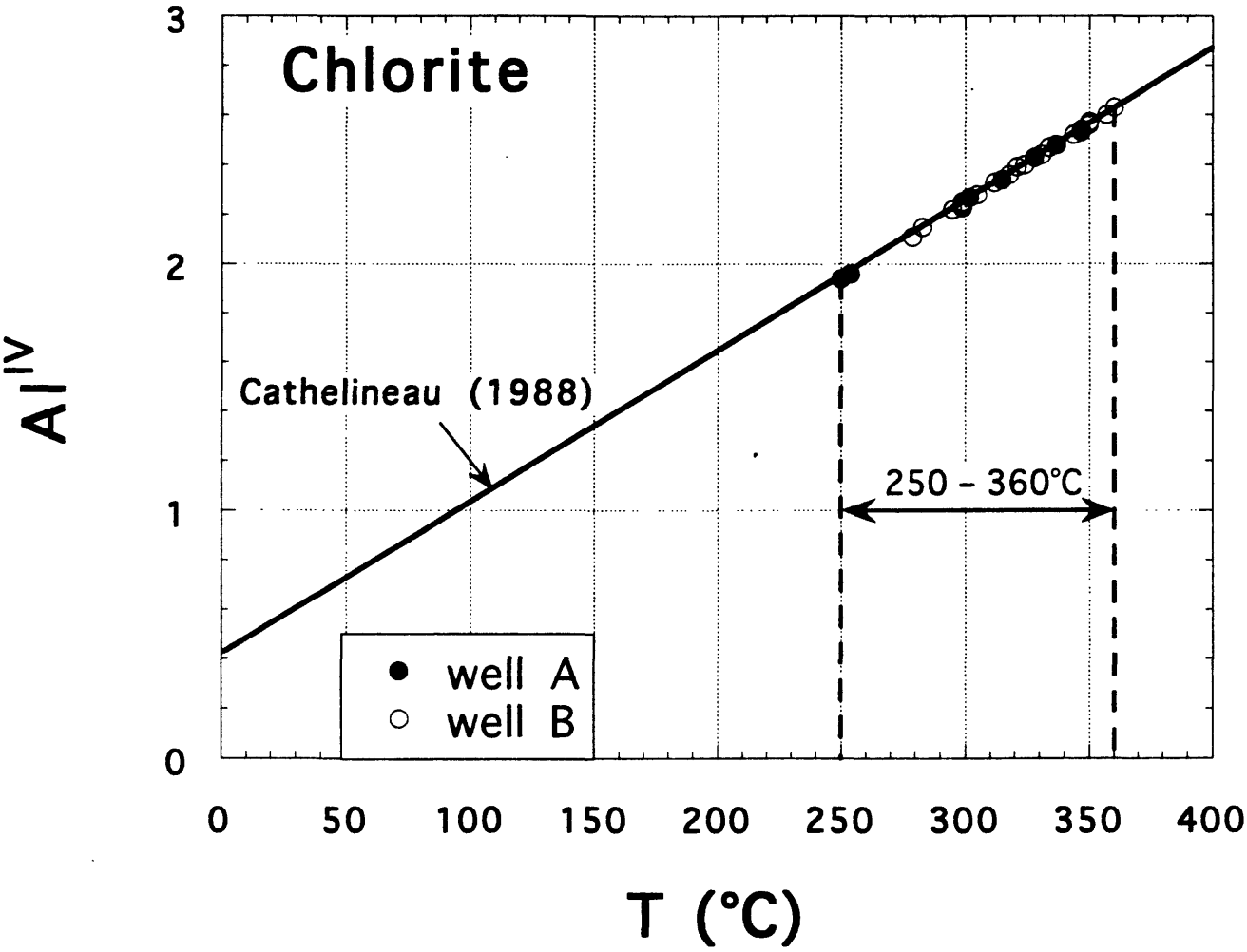

Figure 9. Range of crystallization temperatures calculated for chlorites from wells A and B using the chlorite geothermometer of Cathelineau (1988). The individual temperature estimates are presented in Table 4.

drillholes are considered separately, they yield average temperature estimates of 300 ± 50°C for well A and 320 ± 40°C for well B.

The drawback of the chlorite geothermometer is that factors other than temperature affect chlorite composition. Investigations of chlorite chemistry have demonstrated a very close correspondence between the Fe/(Fe + Mg) ratio of chlorite and that of the host rock (or of the fluid from which the chlorite crystallized). The Fe/(Fe + Mg) ratio, in turn, affects the Al^{IV} content, in that chlorites enriched in Fe also have high Al^{IV} contents (e.g., Kranidiotis and MacLean, 1987; Xie et al., 1997). Kranidiotis and MacLean (1987) relate this correspondence to structural adjustments accompanying the substitution of the larger Fe^{+2} ion for Mg in the octahedral sites, which allows more Al^{+3} to substitute for the smaller Si^{+4} ion in the tetradedral sites. The chlorites of wells A and B also show this compositional relationship (Figure 10a): those from 146-4 with Fe/(Fe + Mg) ≈ 0.2 have the lowest Al^{IV} contents, whereas the ones with Fe/(Fe + Mg) > 0.65 have the highest Al^{IV} contents. Consequently, the calculated crystallization temperatures for these chlorites are closely correlated with the Fe/(Fe + Mg) ratios (Fig. 10b).

The chlorite geothermometer of Cathelineau (1988) should yield reasonable temperature estimates for chlorites whose Fe/(Fe + Mg) ratios are similar to those used to calibrate the geothermometer. The Los Azufres chlorites initially utilized by Cathelineau and Nieva (1985) have Fe/(Fe + Mg) in the range 0.24—0.37, and those added by Cathelineau (1988, Table 1) from the Salton Sea geothermal field have Fe/(Fe + Mg) ratios between 0.44 and 0.58. The range of Salton Sea Fe-Mg contents of chlorite is very similar to the majority of chlorite analyses from wells A and B, which have Fe/(Fe + Mg) ranging principally from 0.4 to 0.6. In addition, the measured temperatures of crystallization of the Salton Sea chlorites were ≈250–320°C (Cathelineau, 1988, Table 1). These similarities suggest that the calculated temperatures are mostly reasonable, although chlorites with Fe/(Fe + Mg) ratios outside the range 0.4–0.6 probably need to be shifted to higher or lower temperatures.

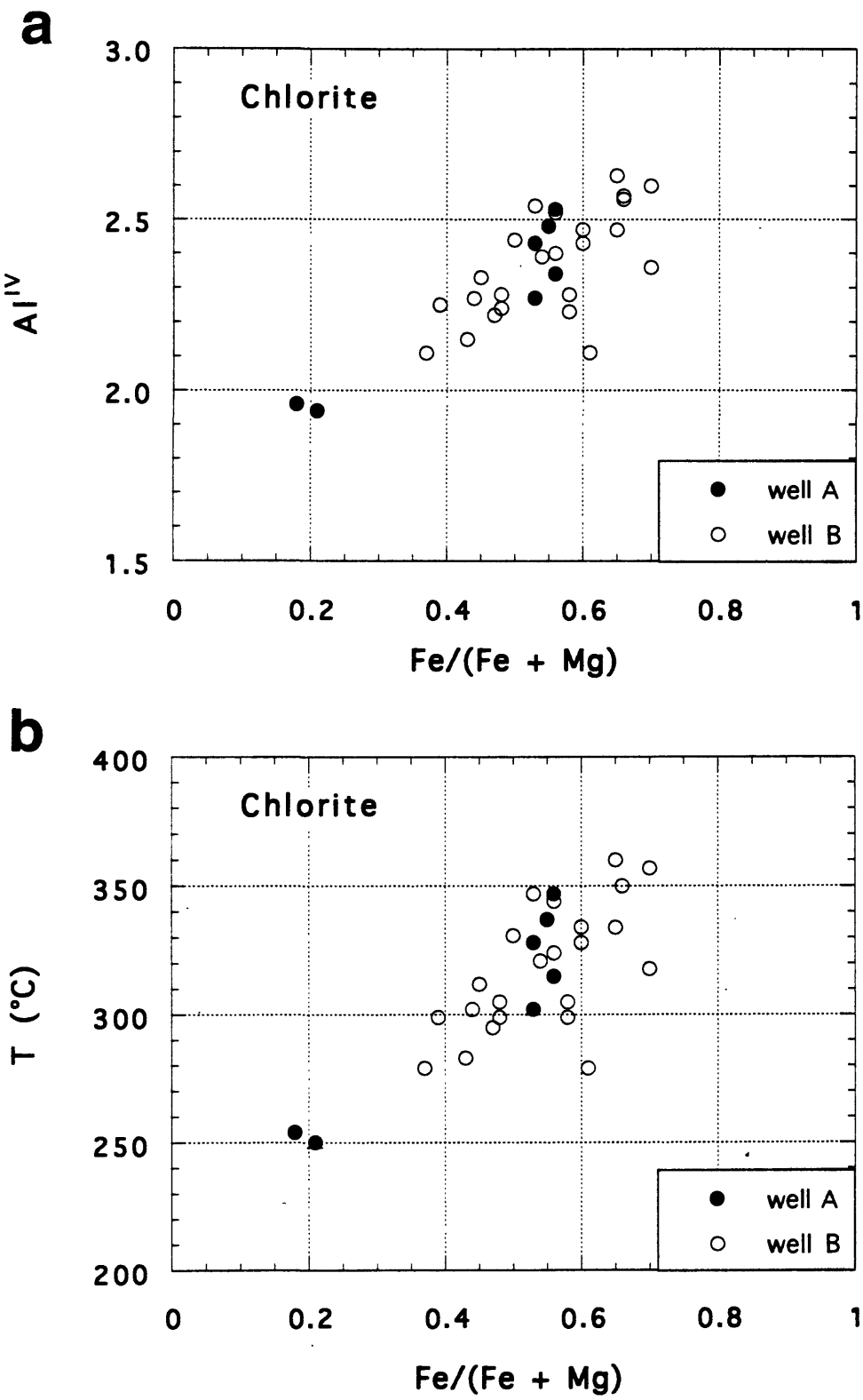

Figure 10. Correspondence between the Fe/(Fe + Mg) ratio of chlorite and its a) AL^{IV} content and b) calculated temperature of formation.

Kranidiotis and MacLean (1987) and Xie et al. (1997) have proposed corrections to the chlorite geothermometer that involve adjustments to the Al^{IV} content based on the Fe/(Fe+Mg) ratio. The equations of Xie et al. (1997) produce a large overcorrection, such that the lowest calculated temperature of ≈250°C from 146-4 becomes the highest (≈400°C) after the correction is applied. The correction proposed by Kranidiotis and MacLean (1987) was originally applied to the older, Cathelineau and Nieva (1985) geothermometer; their equations were adjusted to fit the revised geothermometer and then applied to the chlorite compositions in Table 4. This second set of revisions pulls all of the temperature estimates somewhat closer together; the modified temperature range for well A is 300 ± 30°C and that for well B is nearly identical at 305 ± 25°C. The slight differences in measured well temperature for these depth intervals (270–290°C for well A, and 300–320°C for well B) cannot be detected by the chlorite geothermometer. Nevertheless, the overall range of temperatures calculated with the chlorite geothermometer does correspond very well to the measured temperature range for the core samples. This consistency suggests that the measured fluid temperatures have not been perturbed by the drilling operations.

Comparison to Other Geothermal Fields

The mineral assemblages in wells A, B, and C and the reported temperatures for their depth intervals correspond very closely to those described by Muffler and White (1969) for three wells in the Salton Sea geothermal field, California (Fig. 11). The Salton Sea geothermal system is developed in sedimentary deposits of the Colorado River delta at the northern end of the Gulf of California and the East Pacific Rise. In the wells studied by Muffler and White (1969), illite-montmorillonite is completely converted to well-crystallized K-mica at a temperature of approximately 210°C. K-mica is abundant to ≈290–300°C, but its occurrence is sporadic at higher temperatures. Calcite is very common throughout the shallower parts of the sections, but it too disappears at temperatures above ≈290–310°C. In contrast, chlorite first appears at temperatures between 120 and 200°C in the different wells and becomes

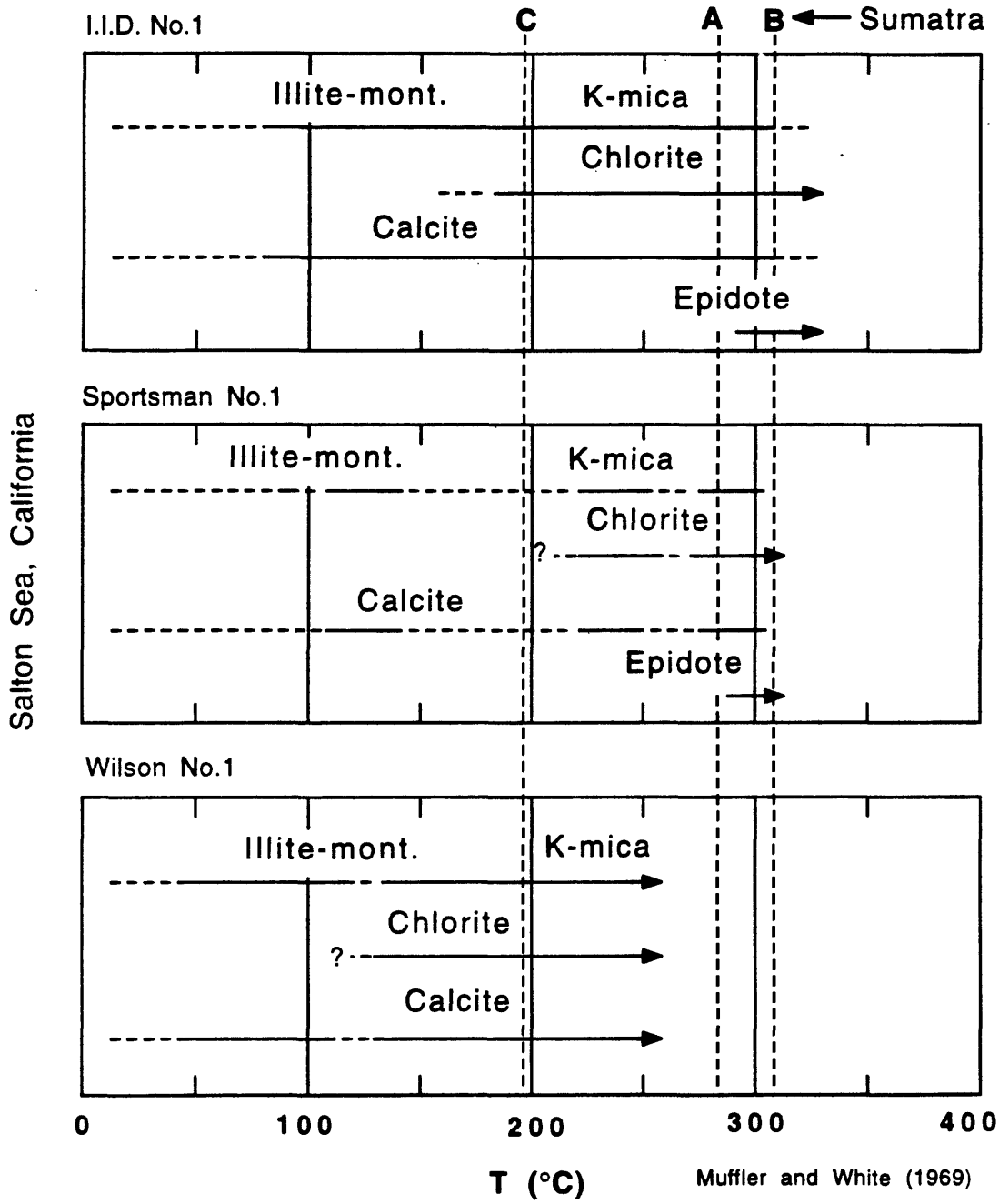

Figure 11. Summary of key mineralogical changes with increasing temperature in three wells from the Salton Sea geothermal field identified by Muffler and White (1969). The mineral assemblages and reported temperatures for the examined core samples from wells A, B, and C are consistent with the Salton Sea assemblages.

progressively more abundant with increasing depth and temperature to the roughly 320°C maximum of the core samples examined by Muffler and White (1969). Iron-rich epidote first appears and hydrothermal K-feldspar becomes abundant at temperatures near 290°C. In one Salton Sea occurrence, epidote that crystallized at 320°C contains 32 mole% of the Fe^{+3}-end member $Ca_2Fe_3Si_3O_{12}(OH)$, and it coexists with chlorite that has Fe/(Fe + Mg) = 0.32 (Keith et al., 1968).

The well C sample corresponds to the ≈200°C conditions in the Salton Sea wells (Fig. 11), where good K-mica and calcite are abundant and chlorite first begins to appear. The well A assemblages are consistent with the temperature interval just before the first appearance of epidote, where K-mica, chlorite, and calcite are all abundant. The well B core samples correspond to the epidote + adularia + chlorite-bearing Salton Sea rocks. The partial breakdown of earlier-formed calcite at the deepest levels of well B is consistent with the hypothesis that it crystallized at a lower temperature than that now attained in the well. Pyrite and hematite coexist in the Salton Sea wells, which suggests that oxygen fugacities are in the range 10^{-25} to 10^{-27} atm and sulfur fugacities are in the range $10^{-5.7}$ to $10^{-7.3}$ atm at a temperature of 325°C (Muffler and White, 1969). Well B contains the same Fe-minerals at a nearly the same temperature and should therefore have similar oxygen and sulfur fugacities. For the most part, well A fluids should be characterized by lower sulfur fugacities than those of well B, but the late-crystallized pyrite suggests a recent change. In the lower-temperature, well C sample magnetite is being resorbed, and pyrite but no hematite has crystallized. This suggests a minimum sulfur fugacity of about 10^{-17} atm at 200°C (Liou et al., 1985).

Other geothermal fields do not have quite the same mineral assemblages or distributions with temperature as that depicted in Figure 11. Three examples are cited here, for comparison. The Cerro Prieto geothermal field is located in Mexico just south of the Salton Sea, and it too is developed in Colorado River sediments. The hydrothermal mineral zonation in this field has been described by Schiffman et al. (1985). The core samples that they examined span a temperature range of 200–370°C at fluid pressures less than 0.3 kb. They identified a series

of mineral isograds as follows: (1) wairakite first appears at 200°C, (2) epidote at 230°C, (3) prehnite/actinolite at 270°C, and (4) clinopyroxene (calcic augite)/biotite at 320°C. Scattered grandite (Ca-Al-Fe^{+3}) garnets appear at ≈325°C. The various calc-silicates crystallized at the expense of the carbonate cement, with epidote by far the most abundant. Schiffman et al. (1985) identified some authigenic K-feldspar but no authigenic plagioclase. These sediments contain large amounts of organic material, and Cerro Prieto is characterized by very reducing conditions, with oxygen fugacities about 4 orders of magnitude lower than those estimated from the Salton Sea assemblages.

Mineral assemblages in the Salton Sea State 2-14 well (Cho et al., 1988) are generally similar to those described by Muffler and White (1969), except for the occurrence of epidote. The State 2-14 well reached temperatures greater than 350°C, and Cho et al. (1988) defined three mineral zones with increasing depth: (1) chlorite and calcite, 610–2480 m; (2) biotite, 2480–3000 m; and (3) clinopyroxene (with calcic amphibole), 3000–3180 m. Sass et al. (1988) estimated formation temperatures to be about 250°C at 1000 m, 305°C at 1890 m, and 355°C at 3170 m. Epidote first appears at a depth slightly greater than 900 m, well within the chlorite-calcite zone, and anhydrite is found in both the chlorite-calcite and biotite zones. In contrast to Cerro Prieto, K-feldspar is a minor phase, mainly restricted to the chlorite-calcite zone, and hydrothermal plagioclase is not uncommon. At lower grades, the authigenic plagioclase is albite, whereas some oligoclase has crystallized at higher temperatures. It is possible that the current temperatures at depths greater than 900 m in State 2-14 are several tens of degrees lower than they were a few thousand years ago (Sass et al., 1988). If so, the epidote in this well may have crystallized at temperatures closer to those shown in Figure 11.

The Ohaki-Broadlands geothermal system of New Zealand is of particular interest to this study, because it is developed to a large extent in rhyolitic airfall and ash-flow tuffs. In addition, Browne and Ellis (1970) identified mineral assemblages that are generally similar to those in wells A, B, and C. The principal hydrothermal assemblage in the temperature range

230–290°C is K-mica + K-feldspar + albite + chlorite + calcite + quartz. Locally, original andesine plagioclase compositions are preserved to temperatures above 285°C. Pyrite is ubiquitous but epidote is relatively uncommon, comprising less than 1% of any sample. Epidote first appears at temperatures >260°C, and it has an Fe-rich composition similar to that of the well B epidotes. The waters from the geothermal field are nearly neutral, dilute Cl-HCO_3^- fluids with relatively high P_{CO2}. By comparison, fluids collected in the vicinity of the Unocal contract area may be slightly more dilute (lower Na, K, Cl, and SiO_2 contents), with the exception of somewhat higher sulfate contents in some analyses (Hochstein and Sudarman, 1993; Gunderson et al., 1995). The calcium contents of the fluids in both geothermal areas are very low. Compared to the Wairakei geothermal field of New Zealand, the Ohaki-Broadlands field has a smaller number of zeolites with a much more restricted distribution, as well as smaller amounts of epidote. Bicarbonate-ion concentrations in the hottest deep waters at Ohaki-Broadlands are about 10 times as high as those at Wairakei.

Many different factors may control the formation of hydrothermal mineral assemblages; according to Browne (1978) the principal factors are usually temperature, fluid composition, and permeability with a secondary group that includes pressure, rock type, and time. Any combination of these factors could control the mineral assemblages of the Sumatran cores; some possibilities are discussed here. As demonstrated by the different geothermal fields described above, epidote can crystallize at temperatures well below 300°C. Its relative scarcity in the Sumatran wells could be a function of high P_{CO2} at depth, which causes calcite to be deposited instead of epidote (Browne and Ellis, 1970; Cho et al., 1988). In this regard, it may be notable that the epidote in well B is one of the younger minerals to crystallize, whereas the calcite, at least at deeper levels, is usually one of the older vein minerals. Alternatively, some of the epidote-bearing assemblages at Cerro Prieto described by Schiffman et al. (1985) may require very low f_{O2} as well as low P_{CO2}, whereas conditions in well B are considerably more oxidizing. Browne and Ellis (1970) also calculated that for the conditions appropriate to Ohaki-Broadlands, epidote and K-mica are not compatible minerals, whereas epidote and K-feldspar

are. Fluid compositions in wells A and B, in particular the ratios (a_{Ca}/a_H) and (a_K/a_H), may vary sufficiently to stabilize epidote in well B but not in well A.

The solubility of anhydrite increases with decreasing temperature, similar to calcite (e.g., Holland, 1967), and it has a very low solubility at temperatures above 200°C. Its absence from wells A and C may thus be a reflection of fluid chemistry. For example, an increase in sulfate ion could recently have stabilized anhydrite in that well. This could be caused by an influx of sulfate-bearing fluids or a change in fluid chemistry that oxidizes some of the sulfur in the fluids. The temperature of the well C core sample would be appropriate for Ca-zeolites such as wairakite, which are common in many geothermal fields. The absence of such zeolites may be a function of high P_{CO2} (e.g., Browne and Ellis, 1970; Cho et al., 1988) or the low Ca content of the fluids (Browne and Ellis, 1970). Low calcium-ion concentrations may also be responsible for the absence of the high-temperature mineral actinolite from well A and B assemblages. Of the index minerals identified by Schiffman et al. (1985) and Cho et al. (1988), biotite is the only one that does not contain calcium. Biotite first appears at ≈320°C at Cerro Prieto, and the deepest core sample from well B, 122-3,4,5, may be very close to the biotite isograd.

Permeability has an important effect on mineral assemblage at a given depth and temperature, and the variation in mineral assemblages with permeability aids in the evaluation of production capacity of a given geothermal well (Browne, 1970). Boiling is concentrated in areas of good permeability. Adularia serves as an indicator of boiling and therefore of high permeability, because it is deposited from solution in response to the loss of CO_2 and change in pH that accompany boiling (Browne and Ellis, 1970). In contrast, very low-permeability rocks at Ohaki-Broadlands contain relict plagioclase (Browne and Ellis, 1970). Browne (1970) correlated the steam-producing capacity of a well at Ohaki-Broadlands with its feldspar mineralogy; with progressively increasing steam production the mineral sequence is (1) primary andesine, (2) albite, (3) albite + adularia, and (4) adularia. Well B would correspond to (3) or (4), well C to (2) and well A to (1). Of the three Sumatran wells, well B

is certainly associated with the largest amount of pore space. Browne and Ellis (1970) correlate the assemblage albite + K-mica at temperatures ≥200°C to recrystallization in an impermeable rock under static aquifer conditions, a situation that may easily apply to the well C tuff. In well A, the sheared bands containing relict andesine should have at least some porosity; perhaps these zones are not in communication with a fluid source.

Fractures and Microstructures

Orientation and Offset Measurements of Fractures

There is no azimuthal control on the orientation of the core samples, but closely spaced black and red lines drawn along the length of the core indicate that the samples are upright when the red line is on the right. The strikes and dips of fractures visible on a given core surface were measured relative to each other, with the red lines assigned an azimuth of 0° on the upright samples and with a plane containing the core axis being vertical. The thin sections were all cut perpendicular to the axis of the core samples, and they too were oriented relative to the red lines. The orientations and characteristics of all the measured fractures are summarized in the Appendix, and the strikes and general features of groups of fractures visible only in thin section are also included. No fracture data are available for the heavily brecciated well B sample, 29-28.

Among the most notable of these fractures and fracture zones are the heavily brecciated zones of well B core samples such as 91-13 (fracture #4 in the Appendix) and the entire 29-28 core sample. These zones resemble the high-dilation breccias that Sibson (1986) considers were formed by the implosion of wall rock into void spaces generated during rapid slip. In particular, the marked angularity of the fragments in these breccias (Fig. 8c) is consistent with the lack of frictional wear of the fragments generated by implosion (Sibson, 19986), as is the relatively large amount of open space remaining despite extensive hydrothermal cementation. Evidence for implosion brecciation is significant for geothermal exploration,

because the cavities so created would be favorable channels for fluid flow. As indicated by the occurrence of at least two stages of brecciation in 29-28, these dilational zones can exist through multiple earthquake events. According to Sibson (1986), implosion breccias preferentially occur at dilational fault jogs or releasing bends rather than the restraining-bend environment associated with well B. He notes, however, that hydraulic implosion breccias can also develop all along faults for which the effective normal stress is tensile. The latter possibility would support Hamilton's (1979) conjecture that the Barisan Mountains — where the Great Sumatran fault is situated — may currently be undergoing extension. On the other hand, the breccia zones associated with well B may all be relatively small-scale features whose occurrence reflects purely local conditions.

Several of the fractures on the core samples (e.g., #6 of 122-3,4,5) have a sheared appearance characterized by smeared-out fine-grained rock, but almost nowhere can the amount or even the direction of offset be determined. Many of the sheared fractures are likely to have slipped horizontally, mimicking the slip direction of the Great Sumatran fault, and such offsets would be difficult to identify on the core surfaces. These fractures have possible offset features indicating reverse slip. In contrast, a number of the smaller-scale fractures visible in thin section do have measurable offsets. In thin section, only the roughly horizontal component of slip can be measured. Nevertheless, despite the few examples of reverse slip noted above, the slickensides visible on fractures in shallower core samples are reported to be nearly horizontal, indicating principally strike-slip motion.

A number of labelling schemes have been put forward to describe the variety of subsidiary shears identified in natural and laboratory fault zones. These schemes differ only in the letter labels used; the actual fractures and their sense of shear are the same. The terminology of Logan et al. (1979) is adopted for this report (Fig. 12a). Some of the labelled fracture sets are more prevalent than others. The main strand of a strike-slip fault zone frequently is a Y trace that lies along one side of the fault zone. Elsewhere, a Y shear is replaced by arrays of echelon R or P traces (Fig. 12b); for example, Figure 4 of Simandjuntak and

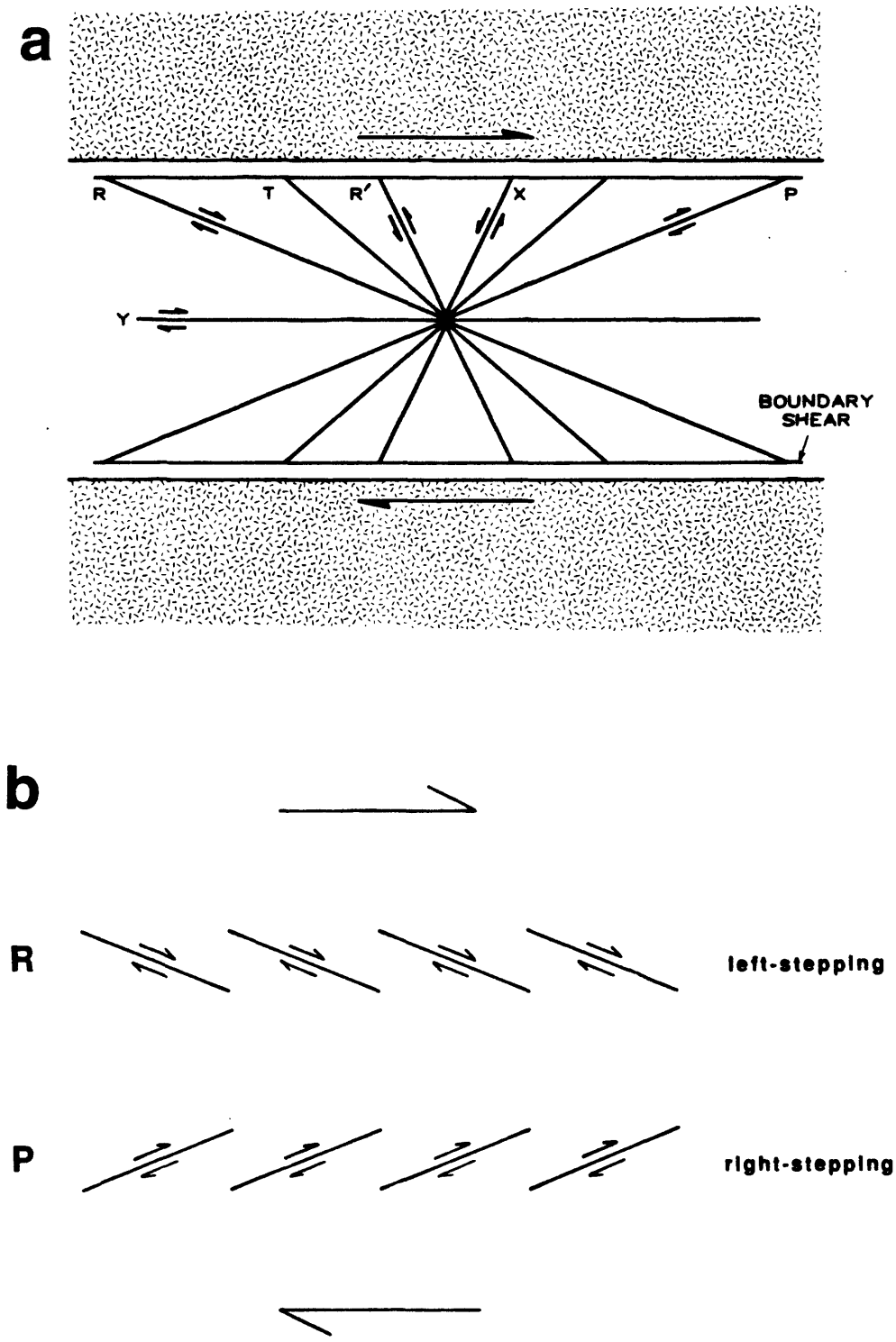

Figure 12. a) Labelling scheme and offset directions of subsidiary fracture sets developed within natural and laboratory fault zones; adapted from Logan et al. (1979). Fractures labelled T are tensile cracks that do not show offset. b) The surface exposures of many strike-slip fault zones are characterized by echelon arrays of traces. For a right-lateral fault such as the San Andreas and the Great Sumatran fault, left-stepping traces correspond to R shears and right-stepping traces to P shears.

Barber (1996) shows a group of right-stepping (P) traces along the right-lateral Great Sumatran fault in central Sumatra. The R and R' traces (Fig. 12a) are commonly equated with Coulomb shears (Hansen, 1961; Morgenstern and Tchalenko, 1967; Tchalenko, 1970). R-type traces are common at all scales in many fault zones, but Vialon (1979) and Gamond (1983) suggest that the development of R' shears is suppressed in fault zones where dilation is inhibited. Small-scale breaks corresponding to both R and R' traces were identified by Power and Tullis (1989) within the Stillwater fault zone of Nevada, which is a normal fault. The X shears are almost never found in either natural or laboratory faults; Logan et al. (1979) included them principally for symmetry. As discussed by Tchalenko (1970) and Wallace (1973), the internal features of a fault zone are scale-invariant, that is, the same geometry develops at scales varying from millimeters to kilometers. The smaller-scale traces may link together to form subsidiary shears of a higher order.

Minor offsets, generally <0.2 mm, were measured in thin section in both right-lateral and left-lateral directions along several of the fractures. Two examples of right slip are shown in Figure 13a-c. Another group of fractures whose strikes vary in a zig-zag pattern may also provide information about offset direction. The photomicrograph in Figure 13d shows one end of a calcite + chlorite + titanite-filled fracture from well A. Near the tip the fracture narrows and contains only titanite, and its strike alternates between northwestward and northeastward trends (Fig. 13d). The northeast-oriented segments are very narrow, whereas the northwest-trending ones are relatively wide, titanite-filled rhombs. Gamond (1983) has interpreted the origin of this type of structure according to the sequence in Figure 14. In laboratory experiments, subsidiary R-type traces are typically the first to form within a shear zone, and given the limited amount of offset available in triaxial friction experiments, they are generally the only shears to form (e.g., Moore et al., 1986, 1989). Where larger amounts of slip are possible, as in shear-box experiments, P-type shears develop as secondary, connecting traces. In the common case where the fault zone cannot dilate, the R traces remain the dominant segments. However, if the normal stress acting on the fault is sufficiently low that the fault can

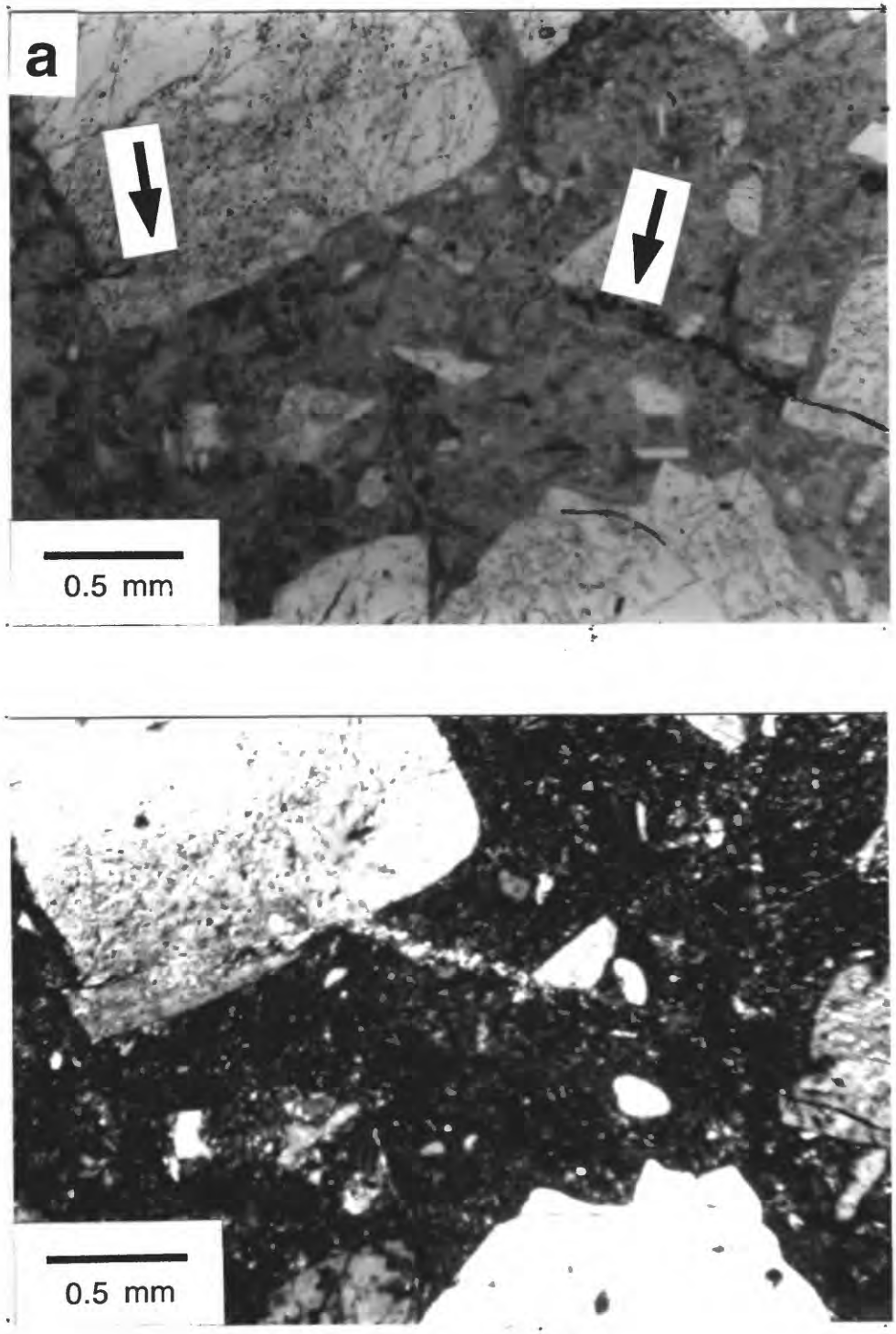

Figure 13. Narrow, bent hematite + quartz + K-mica-bearing fracture (indicated by arrows) showing right-lateral offset of plagioclase phenocrysts, viewed in a) plane-polarized light and b) crossed polarizers; 146-4, well A.

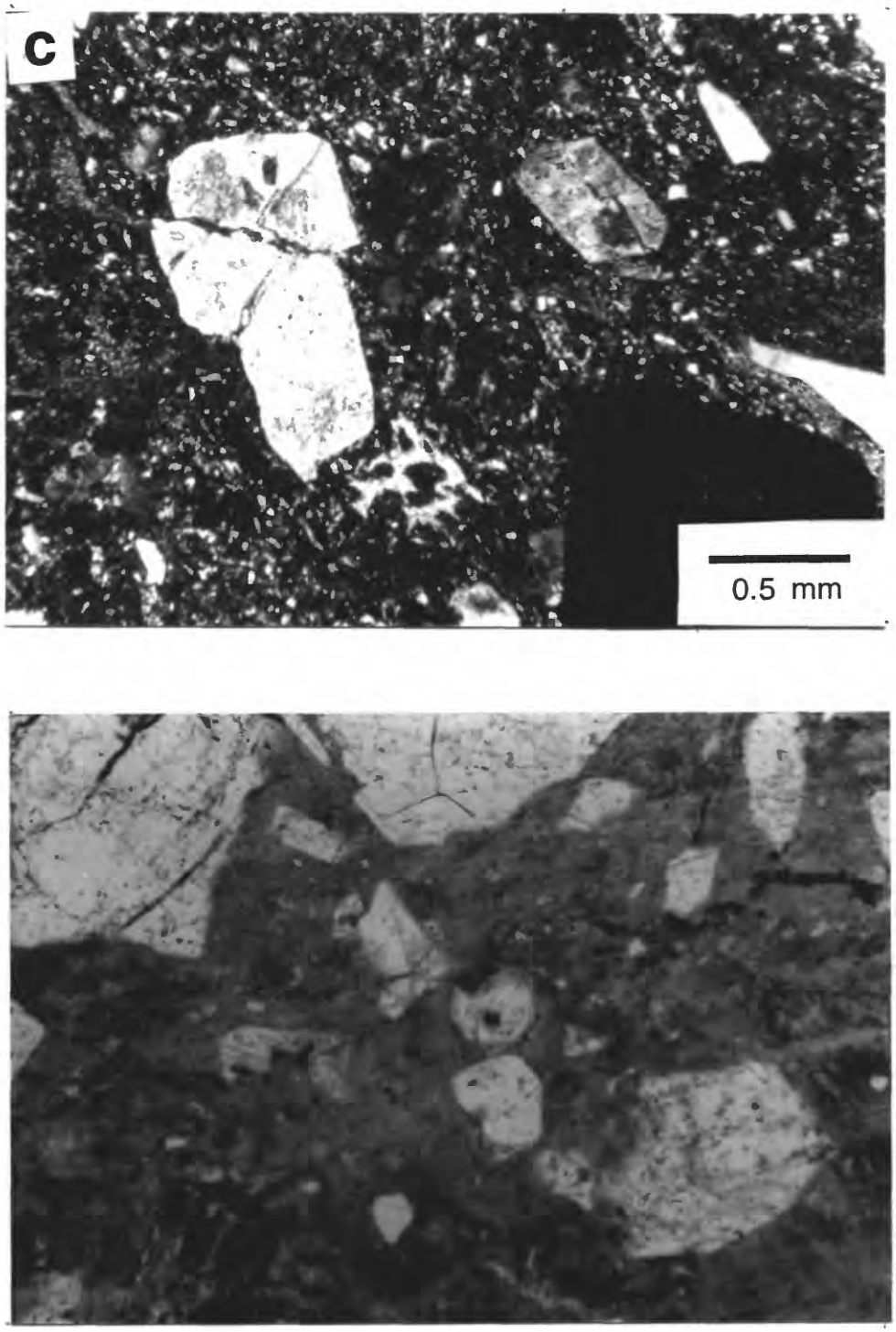

Figure 13, continued. c) Adularia + quartz-filled fracture in 29-28, well B, showing right-lateral offset of a plagioclase phenocryst; crossed polarizers. Within the plagioclase crystal, the fracture has a zig-zag arrangement of alternating narrow and wide segments. d) Zig-zag form of a titanite-bearing fracture near its termination; 146-4, well A; plane polarized light. The segments trending from upper left to lower right are variably wide, rhomb-shaped patches that are filled with titanite; the narrow connecting pieces trend from lower left to upper right.

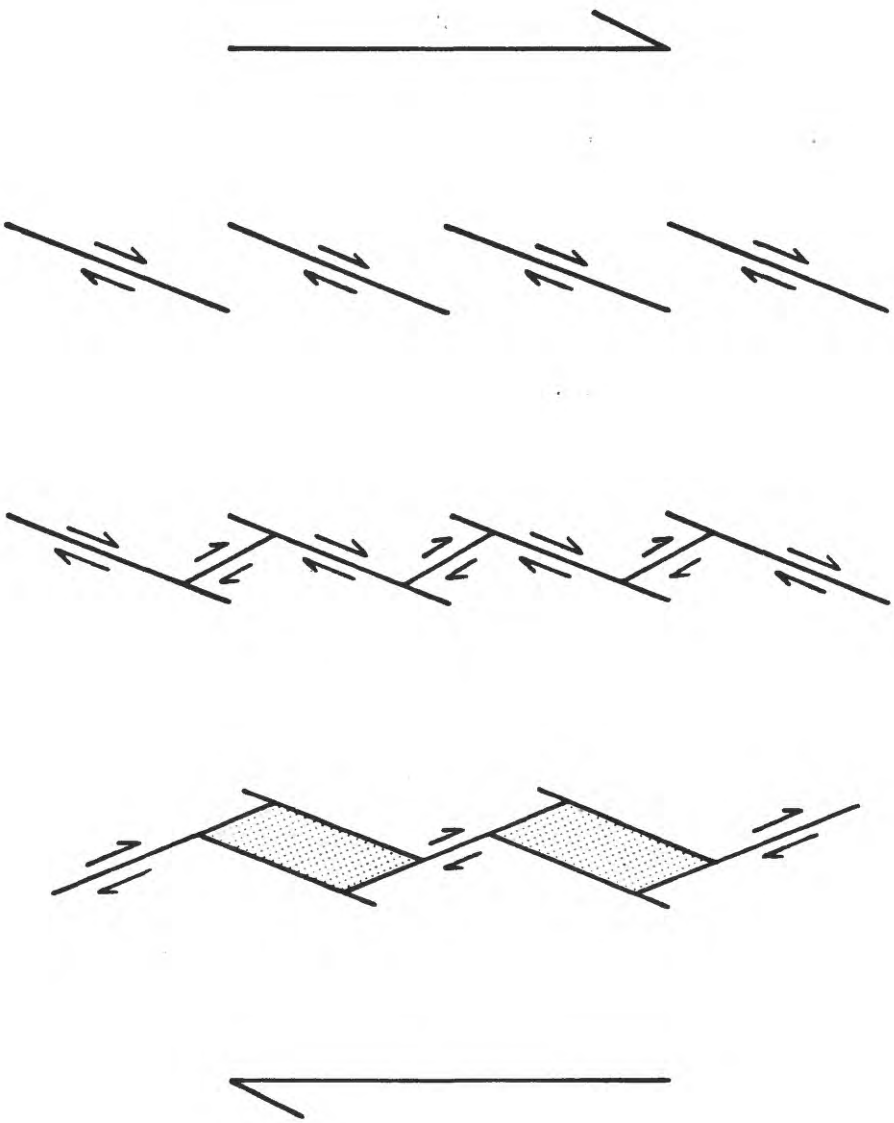

Figure 14. Sequential growth of a zig-zag shear. Primary R shears (top row) become linked by secondary P shears (second row). In the case where the fault zone can dilate, shearing eventually is concentrated along the P traces, and the R fractures open passively to form cavities.

dilate, then shear will become concentrated along the secondary P traces while the R traces are converted to passive markers that open up as a result of slip along the P traces to produce rhomb-shaped cavities (Gamond, 1983). The titanite-bearing fracture in Figure 13d is interpreted to be such a composite fracture, whose arrangement of segments indicates right-lateral offset. The inferred direction of slip of some zig-zag fractures can be verified by offset phenocrysts or lithic fragments. For example, in Figure 13c where the fracture cuts across the plagioclase phenocryst, the fracture consists of a set of segments with a roughly horizontal trend alternating with wider, northwest-striking ones. The arrangement of segments (Fig. 14) is consistent with the right-lateral offset of the phenocryst.

The practical implication of the zig-zag fractures is that the sequence of alternating narrow and wide segments can be used as an indicator of shearing direction for fractures that lack other evidence of offset (Fig. 13a-c). More significantly, their presence indicates that at least these very small-scale shears can dilate. It is possible that some of the larger fractures in well B may have a similar zig-zag configuration, but at too large a scale to be readily discerned in thin section. One possible example is fracture #4 of 85-4 (see Appendix) that is shown in Figure 3a. The photomicrograph was taken at the point where the fracture changes from a narrow, closed, sheared-looking break to an open fracture lined with adularia and traversed by anhydrite crystals. The strike of the fracture also changes at this point, and the orientations of the narrow and wide parts are consistent with right-lateral offset of the fracture. The right-stepping arrangement of major fault strands interspersed with lake-filled basins that was illustrated by Simandjuntak and Barber (1996) represents the same fault geometry at a higher order.

Stereonet Plots

The relative fracture orientations measured on the core samples (see Appendix) were plotted as great circles on stereonets, using the computer program Stereonet (version 4.5) of

R. W. Allmendinger. The stereonets are presented on the following pages with well C first, followed by well B and then well A. The various offset indicators have been added around the outside of each stereonet, at the measured strikes of the features. In the case of zig-zag fractures, the offset indicator is positioned at the average trend. Half the stereonets also include the possible orientation of the maximum (σ_1) and/or the minimum (σ_3) principal stresses. The maximum principal stress direction was determined from them ean orientation of quartz-filled tensile cracks. The minimum principal stress direction was estimated from the preferred orientation of vein minerals or from the opening direction of obliquely opened fractures.

Using the first stereonet, 49-5 from well C, as an example, a number of left offsets as well as right offsets were identified. The right offsets are clustered together and the left offsets form a second group oriented ≈20–30° clockwise from the closest right-slip marker. Of the nine core samples in which both left- and right-slip indicators have been identified, six have the pattern of 49-5, whereas the indicators overlap or are reversed in the other three. Among the other four samples, three have evidence of only right slip and the other yielded a single, left-slip trace. The relative orientations of the two groups of offset indicators in the 49-5 and similar stereonets suggest that the left-slip fractures correspond to R' traces and the right-slip ones to R, Y, or P traces (Fig. 12a). As described previously, R' fractures are likely to be as common as R traces in fault zones that can dilate (Vialon, 1979; Gamond, 1983). The apparent abundance of R' traces would therefore be consistent with the zig-zag fractures in indicating the possibility of dilation. Where available, the estimated σ_1 and σ_3 directions are consistent with the correlation described above. Notably, the three fractures showing apparent reverse slip (from 12-4, 91-13, and 173-6B) are all oriented nearly perpendicular to the estmated σ_1 direction.

Because the arrangement of right- and left-slip fractures described above corresponds to the subsidiary faulting patterns exhibited by many natural and laboratory faults (Fig. 12a), it is considered to be the valid one for the cores. The three core samples for which only one direction of offset was identified are presumed to be displaying the R' (left offset) or the R, Y, P

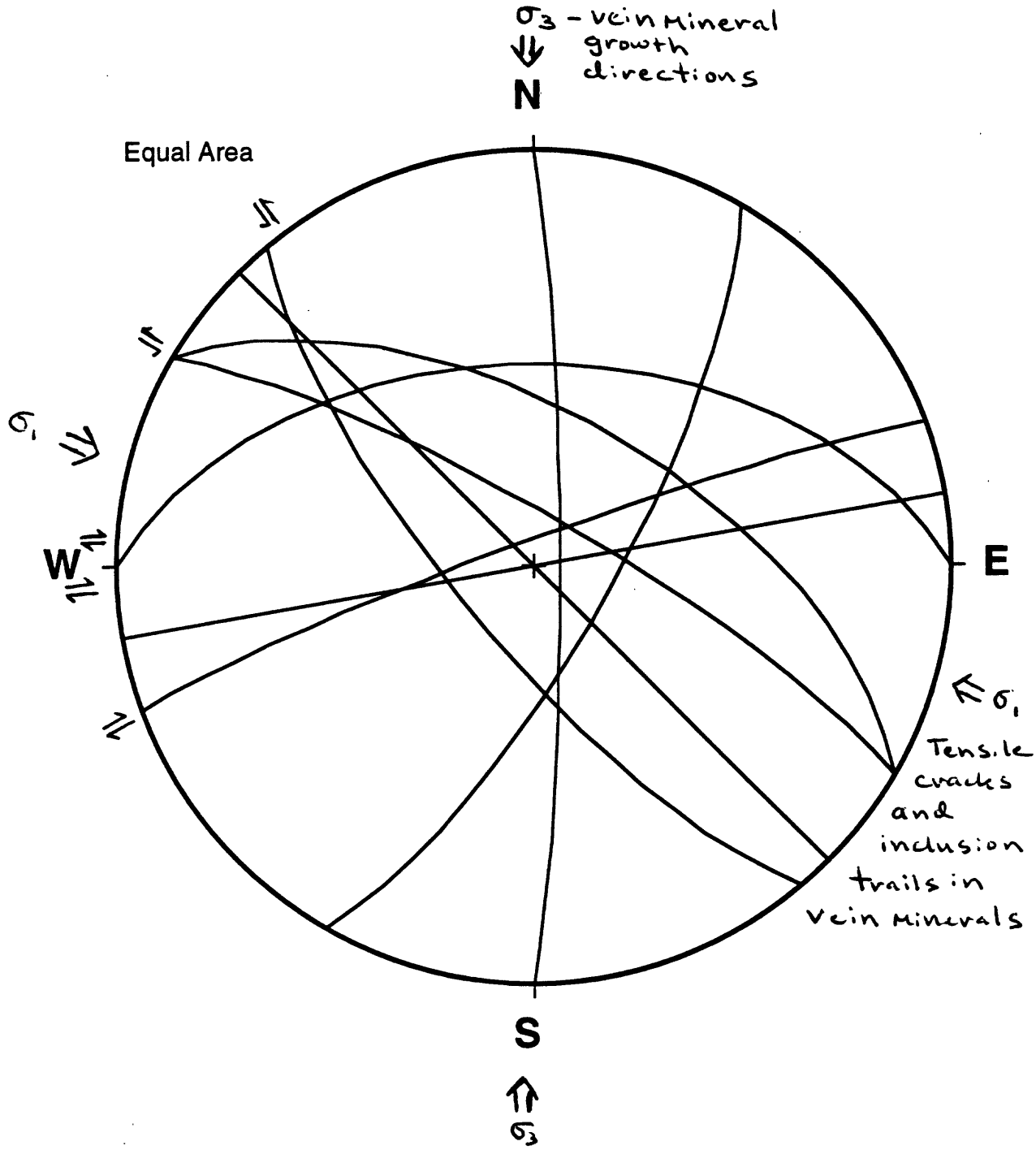
σ3 - vein Mineral growth directions
N
Equal Area
σ1
W
E
σ1
Tensile cracks and inclusion trails in vein minerals
S
σ3

49-5

Well C

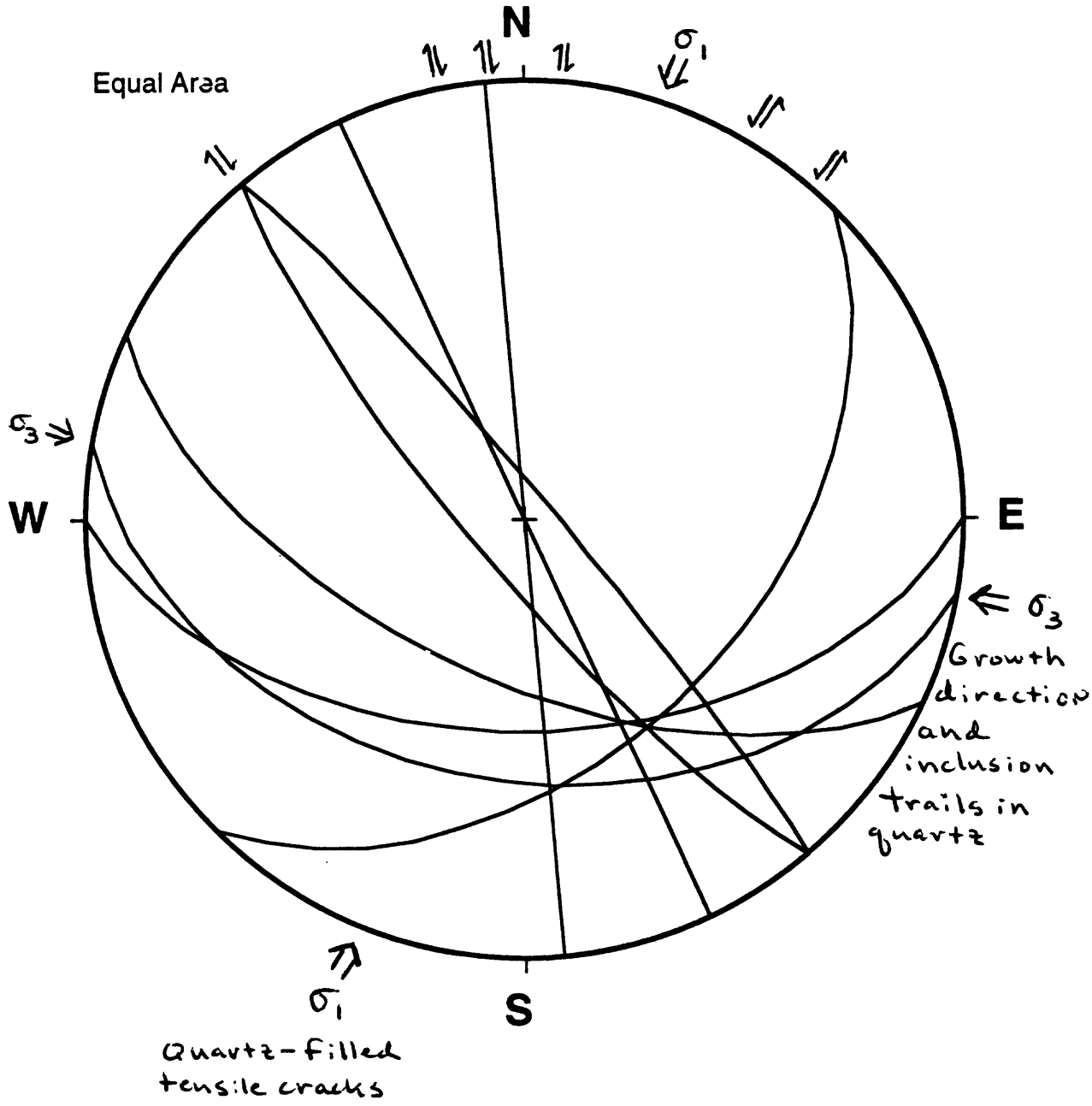
Equal Area
N
S
E
W
σ1
σ3
σ3
σ1
Growth direction and inclusion trails in quartz
Quartz-filled tensile cracks

5-19
Well B

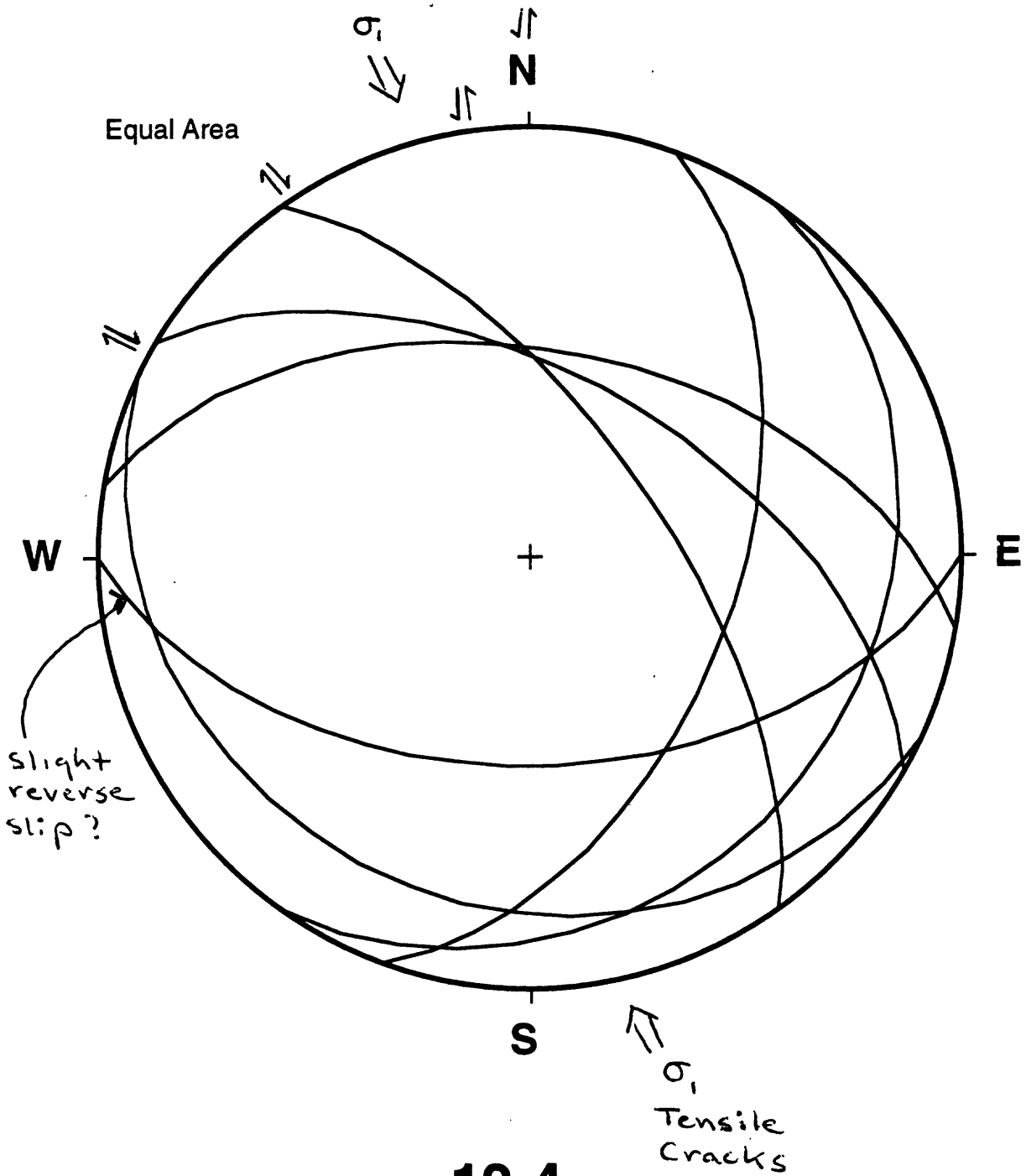

12-4
Well B

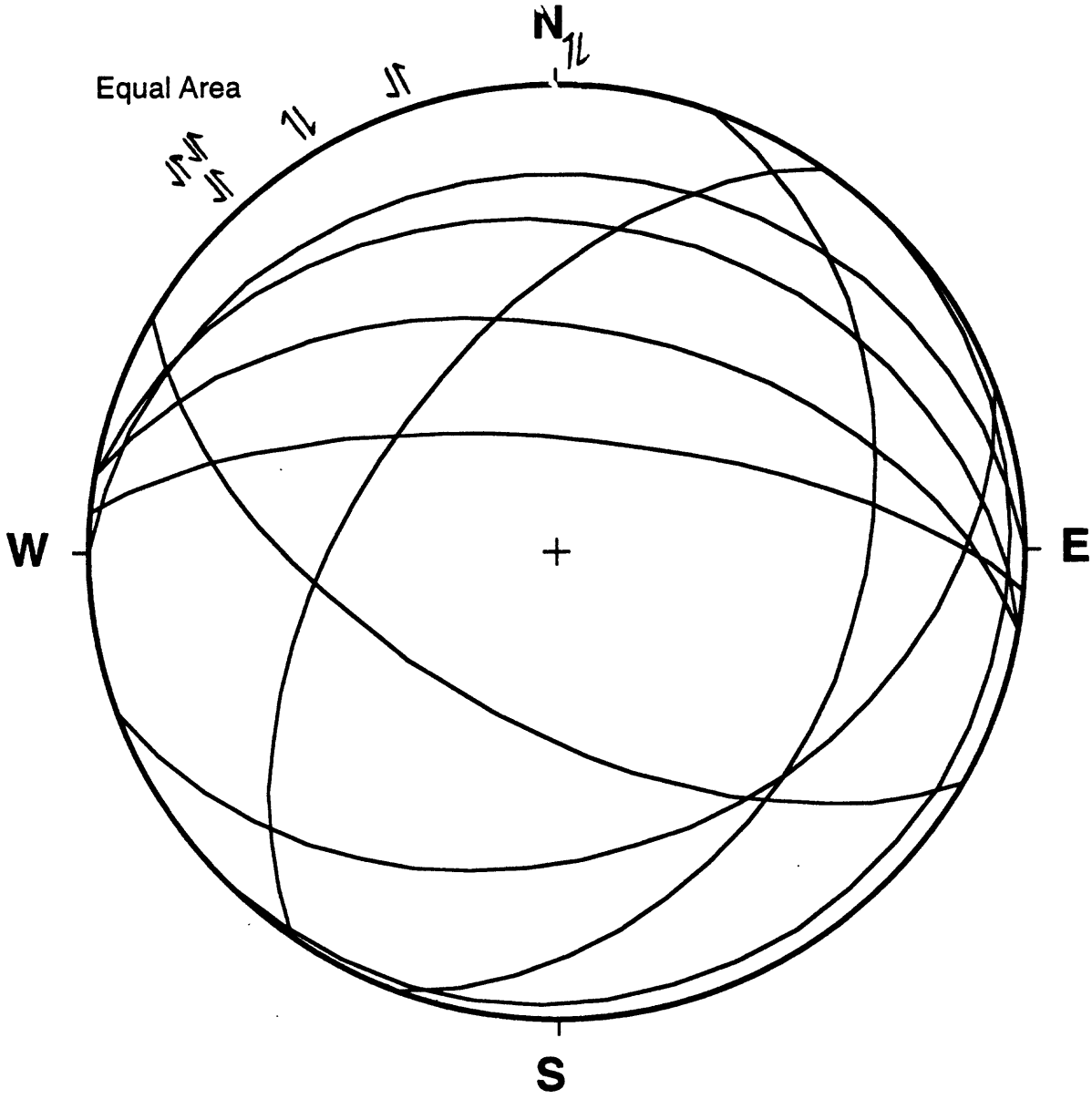

60-3
Well B

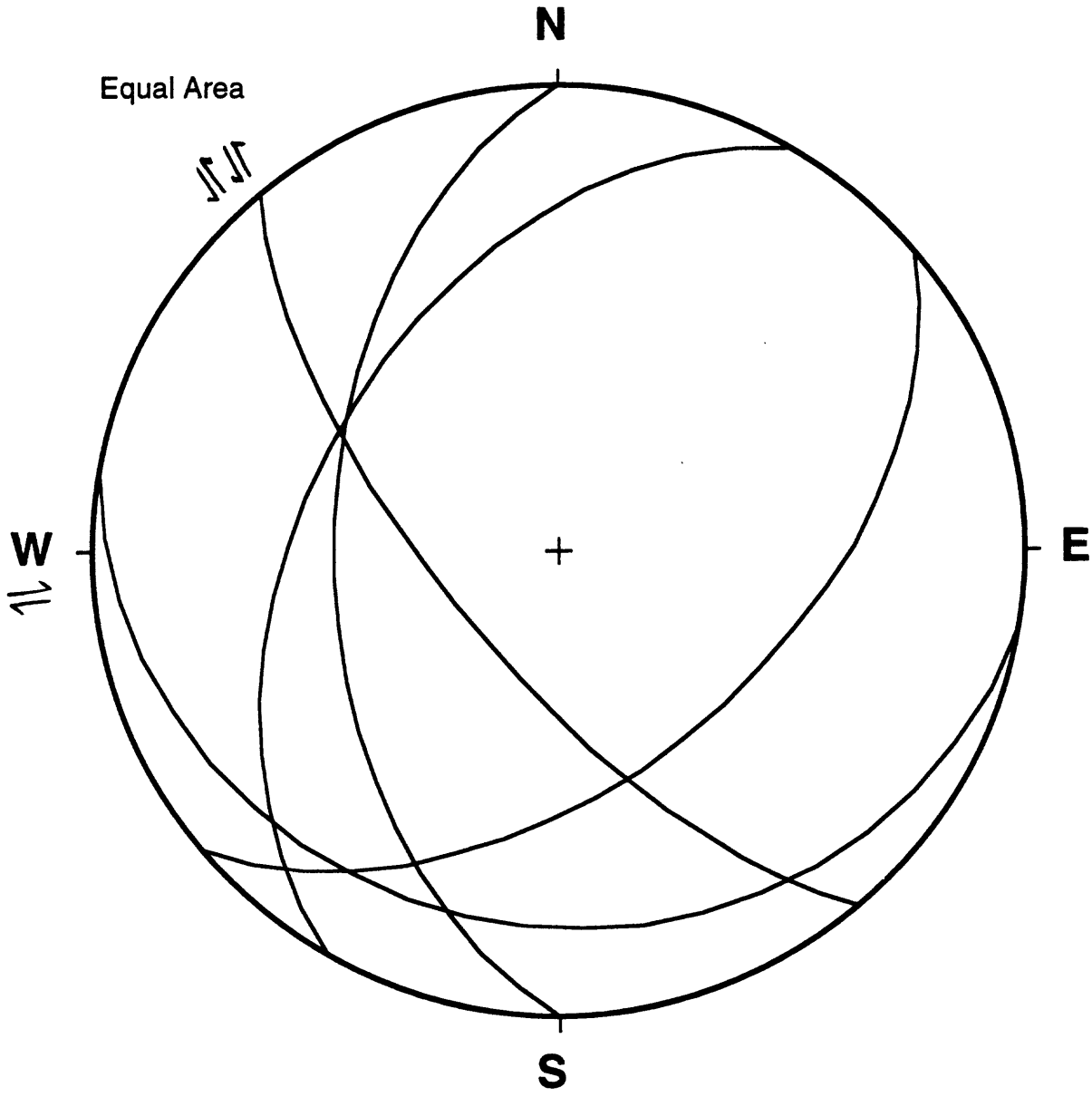

71-3
Well B

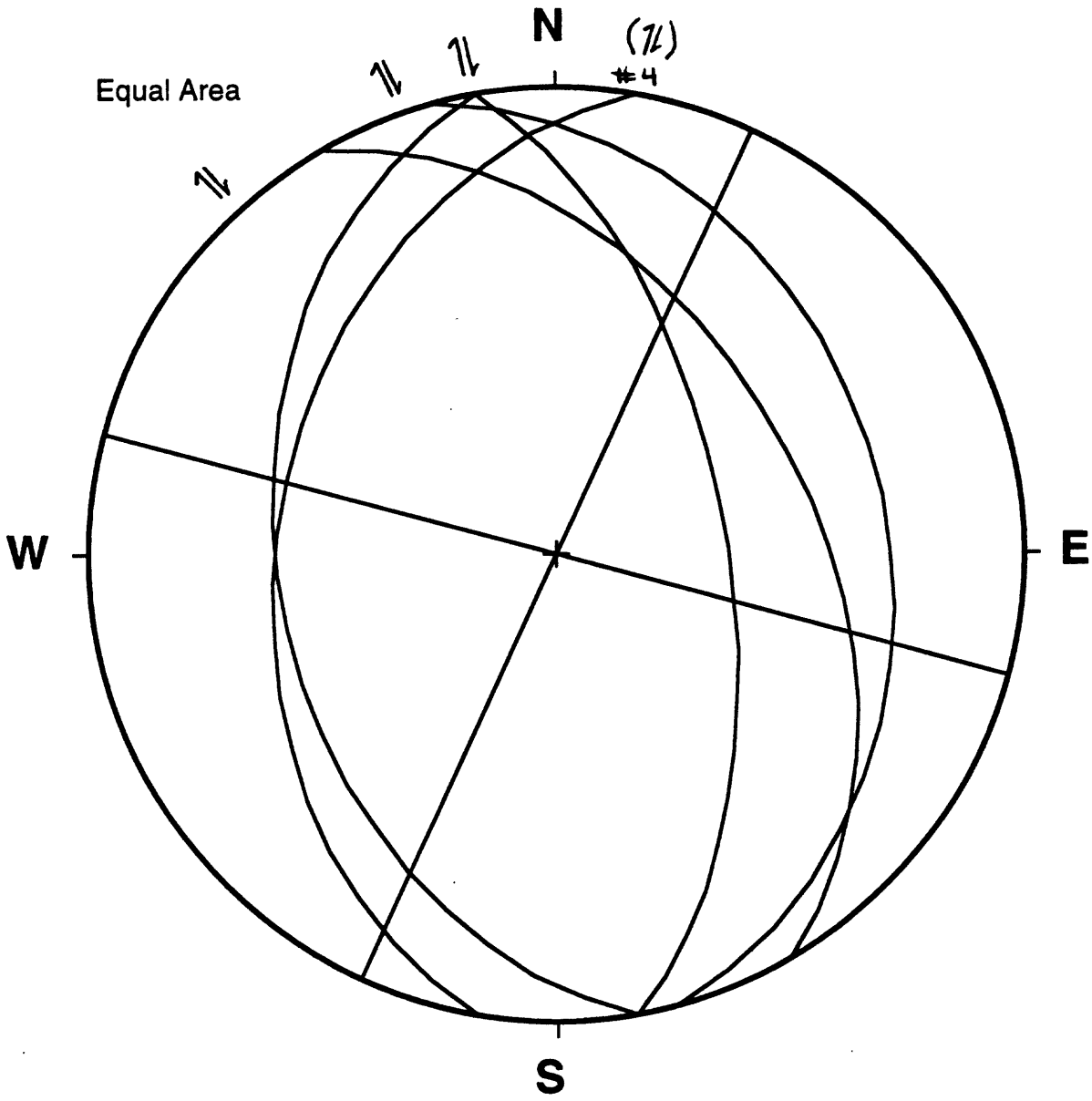

85-4,6
Well B

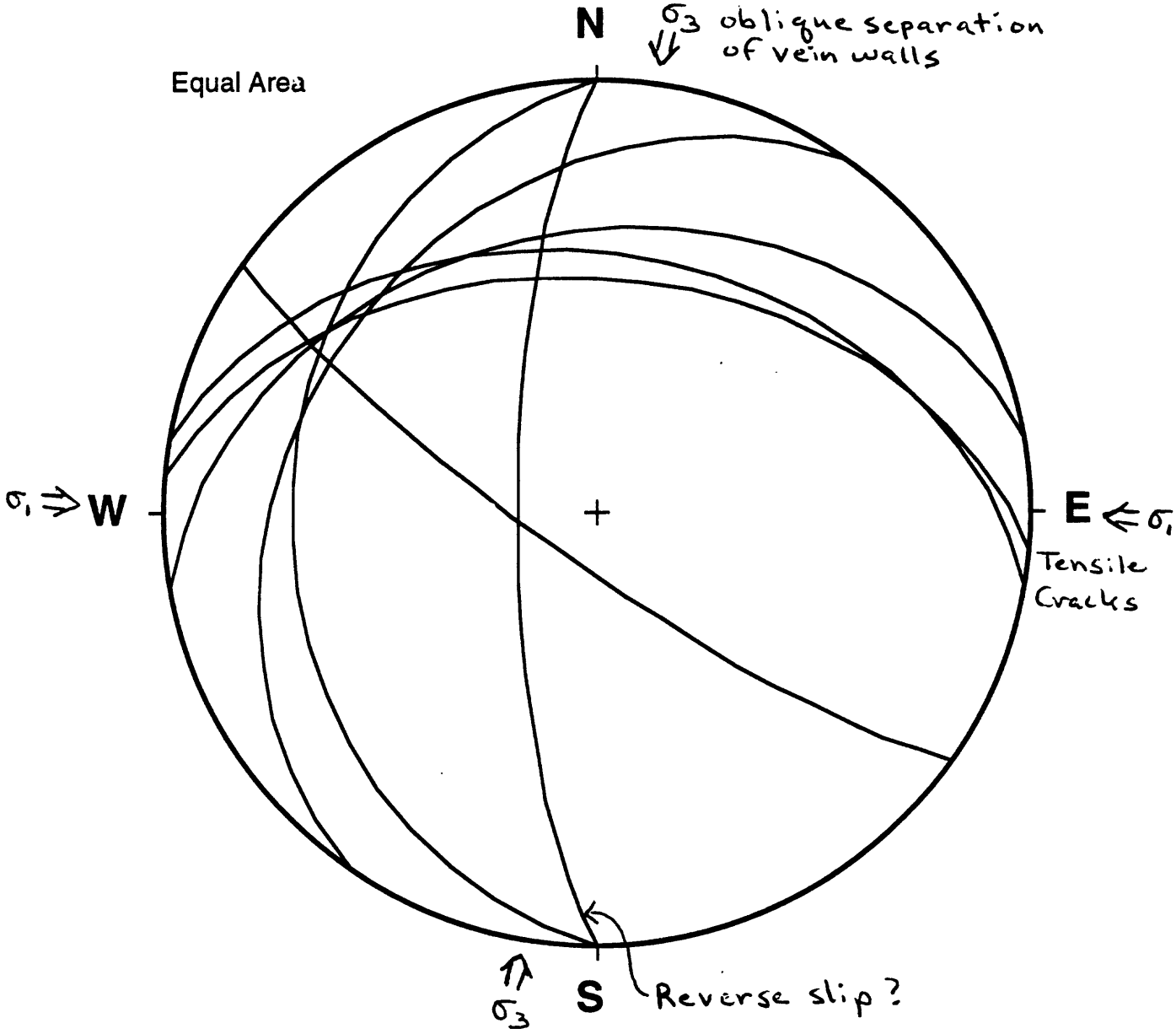
N
σ3 oblique separation of vein walls
Equal Area
σ1 ⇒ W
E ⇐ σ1
Tensile Cracks
σ3
S
Reverse slip?

91-13
Well B

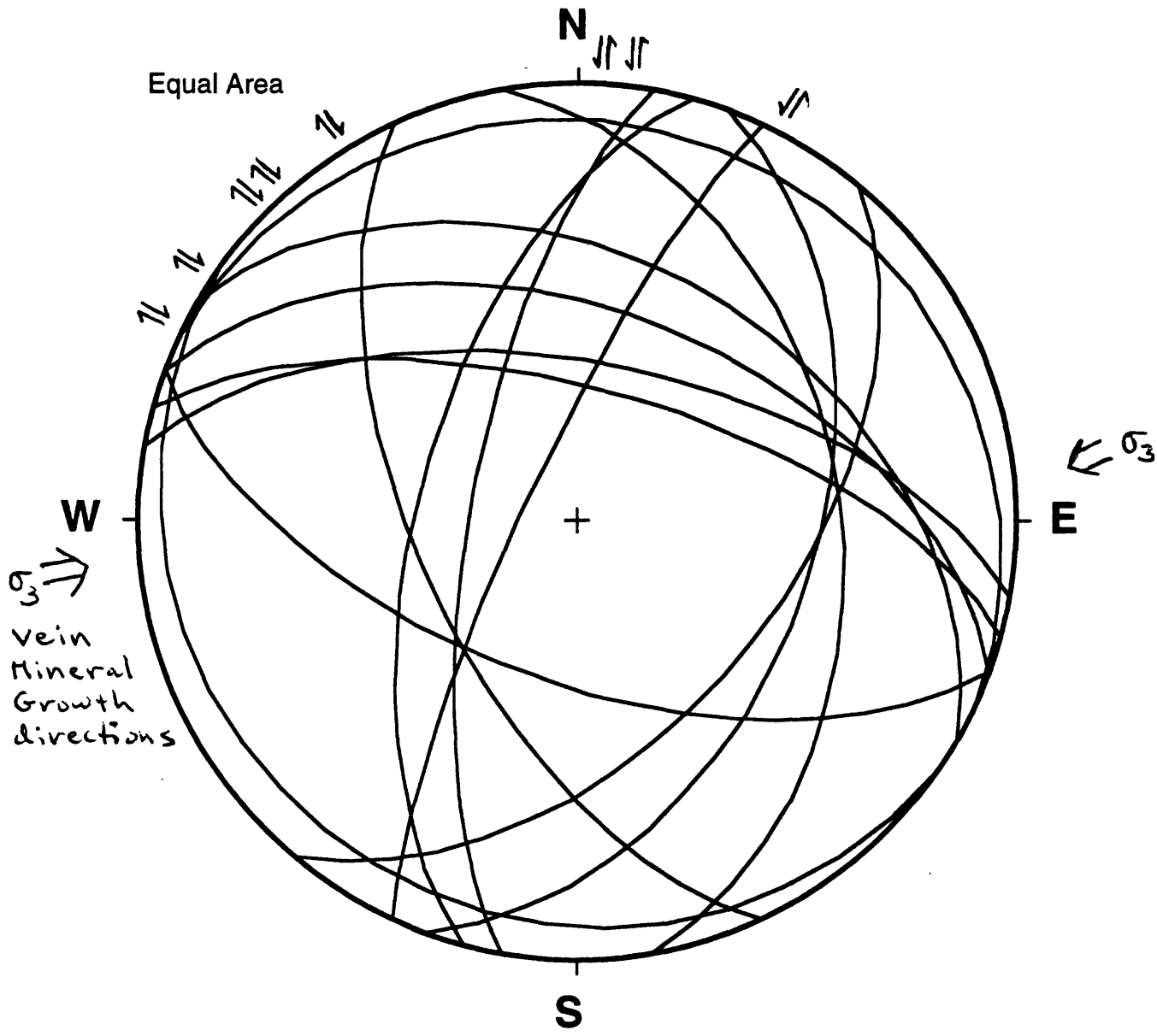

122-3,4,5
Well B

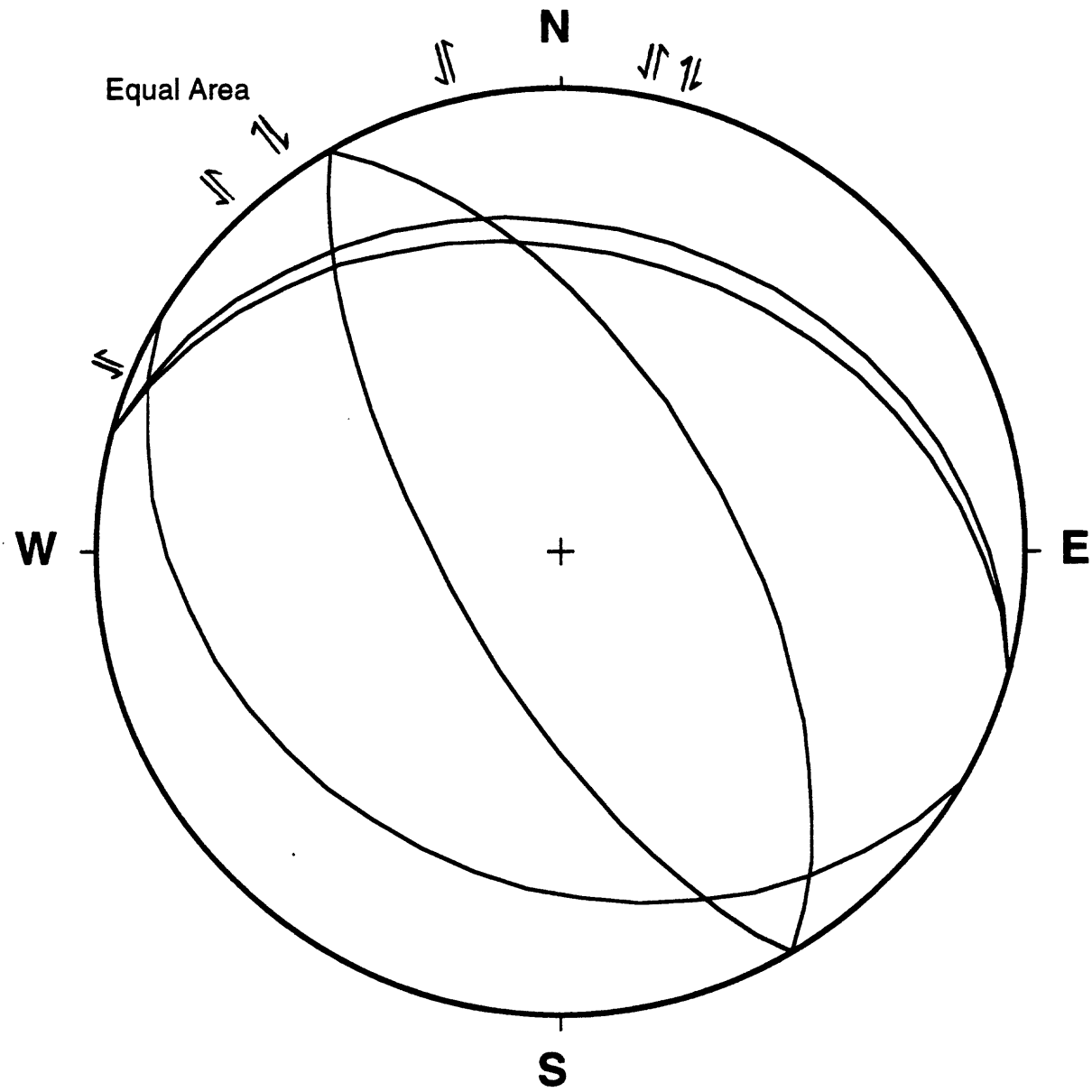

123-4B
Well A

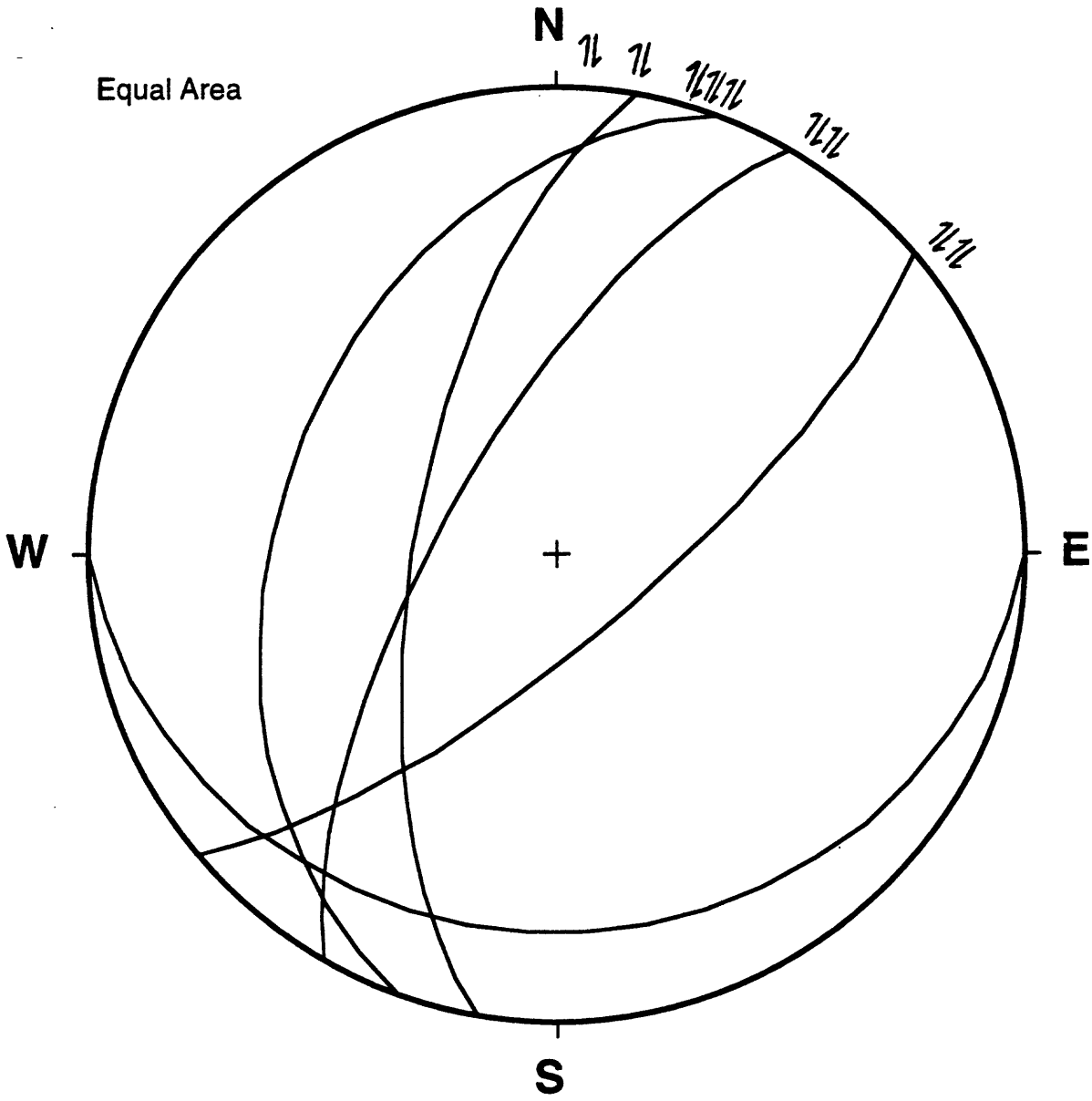

146-4
Well A

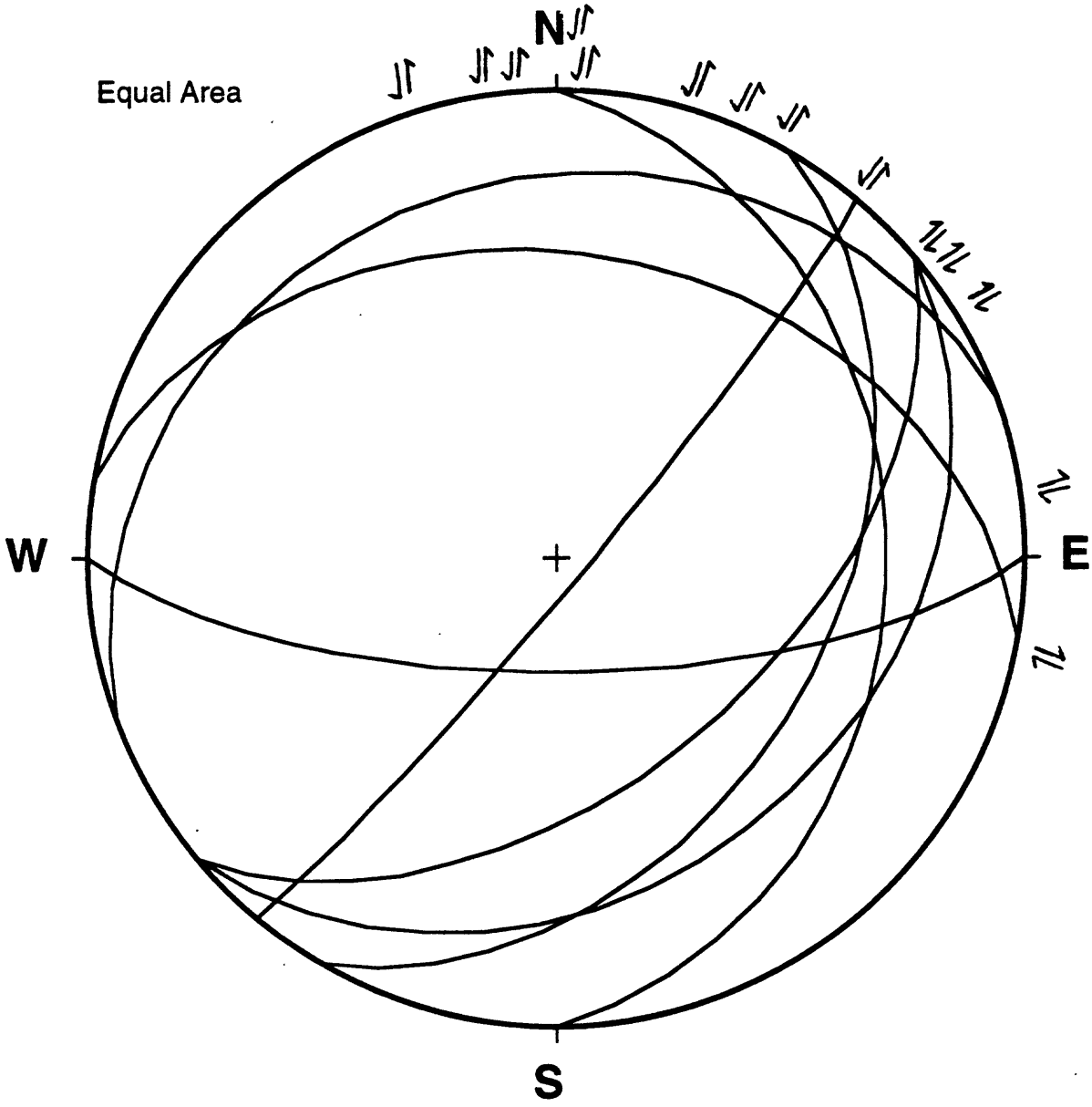

156-9
Well A

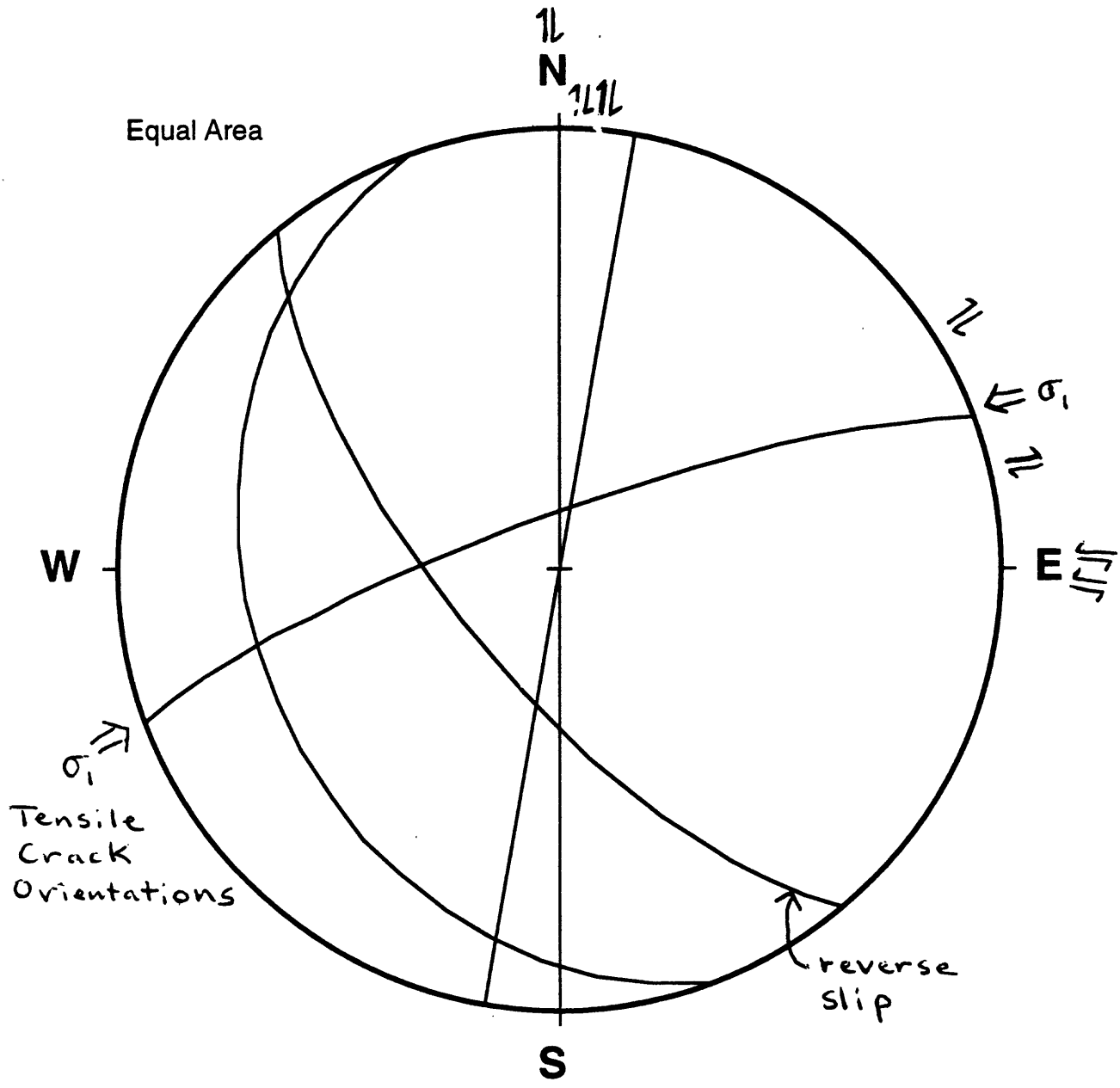
N
Equal Area
W
E
S
σ_1
σ_1
Tensile
Crack
Orientations
reverse
slip

173-6B
Well A

(right offset) group. The three samples giving contradictory results need to be re-examined. If the various discrepancies can be resolved to provide a consistent set of offset data, then the potential exists for correlating the fracture patterns of the different core samples with each other and with the Great Sumatran fault zone. The problem in making such a correlation is whether the subsidiary shears in the cores reflect the overall stress field of the fault zone or some subsidiary trace of possibly different strike or different character (e.g., a normal fault); on the other hand, all three wells were drilled close to fault strands that are subparallel to the overall strike of the fault zone. If the cores can be properly oriented, the fracture patterns will provide information about stress conditions associated with the fault zone and, of particular importance to geothermal development, they can be incorporated into models of fluid flow.

The core samples of well B are the ones located nearest to the principal strand of the Great Sumatran fault, and of the eight samples the shallowest (5-19) and the deepest (122-3,4,5) may be the closest to fault strands. Therefore, these two samples were selected for a preliminary attempt to orient the cores. Using Figure 12a as a guide, the stereonet for each core sample was rotated to match the strike of the fault zone. The arrangement of shear planes in Figure 12a looks the same when the figure is rotated 180° about a vertical axis; thus, two matches exist for each piece of core. However, it may be possible to select one in preference to the other, based on the arrangement of great circles on the stereonets. Well B has the added complication that the fracture orientations in the Appendix were determined assuming the core axis to be vertical, but the core actually dips ≈60° to the east (S84°E).

With 5-19, the orientation of the subsidiary fractures as plotted is roughly consistent with the northwest-southeast strike of the Great Sumatran fault. Thus, the first attempt at reorienting this core sample only requires the rotation to account for the dip of the well, which is accomplished by a 30° counterclockwise rotation about a horizontal axis with azimuth 0° (for these rough calculations, the dip direction was assumed to be due east). This single rotation produces the stereonet plot in Figure 15a. To create the second possibility (Fig. 15b) requires an initial rotation of 180° about a vertical axis and a second rotation about the 0°

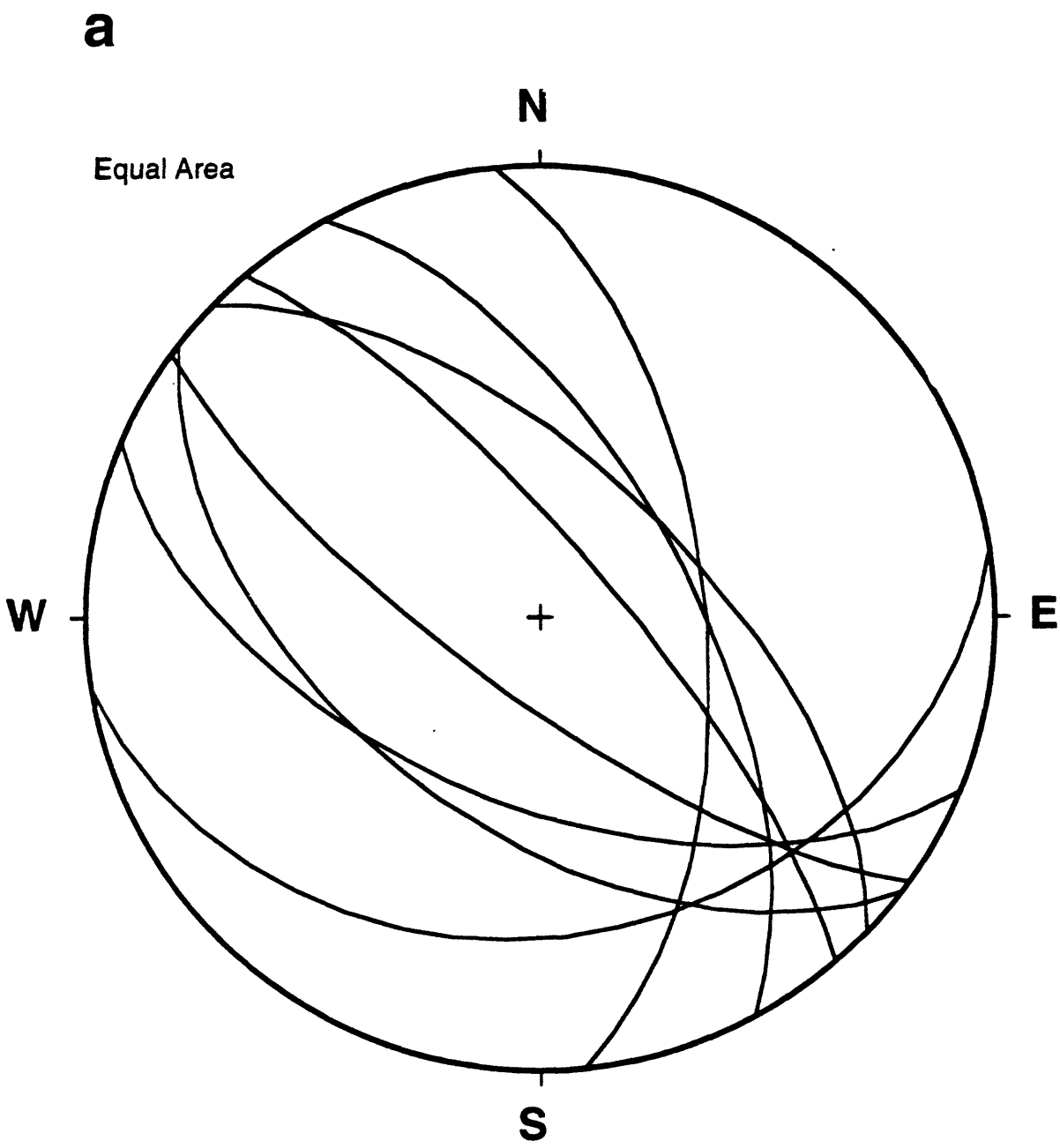

Figure 15. Rotation of 5-19 (well B) fracture data to a possibly realistic position (see text for details). a) Orientation of fractures following a single rotation of 30° counterclockwise about a horizontal axis of azimuth 0°.

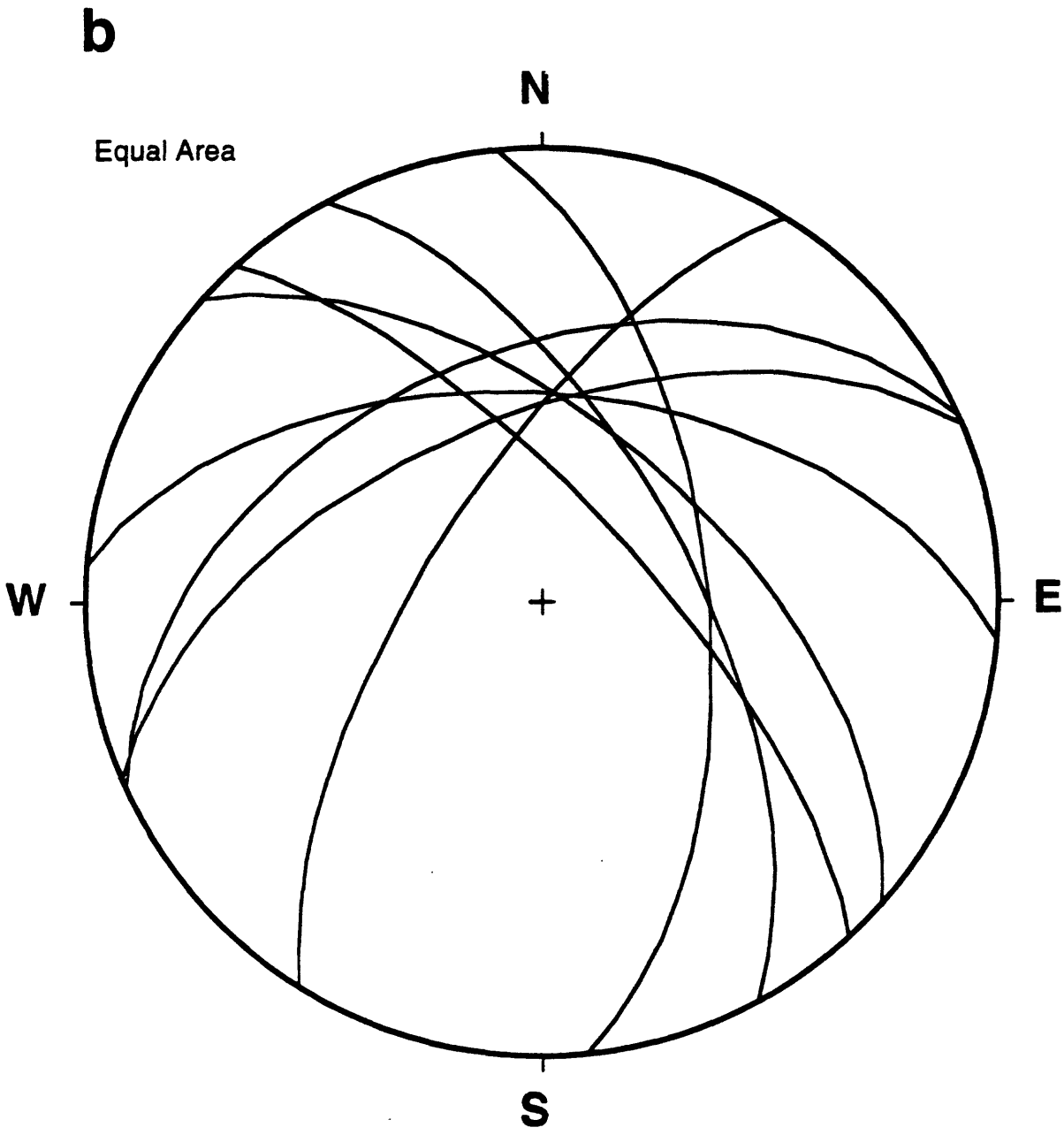

Figure 15, continued. b) Orientation of 5-19 fractures after an alternate pair of rotations: first, 180° rotation about a vertical axis, and second, 30° counterclockwise rotation about a horizontal axis of azimuth 0°.

horizontal axis, as before. The two plots have not been compared in detail, but a cursory view suggests that the stereonet of Figure 15a might be preferable, because all of the measured fractures are symmetrically distributed about the strike of the Great Sumatran fault. In contrast, the fracture orientations in Figure 15b are smeared out over a roughly 140° range.

For the test on 122-3,4,5, the stereonet was first rotated 25° clockwise about a vertical axis, to make the offset indicators consistent with the arrangement in Figure 12a. After that the same operations were performed on these data as for 5-19; the results are presented in Figure 16. This core contains so many fractures that their relative ages could be determined by cross-cutting relations; the age information is included in the figure. In this case, the second stereonet (Fig. 16b) may provide the better arrangement of fractures, because all of the younger fractures are grouped together and oriented subparallel to the strike of the fault. With a couple of exceptions, the older and the intermediate-age fractures in Figure 16b are also grouped by strike, and there is a progressive change in strike from the oldest, through the intermediate-age, to the youngest fractures. On the other hand, only one intermediate-age fracture is subparallel to the strike of the Great Sumatran fault in the first stereonet; all of the other fractures are randomly distributed. Figure 16b indicates another potential benefit of correctly oriented cores, in that the fracture sequence, where determinable, may be useful in elucidating the history of faulting in the area.

Conclusions

- Hydrothermal mineral assemblages are distinctive from well to well. These variations may be primarily a function of temperature, but fluid chemistry and permeability also play important roles. The core samples from wells A and B show some variations in mineralogy with depth and with time, indicating the possibility of changing temperature and/or fluid compositions.

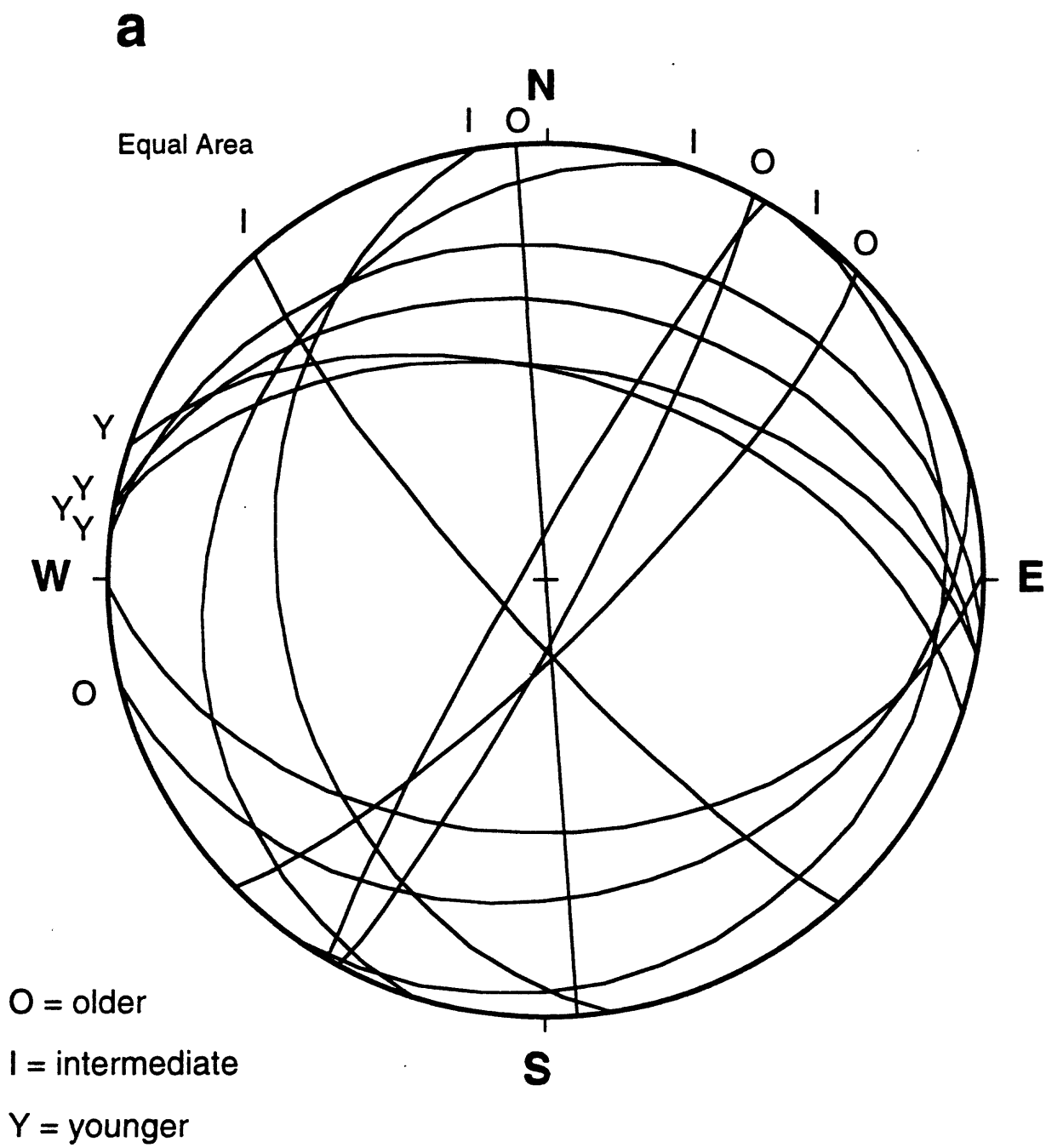

Figure 16. Rotation of 122-3,4,5 (well B) fracture data to a potentially realistic position (see text for details). O, I, and Y are the relative ages of the fractures determined from cross-cutting relationships. a) Orientation of fractures following a pair of rotations: first, 25° clockwise rotation about a vertical axis; second, 30° counterclockwise rotation about a horizontal axis of azimuth 0°.

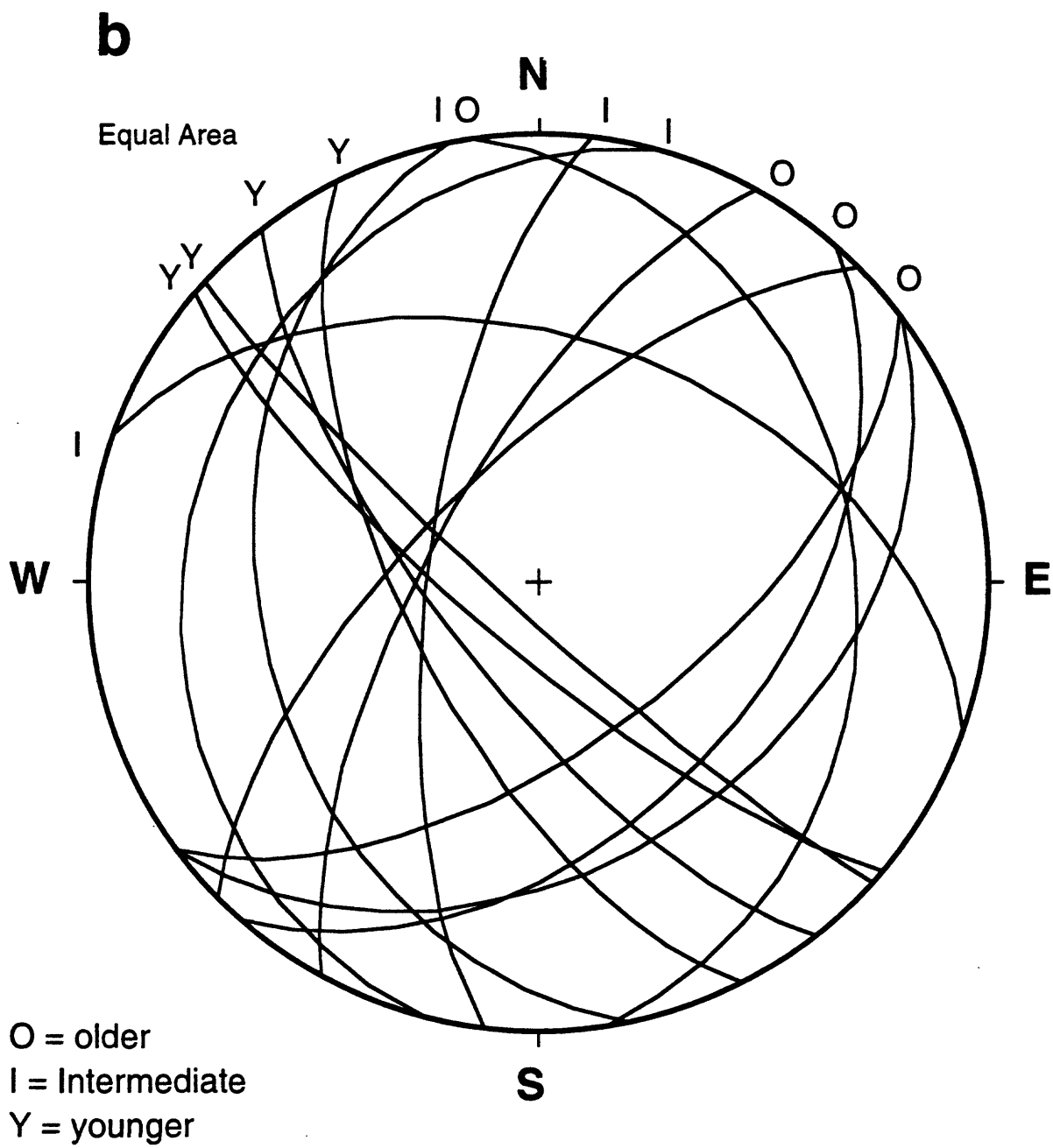

122-3,4,5 Second Rotation

Figure 16, continued. b) 122-3,4,5 fracture orientations resulting from an alternate set of rotations: first, 205° clockwise rotation about a vertical axis, and second, 30° counterclockwise rotation about a horizontal axis of azimuth 0°.

- The application of the chlorite geothermometer of Cathelineau (1988) to the chlorite compositions obtained from wells A and B yield temperature ranges that are consistent with the fluid temperatures measured at the corresponding depth intervals.

- The hydrothermal alteration in the Silangkitang geothermal field is similar in many respects to the alteration patterns of the Salton Sea geothermal field, U. S. A. and Ohaki-Broadlands, New Zealand.

- Differences in feldspar mineralogy among the three wells are consistent with well A being the least permeable and well B the most permeable. The many wide, open fractures and numerous cavities in the well B core also attests to its high permeability.

- The zig-zag arrangement of some subsidiary shears, the relative abundance of left-lateral (R') fractures, and the occurrence of implosion breccias in the core samples situated close to a restraining bend of the principal fault strand, all support the possibility that this portion of the fault zone can dilate.

- The correlation of right- and left-slip indicators in the core samples with the subsidiary fractures of known orientation that are commonly developed in fault zones suggests that they may potentially be used to determine the true orientation of each core sample. This would open the way for modeling fluid flow in the geothermal prospect area and for investigating stress relations at depth in and around the fault zone.

Acknowledgments

Special thanks to Unocal Geothermal for allowing us to examine some of their core materials and for permission to publish the results of the investigations. Steve Hickman and David Lockner of the U. S. Geological Survey worked out the research proposal with Unocal.

References

Bellier, O., Sebrier, M., and Pramunijoyo, S., 1991, La grande faille de Sumatra: géométrie, cinématique et quantité de déplacement mises en évidence par l'imagerie satellitaire, Comptes Rendus de l'Académie des Sciences de Paris, 312: 1219–1226.

Bevins, R. E., Robinson, D., and Rowbotham, G., 1991, Compositional variations in mafic phyllosilicates from regional low-grade metabasites and application of the chlorite geothermometer, Journal of Metamorphic Geology, 9: 711–721.

Bird, D. K., Cho, M., Janik, C. J., Liou, J. G., and Caruso, L. J., 1988, Compositional, order/disorder, and stable isotope characteristics of Al-Fe epidote, State 2-14 drill hole, Salton Sea geothermal system, Journal of Geophysical Research, 93: 13,135–13,144.

Browne, P. R. L., 1970, Hydrothermal alteration as an aid in investigating geothermal fields, Geothermics, Special Issue, 2: 564–570.

Browne, P. R. L., 1978, Hydrothermal alteration in active geothermal fields, Annual Review of Earth and Planetary Science, 6: 229–250.

Browne, P. R. L., and Ellis, A. J., 1970, The Ohaki-Broadlands hydrothermal area, New Zealand: Mineralogy and related geochemistry, American Journal of Science, 269: 97–131.

Cathelineau, M., 1988, Cation site occupancy in chlorites and illites as a function of temperature, Clay Minerals, 23: 471–485.

Cathelineau, M., and Nieva, D., 1985, A chlorite solid solution geothermometer the Los Azufres (Mexico) geothermal system, Contributions to Mineralogy and Petrology, 91: 235–244.

Cho, M., Liou, J. G., and Bird, D. K., 1988, Prograde phase relations in the State 2-14 well metasandstones, Salton Sea geothermal field, California, Journal of Geophysical Research, 93: 13,081–13,103.

Coombs, D. S., Nakamura, Y., and Vuagnat, M., 1976, Pumpellyite-actinolite facies schists of the Taveyanne Formation near Loèche, Valais, Switzerland, Journal of Petrology, 17: 440–471.

Deer, W. A., Howie, R. A., and Zussman, J., 1962, Rock-Forming Minerals, Volume 3, Sheet Silicates, John Wiley, New York, pp. 213-225.

Deer, W. A., Howie, R. A., and Zussman, J., 1966, An Introduction to the Rock-Forming Minerals, John Wiley, New York, pp. 420–421.

Deer, W. A., Howie, R. A., and Zussman, J., 1986, Rock-Forming Minerals, Second Edition, Volume 1B, Disilicates and Ring Silicates, John Wiley, New York, pp. 2–179.

Exley, R. A., 1980, Microprobe studies of REE-rich accessory minerals: Implications for Skye granite petrogenesis and REE mobility in hydrothermal systems, Earth and Planetary Science Letters, 48: 97–110.

Fitch, T. J., 1972, Plate convergence, transcurrent faults and internal deformation adjacent to southeast Asia and the western Pacific, Journal of Geophysical Research, 77: 4432–4460.

Gamond, J. F., 1983, Displacement features associated with fault zones: a comparison between observed examples and experimental models, Journal of Structural Geology, 5: 33–45.

Gunderson, R. P., Dobson, P. F., Sharp, W. D., Pudjianto, R., and Hasibuan, A., 1995, Geology and thermal features of the Sarulla contract area, north Sumatra, Indonesia, Proceedings World Geothermal Congress, 2: 687–692.

Hamilton, W., 1979, Tectonics of the Indonesian Region, U. S. Geological Survey Professional Paper, 1078, pp. 18–38.

Hansen, B., 1961, Shear box tests on sand, Proceedings 5th International Conference on Soil Mechanics, 1: 127–131.

Higgins, J. B., and Ribbe, P. H., 1976, The crystal chemistry and space group of natural and synthetic titanites, American Mineralogist, 61: 878–888.

Hochstein, M. P., and Sudarman, S., 1993, Geothermal resources of Sumatra, Geothermics, 22: 181–200.

Holland, H. D., 1967, Gangue minerals in hydrothermal deposits, in Barnes, H. L., ed., Geochemistry of Hydrothermal Ore Deposits, H. H. Rinehart and Winston, Inc., New York, pp. 382–436.

Hughes, J. M., Bloodaxe, E. S., Hanchar, J. M., and Foord, E. E., 1997, Incorporation of rare earth elements in titanite: Stabilization of the *A2/a* dimorph by creation of antiphase boundaries, American Mineralogist, 82: 512–516.

Kawachi, Y., Grapes, R. H., Coombs, D. S., and Dowse, M., 1983, Mineralogy and petrology of a piemontite-bearing schist, western Otago, New Zealand, Journal of Metamorphic Geology, 1: 353–372.

Keith, T. E. C., Muffler, L. J. P., and Cremer, M., 1968, Hydrothermal epidote formed in the Salton Sea geothermal system, California, American Mineralogist, 53: 1635–1644.

Kranidiotis, P., and MacLean, W. H., 1987, Systematics of chlorite alteration at the Phelps Dodge massive sulfide deposit, Matagami, Quebec, Economic Geology, 82: 1898–1911.

Liou, J. G., Seki, Y., Guillemette, R. N., and Sakai, H., 1985, Compositions and parageneses of secondary minerals in the Onikobe geothermal system, Japan, Chemical Geology, 49: 1–20.

Logan, J. M., Friedman, M., Higgs, N., Dengo, C., and Shimamoto, T., 1979, Experimental studies of simulated gouge and their application to studies of natural fault zones, Proceedings of Conference VIII Analysis of Actual Fault Zones in Bedrock, U. S. Geological Survey Open-File Report, 79-1239: 305–343.

McCourt, W. J., Crow, M. J., Cobbing, E. J., and Amin, T. C., 1996, Mesozoic and Cenozoic plutonic evolution of SE Asia: evidence from Sumatra, Indonesia, in Hall, R., and Blundell, D., eds., Tectonic Evolution of Southeast Asia, Geological Society Special Publication, 106: 321–335.

Moore, D. E., Summers, R., and Byerlee, J. D., 1986, The effect of sliding velocity on the frictional and physical properties of heated fault gouge, Pure and Applied Geophysics, 124: 31–52.

Moore, D. E., Summers, R., and Byerlee, J. D., 1989, Sliding behavior and deformation textures of heated illite gouge, Journal of Structural Geology, 11: 329–342.

Morgenstern, M. R., and Tchalenko, J. S., 1967, Microscopic structures in kaolin subjected to direct shear, Géotechnique, 17: 309–328.

Mount, V. S., and Suppe, J., 1992, Present-day stress orientations adjacent to active strike-slip faults: California and Sumatra, Journal of Geophysical Research, 97: 11,995–12,013.

Muffler, L. J. P., and White, D. E., 1969, Active metamorphism of Upper Cenozoic sediments in the Salton Sea geothermal field and the Salton trough, southeastern California, Geological Society of America Bulletin, 80: 157–182.

Power, W. L., and Tullis, T. E., 1989, The relationship between slickenside surfaces in fine-grained quartz and the seismic cycle, Journal of Structural Geology, 11: 879–893.

Sass, J. H., Priest, S. S., Duda, L. E., Carson, C. C., Hendricks, J. D., and Robison, L. C., 1988, Thermal regime of the State 2-14 well, Salton Sea Scientific Drilling Project, Journal of Geophysical Research, 93: 12,995–13,004.

Schiffman, P., Bird, D. K., and Elders, W. A., 1985, Hydrothermal mineralogy of calcareous sandstones from the Colorado River delta in the Cerro Prieto geothermal system, Baja California, Mexico, Mineralogical Magazine, 49: 435–449.

Sibson, R. H., 1986, Brecciation processes in fault zones: Inferences from earthquake rupturing, Pure and Applied Geophysics, 124: 159–175.

Sieh, K., Zachariasen, J., Bock, Y., Edwards, L., Taylor, F., and Gans, P., 1994, Active tectonics of Sumatra, Geological Society of America Abstracts with Programs, 26(7): A382.

Simandjuntak, T. O., and Barber, A. J., 1996, Contrasting tectonic styles in the Neogene orogenic belts of Indonesia, in Hall, R., and Blundell, D., eds., Tectonic Evolution of Southeast Asia, Geological Society Special Publication, 106: 185–201.

Tchalenko, J. S., 1970, Similarities between shear zones of different magnitudes, Geological Society of America Bulletin, 81: 1625–1640.

Tikoff, B., and Teyssier, C., 1994, Strain modeling of displacement-field partitioning in transpressional orogens, Journal of Structural Geology, 16: 1575–1588.

Vialon, P., 1979, Les déformations continues–discontinues des roches anisotropes, Eclogae Geologiae Helveticae, 72: 531–549.

Wallace, R. E., 1973, Surface fracture patterns along the San Andreas fault, in Kovach, R. L., and Nur, A., eds., Proceedings of the Conference on Tectonic Problems of the San Andreas Fault System, Stanford University Publications in Geological Science, 13: 248–250.

Xie, X., Byerly, G. R., and Farrell, R. E., Jr., 1997, IIb trioctahedral chlorite from the Barberton greenstone belt: crystal structure and rock composition constraints with implications to geothermometry, Contributions to Mineralogy and Petrology, 126: 275–291.

Yau, Y. C., 1986, Microscopic studies of hydrothermally metamorphosed shales from the Salton Sea geothermal field, California, USA, Ph. D. thesis, University of Michigan, Ann Arbor, 159 pp.

Appendix. Relative Fracture Orientations and Characteristics

Because the orientations of the core samples are not known, all fractures and thin sections were measured relative to the red line drawn on the core surface (see text). It should be kept in mind that, although internally consistent, the reported strikes and dip directions for a given core sample are probably not their true orientations, and they cannot be directly compared to other samples. In addition, well A was drilled at an angle of 87.5° from horizontal, well C at 80°, and well B at approximately 60° (a range of 57° to 64° dip for the sampled interval). The numbering system of the fractures reflects the initial list of measurements for each core sample.

123-4B (Well A)

In contrast to other core samples from well A, this piece has only two distinct fractures:

	Relative Strike	Relative Dip Direction	Amount of Dip	
# 2	120°/300°	210°	30°	Irregular fracture surface with small, unfilled patches. Although very hard to find in thin section (123-4Bb), it may correspond to a faint band of ground-up rock with a scattering of K-mica.
# 4	150°/330°	240°	≈70°	≤0.5 mm wide; fracture marked by smeared-out green minerals. In thin section (123-4Bb), it is a narrow, sheared-looking band with disseminated opaque grains (Fe-oxides?). It is best seen in plane polarized light, where it appears as a relatively light-colored, fine-grained band. Fracture #4 appears to cross-cut #1 and to be cut by #2, in turn.

Most of the planar features consist of faint, whitish-gray zones, 2-3 mm wide, some branched:

	Relative Strike	Relative Dip Direction	Amount of Dip	
# 1	105°/285°	15°	30°	cut by #4
# 5	105°/285°	15°	35°	

Several other breaks have this approximate strike but varying dips. These two come from different parts of the core.

# 3	150°/330°	60°	60°	

Thin section 123-4Ba contains #3, which is a zone of broken-up quartz and feldspar crystals, but the band does not have the sheared look of #4. Here, variably sized, angular pieces of quartz and feldspar are scattered in a matrix rich in white mica. The boundaries of this zone cannot be precisely located in thin section, because the adjoining rock also has a

broken-up appearance. In areas clearly outside the band, however, the fragmented quartz and feldspar phenocrysts have more or less coherent outlines.

Thin section 123-4Ba also contains a series of calcite + white mica ± titanite ± TiO_2 veinlets, mostly ≤10 mm in length, that may possibly postdate #3. The wider parts of these veins are calcite-rich and the narrower parts are rich in white mica. Most of these have one of two, nearly perpendicular orientations, either in the range 80°/260° to 110°/290° or 160°/340° to 195°/15°.

146-4 (Well A)

This entire piece of core has been fractured, and thin, short, red-lined cracks extend in all directions in thin section. The principal fractures/veins visible on the core surface are grouped by appearance:

	Relative Strike	Relative Dip Direction	Amount of Dip	
# 1	30°/210°	300°	70°	Thin section 146-4a
# 3	50°/230°	140°	≈75°	Thin section 146-4b

These two breaks are marked by a series of white and green mineral deposits, connected by faint lines.

	Relative Strike	Relative Dip Direction	Amount of Dip	
# 2	10°/190°	280°	65°	Thin sections 146-4b, c

This is a well-defined, red-lined fracture that appears to cross-cut #3. Overall, it is relatively narrow with local development of anastomosing strands, but it widens at one point to a 1-cm thick, heavily brecciated zone.

4 20°/200° 290° 40° Possibly associated with #2 and with almost the same strike and dip direction, but the dip is shallower.

5 90°/270° 180° ≈20° Red-coated end of core sample

The sawcut surfaces reveal traces of red-lined cracks, striking 60°/240° on the cut for thin section 146-4a and 130°/320° on the one for 146-4b.

In thin section, the two green and white fractures (#1 and #3) contain elongate patches of calcite with borders of pale green chlorite. The patches are linked by narrow trails of grainy titanite. Quartz and feldspar phenocrysts cut by these bands are somewhat brecciated. Narrow

offshoots of fracture #1 and some associated subparallel traces are calcite-rich but also contain relatively abundant quartz (± feldspar) and fine-grained white mica (± chlorite).

The 60°-striking fracture visible in 146-4a is very narrow, but it extends for more than 20 mm and is marked by red-tinged opaques, fine-grained white mica, and minor titanite and calcite. Phenocrysts cut by this vein are offset slightly in a right-lateral sense.

In 146-4b and 4c, fracture #2 and its associated breccia zone predominate. The breccia consists of a series of large, angular pieces that are cemented together by calcite and Fe-oxides. Along the main break in 146-4b are narrow, sheared strands characterized by extensive grain-size reduction and some smearing out of opaque-looking material.

On the side of thin section 146-4b away from the heavily brecciated area, a number of quartz ± K-mica-bearing cracks were found that are ≤0.1 mm wide and generally no more than 1–2 mm in length. These cracks probably predate the fracturing associated with #2. A few patches of calcite in and around the quartz veins may be a later overprint.

156-9 (Well A)

The core contains a number of narrow, red-stained fractures, and the ends of the core sample are relatively straight, red-coated surfaces . Some fractures occur singly, whereas others are in complex groups. Measurable breaks are as follows:

	Relative Strike	Relative Dip Direction	Amount of Dip	
# 1	50°/230°	140°	50°	One end of core, smooth, red stained; small amounts of calcite and K-mica and a few feldspar (?) crystals are visible on the fracture surface in thin section (156-9a).
# 2	50°/230°	140°	30°	Intersects #1; it appears as a series of discontinuous, wavy, Fe-stained cracks in thin section (156-9a).
# 6	30°/210°	120°	≈40°	Smooth surface at other end of core; red stained.
# 5	100°/280°	10°	≈35°	Irregular, possibly composite break where core came apart in the middle of the sample; red stained.

	Relative Strike	Relative Dip Direction	Amount of Dip

# 7	40°/220°	130°	≈85°	Nearly vertical, intersects #5. In thin section (156-9b) it appears as a 1.5–3.5-mm wide brecciated zone, partly edged by bands of Fe-oxide. New minerals include abundant K-mica and some titanite, but little calcite.
# 4	70°/250°	≈340°	≈20°	Complex group of fractures, red stained, anastomosing.
# 3	90°/270°	180°	70°	Messy, discontinuous, possibly multiple breaks; intersects #4.
# 8	0°/180°	90°	≈30°	Very irregular

The thin sections reveal a more varied array of fractures and sheared or brecciated zones than is visible on the core surface. They can be grouped as follows:

Relative Strike

≈50°/230° Bands of brecciated or ground-up material that have more or less the same orientation as #1 and #2. They display a wide range in the amount of grain-size reduction — some contain many large, angular pieces, whereas others are more uniformly fine-grained. Most of these zones look fresh (that is, ground down but not altered), but one band is partly recrystallized to a groundmass of fine-grained, interlocking quartz and feldspar, along with fine-grained white mica and medium-grained titanite.

155°/335° – 170°/350° A prominent group of narrow veinlets containing white mica + quartz and/or feldspar. Individual veins are generally ≤1.5 mm long, but groups of them may extend for ≈10 mm. The quartz/feldspar crystals grow in from the sides of the vein, and the center is filled with fine-grained white mica oriented subparallel to the walls. Some feldspars cut by these cracks are slightly brecciated. Two relatively narrow shears in 156-9b have this orientation.

10°/190° – 25°/205° Many of these filled cracks are very similar to the 155°-trending cracks described above, but this group tends to be wider (to about 0.3 mm), longer, and more heavily brecciated. Prominent offshoots of fracture #1 have this orientation for about 5 mm, after which they bend to about 155°. Some of the cracks contain splotches of calcite, but the calcite may be a later mineral.

95°/275° This is an unusual-looking set of 3 or 4 long cracks. They are faint and discontinuous in places, and they also bend around somewhat. Portions of the cracks are partly open, containing only scattered, coarse-grained titanite and opaque grains and a few small, pointed crystals of feldspar or quartz. Where filled, the cracks are characterized by a central band of dark, grainy material surrounded on either side by tuff that is lighter than normal. Two of these veins offset slightly to the right some quartz-feldspar veinlets of 120°–130° strike.

Relative Strike	
120°/300°	Sets of moderately narrow, discontinuous or en echelon calcite veins up to about 5 mm in length. These veins are clustered together well away from most of the other veins, but one of them cross-cuts a 155°-striking brecciated band.

173-6B (Well A)

	Relative Strike	Relative Dip Direction	Amount of Dip	
# 4	90°/270°	180°	20°	
# 6	110°/290°	200°	5°	
# 5	130°/310°	220°	10°	

The core came apart along these unmineralized, nearly horizontal, slightly wavy surfaces. They may have formed as the core was brought to the surface, and they are not included in the stereonet plot for 173-6B (see text).

#1a	0°/180°	- -	Vertical	
#1b	10°/190°	- -	Vertical	

These two breaks are faint and narrow, but they can be followed for ≥20 cm on the core surface. Their cross-sections on the sawcut surfaces are very irregular and discontinuous, with many splays. One surface has a faint greenish cast. Other, more poorly defined fractures may have this same orientation. Fracture #1a is contained in thin section 173-6Ba, which reveals its numerous anastomosing branches and splays. The cracks contain at most a few phyllosilicates (the probable source of the greenish tinge). A lithic fragment cut by one crack is not offset.

# 7	70°/250°	340°	80°	Very faint; not very long.

Both thin sections contain a series of cracks whose orientations are similar to #7. Such cracks are generally very short, commonly ≤1 mm, and contain white mica ± quartz (± feldspar?). A few discontinuous cracks total several mm in length.

The core contains a red-stained section, about 15 cm long, with very irregular and wavy edges. Within this zone are two white, filled fractures:

	Relative Strike	Relative Dip Direction	Amount of Dip

2 140°/320° 230° 70° A lithic fragment and the border of the red-stained region cut by this fracture both indicate 4-5 mm of reverse slip (hanging wall up). The fracture looks sheared in thin section (173-6Bb). It is of variable width, exceeding 2 mm where it passes around large rock fragments. Quartz and feldspar phenocrysts incorporated into the fracture are ground-up and look partly recrystallized. Some calcite is present in the sheared band, and replacement of the tuff by calcite is most abundant in the vicinity of this break.

3 160°/340° 250° 30° Poorly defined on one side of core.

5-19 (Well B)

Fractures measured on the core sample are grouped by orientation, as follows:

	Relative Strike	Relative Dip Direction	Amount of Dip	
# 6	140°/320°	50°	85°	Irregular
# 4	140°/320°	230°	80°	Wide zone of slightly sheared-looking rock with numerous strands of titanite; thin section 5-19a.
# 7	≈155°/335°	- -	Vertical	Thin section 5-19b
# 8	≈175°/355°	- -	Vertical	Thin section 5-19b

The sawcut surface for thin section 5-19b reveals a number of fracture traces with the approximate orientation of #7 and #8. They appear as irregular multiple traces that may offset shallower-dipping cracks. Similar-looking fractures visible in the two thin sections span the entire range of orientations of these four breaks. They commonly occur in groups and contain titanite + chlorite + calcite ± K-mica ± quartz ± pyrite. Individual veins can be as much as 3 mm wide; a few narrower ones are principally pyrite-bearing.

	Relative Strike	Relative Dip Direction	Amount of Dip	
# 3	90°/270°	180°	50°	Filled with white minerals; disappears where intersects #4.
# 5	100°/280°	190°	40°	The sample came apart along this crystal-lined surface, which may be a composite of differently oriented fractures.

	Relative Strike	Relative Dip Direction	Amount of Dip

	Relative Strike	Relative Dip Direction	Amount of Dip	
# 2	115°/295°	205°	≈60°	Irregular, lined with white

minerals. Offshoots of the titanite + chlorite + calcite fractures described above are subparallel to #2, as are some narrow, wispy strands of titanite (± white mica ± chlorite). May be cross-cut by #7 or #8.

	Relative Strike	Relative Dip Direction	Amount of Dip	
# 1	45°/225°	135°	≈45°	A group of relatively straight,

white-lined cracks; the rock nearby is red-stained.

As seen in thin section, some quartz + calcite + K-mica-bearing fractures ≤5 mm in length have orientations similar to #1.

Observed only in thin section:

Relative Strike	
55°/235° – 65°/245°	A set of narrow, chlorite + white mica-filled veinlets in thin section 5-19b have this orientation; all are ≤3 mm in length. Corresponding veinlets in 5-19a are more varied in composition, containing white mica alone, quartz alone, or quartz + white mica. One of the latter may be cut off by a 90–115°-trending fracture.

12-4 (Well B)

The core sample contains three main sets of fractures grouped by strike and dip directions. First group:

	Relative Strike	Relative Dip Direction	Amount of Dip	
# 1	20°/200°	110°	50°	The core came apart along this

relatively straight, smooth fracture. The side of the break visible in thin section 12-4b is a wide (to ≈3 mm), sheared-looking zone. Phenocrysts caught up in it are variably ground down, and aligned K-mica defines a slight foliation. The edge of the zone is marked by a line of pyrite + titanite ± allanite (± epidote?). Also associated are patches of adularia + quartz + pyrite that also contains numerous voids.

#6,7	35°/215°	125°	20°	Two parallel fractures, about 5 cm

apart, filled with gray and white minerals. Possibly cross-cut by other fractures.

The second and third groups have similar strikes but dip in opposite directions. Second group:

	Relative Strike	Relative Dip Direction	Amount of Dip	
# 3	115°/295°	205°	20°	Mineralized end of core sample
# 8	90°/270°	180°	50°	A pair of narrow, filled fractures associated with patches of calcite. Both appear to crosscut one of the #2 fractures and offset it slightly in a reverse (hanging wall up) direction.

Third group:

	Relative Strike	Relative Dip Direction	Amount of Dip	
# 4	100°/280°	10°	50°	Wide, filled with white mineral, probably calcite; may be similar to #1.
# 5	120°/300°	30°	55°	Filled with white mineral (calcite?); possibly cross cut by #4.
# 2	145°/325°	55°	65°	Set of three sub-parallel fractures, all lined with calcite; one is crosscut by the #8 fractures.

Many other short veinlets, probably filled with calcite, are visible on the core surface. They can be traced only partway around the core.

The thin sections contain numerous short, discontinuous veins of calcite + titanite + white mica, and in some cases adularia + quartz. They mostly follow the trend of the 100°- and 120°-striking fractures described above, although narrow veinlets containing white mica can have any orientation. The K-micas generally are oriented roughly perpendicular to the sides of the veins. One band of very fine-grained adularia + quartz, similar in appearance to those found at deeper levels in well B, strikes approximately parallel to the mineralized end of the core sample (#3). In addition, approximately 5-mm-long bands containing adularia, quartz, and many void spaces are oriented in the range 150°/330° to 180°/0°.

29-28 (Well B)

The entire piece of core is heavily brecciated and extremely porous, and through-going cracks or fractures cannot be identified. A few minor, filled cracks are visible in thin section, but these are confined to individual fragments in the breccia. They consist either of narrow, wavy bands of titanite, usually associated with chlorite, that are no more than a few mm long, or short, narrow calcite veins.

60-3 (Well B)

Both ends of the core are mineralized, and the core came apart along a third mineralized surface:

	Relative Strike	Relative Dip Direction	Amount of Dip	
# 5	90°/270°	0°	≈20°	One mineralized end
# 9	70°/250°	160°	≈35°	Irregular surface at other end; cuts a large lithic fragment. The surface is thinly coated with pyrite and a white mineral.
# 1	35°/215°	305°	55°	Mineralized surface where sample came apart.

Three other fractures have approximately the same strike and dip direction as #5, although the amount of dip is variable:

	Relative Strike	Relative Dip Direction	Amount of Dip	
# 4	95°/275°	≈5°	≈70°	Jagged narrow break, only partly filled. Visible in thin section 60-3b, it contains adularia + quartz + anhydrite + pyrite, along with numerous large pore spaces. In narrower parts, the vein-filling minerals are fractured parallel to the sides.
# 2	100°/280°	≈10°	≈30°	5–8 mm wide, gray-colored, cherty-looking zone, with a darker gray band along each side. In thin section (60-3a), it appears to be a composite of newly crystallized adularia + quartz, fine-grained recrystallized groundmass, and overgrowths/alteration of igneous phenocrysts and clasts. The outer edges are marked by wide bands of titanite + allanite. Within this wider band are narrower, lighter-colored, partly open veins of medium-grained adularia and some anhydrite. Fine-grained bands such as #2 may represent recrystallized versions of the sheared zones found in well A.

	Relative	Relative

	Strike	Dip Direction	Amount of Dip	
# 3	100°/280°	≈10°	≈50°	Narrow but well defined; similar in appearance to one of the darker gray edges of #2. In thin section (60-3b), it forms a wavy path of grainy, dark titanite + pyrite, with large lozenges of calcite spaced at intervals. This break appears to be cut by veins of adularia + quartz with 0°/180° and 120°/300° trends.

Other fractures include:

	Relative Strike	Relative Dip Direction	Amount of Dip	
# 7	45°/225°	≈135°	≈5°	Partly open, narrow; intersects the open surface of #1 and is covered by the minerals deposited on that surface.
# 8	20°/200°	≈110°	≈35°	Pyrite-rich vein confined to large lithic fragment.
# 6	120°/300°	210°?	60°?	Very faint; may stop at #9.

One of the sawcut surfaces shows two additional sets of narrow cracks striking 70°/250° and 150°/330°. The 70° crack is at the other end of the core piece from #9; it is an irregular break that terminates at #2. The 150° cracks are narrow and only partly filled; they may cut across the 70° set.

Observed in thin section:

Relative Strike	
70°/250° – 90°/270°	Offshoots of #2
140°/320° – 160°/340°	Offshoots of #2

These two sets correspond to the narrow fractures that were observed along the sawcut surface.

10°/190° – 45°/225° Calcite vein orientations in 60-3a. They are relatively short and cut by offshoots of the main vein. In addition, some older-looking fractures with the same trends have a granulated look; they generally contain trails of dark titanite, partly recrystallized feldspar/quartz, patches of calcite, moderate amounts of chlorite, minor pyrite, and traces of K-mica.

75°/255° – 95°/275° Calcite vein orientations in 60-3b.

Relative Strike

≈170°/350° Relatively scarce veinlets, ≤1.5 mm long, that contain only fine-grained white mica. They may represent segregations of white mica in lithic fragments.

71-3 (Well B)

The core pieces contain at least one horizontal fracture (#3) lined with white minerals and other, inclined fractures as follows:

	Relative Strike	Relative Dip Direction	Amount of Dip	
# 2	30°/210°	300°	45°	Slightly wavy surface where core came apart; alternating greenish and sugary white patterns on surface, along with scattered pyrite crystals. Four fractures in thin section 71-3b with this orientation contain adularia + quartz + chlorite + titanite ± pyrite ± K-mica.
# 5	50°/230°	≈140°	≈50°	Narrow yellow-lined break, irregular, discontinuous; appears to stop where reaches #2.
# 4	100°/280°	≈190°	≈20°	Thin crack, partly healed
# 1	140°/320°	230°	≈70°	White and yellow filled vein. Thin section 71-3b cuts this vein, which is a fine-grained quartzofeldspathic band ≈4 mm wide. Within it is a series of narrower veins containing anhydrite along with some calcite and titanite, scattered pyrites, and small amounts of white mica that grow along the sides where the veins are relatively thin. Several less prominent bands in the thin section have a similar mineral assemblage, appearance, and orientation.
# 6	0°/180°	270°	50°	The sawcut piece for thin section 71-3a came apart along this fracture, lined with traces of calcite.

The thin sections also contain a number of other breaks, as follows:

Relative Strike	
80°/260° – 120°/300°	A series of calcite-bearing cracks of varying lengths and widths. One calcite vein also contains adularia + quartz, and a large, calcite-free vein contains quartz + adularia + pyrite (+ titanite + chlorite along narrower sections).
5°/185° – 35°/215°	A group of cracks generally characterized by the presence of chlorite and titanite. The rock adjoining one of these veins contains less disseminated dark, grainy material than elsewhere. Others are notable for apparent granulation and recrystallization of adjacent quartz and feldspar phenocrysts.

Relative Strike

140°/320° – 145°/325° Two titanite-bearing veins have this orientation. One is notable for also containing white mica and pyrite, K-mica being a relatively scarce vein-filling mineral in this piece of core.

85-4 and 85-6 (Well B)

The fractures visible in the core samples can be separated into groups, based on their dip direction:

	Relative Strike	Relative Dip Direction	Amount of Dip	
# 3	150°/330°	60°	40–45°	Partly open, lined with large crystals. Thin section 85-4b contains one surface of this fracture, which separated during cutting. The fracture surface is very irregular, with pockets of vein minerals in the depressions. In one place, large anhydrite crystals are surrounded by a succession from fine-grained to coarser-grained adularia. Small amounts of calcite + chlorite are present; one calcite patch is partly encased in a large anhydrite crystal. Large, clean titanite crystals and narrow, bladed allanite crystals extend from the side of the vein into the adularia zones.
# 7	165°/345°	75°	30°	Mineralized half-surface at the outer end of 85-6.
# 1	170°/350°	80°	60°	Separates 85-4 and 85-6; very irregular surface lined with a lumpy coating of fine-grained feldspar + quartz and some larger crystals. Possibly connects with #3.

	Relative Strike	Relative Dip Direction	Amount of Dip	
# 2	170°/350°	260°	40°(?)	Non-mineralized half-surface at outer end of 85-6, opposite #7.
# 4	10°/190°	280°	40°	About 2 mm wide, partly filled. As seen in thin section 85-4a, the vein is lined with fine- to medium-grained adularia + quartz, lumpy titanite and small, bladed allanite crystals, with large anhydrite crystals spanning open parts of the fracture. Narrow sections are completely filled. Some of the vein-filling minerals are cracked parallel to the sides of the fracture.

	Relative Strike	Relative Dip Direction	Amount of Dip	

# 5	25°/205°	- -	Vertical	Discontinuous; separates #7 and #2 at the end of 85-6.
# 6	105°/285°	- -	Vertical	Partly filled vertical crack; very faint.

A group of narrow quartz veinlets in thin section 85-4a have orientations similar to #5; other cracks containing quartz and/or white mica ± pyrite are oriented roughly parallel to #1 and #3. One of the cracks parallel to #5 may crosscut a K-mica-bearing veinlet with a strike similar to #3. The thin sections yield a few additional trends:

Relative Strike

60°/240° – 85°/265° Offshoots to fracture #4 and separate fractures with a similar vein-mineral assemblage.

0°/180° Several faint trends in 85-4b, defined principally by oriented white mica; all are found in a white-mica-rich zone (clast?). A few also contain pyrite, titanite, or quartz.

91-13 (Well B)

The core sample is quite vuggy. Apparently isolated cavities are scattered over the surface of the core; others are grouped into wide, porous, brecciated zones. Narrow cracks are also only partly filled, leaving small vugs.

	Relative Strike	Relative Dip Direction	Amount of Dip	
# 1	35°/215°	305°	30°	One mineralized end of sample. In thin section (91-13a), it is a wide, fine-grained band of adularia + quartz + titanite + chlorite.
# 3	≈80°/260°	≈350°	35°?	Very faint, narrow
# 2	95°/275°	5°	45°	Narrow, mostly filled
# 7	100°/280°	≈10°	≈40°	Very faint, discontinuous, irregular; narrow, partly open; may intersect #5.
# 6	125°/305°	215°	≈80°	Irregular; marked by large, mineral-lined vugs; perhaps brecciated. Intersects top end of sample; opening is covered by large anhydrite crystals.

	Relative Strike	Relative Dip Direction	Amount of Dip

4 0°/180° 270° 30° Thin section 91-13b. Shallow, wide, brecciated zone that stops at #5. The fragments of tuff are partly cemented together by adularia + quartz ± titanite, and the fragments themselves are partly recrystallized. Multiple generations of fragmentation could not be identified, but some of the adularia + quartz rims probably represent 2 or 3 episodes of crystal growth. Numerous calcite veins occur within the tuff fragments, but calcite forms essentially no part of the adularia + quartz assemblage.

5 0°/180° 270° ≈75° Variably wide, partly healed, vuggy. An irregular brecciated area extending to one side of #5 may possibly be the offset (8-10 cm reverse slip) equivalent of #4.

The thin sections also contain groups of cracks with distinctive mineral assemblages and/or textures:

Relative Strike

0°/180° – 90°/270° Most of the calcite veins in the various pieces of tuff in 91-13b are oriented somewhere in this wide range. Because all of these veins probably formed before the tuff was fragmented, this range may not represent their original orientations.

60°/240° – 100°/280° The principal break with this orientation is a relatively wide, only partly filled vein of coarse-grained adularia + quartz, with some coarse-grained calcite that crosses fracture #1 in thin section 91-13a. Several narrower veins of this type are also present.

115°/295 – 130°/310° A group of narrow, adularia + quartz-bearing veins (1–2 crystals wide) that are considerably coarser-grained than many of the other bands. One of these is an offshoot of #1.

In addition, a series of short, titanite-rich or titanite + chlorite-rich cracks occur in all orientations in 91-13a. Some also contain feldspar/quartz and others have small to moderate-sized vugs. In any one part of the thin section these veinlets have only one or two orientations.

122-3, 122-4, and 122-5 (Well B)

The three pieces of core sample comprising 122-3, 4, and 5 contain numerous fractured and mineral-lined surfaces. They are grouped below according to their apparent relative ages. First (oldest) group:

	Relative Strike	Relative Dip Direction	Amount of Dip	
# 6	10°/190°	280°	70°	Prominent sheared-looking band, characterized by a smeared-out zone of fine-grained dark material. As seen in thin sections 122-5b and 5c, this zone has been broken into elongate pieces aligned parallel to the strike. Relict quartz and feldspar phenocrysts generally are small and rounded. The various fragments are bound together by aggregates of fine-grained adularia + quartz + pyrite + titanite. The shear also looks to be cut by younger veins of adularia + quartz + chlorite. Calcite crystals in this zone have a corroded appearance and are partly rimmed by titanite. Sheet-silicate-rich bands within the zone are mixtures of chlorite + K-mica (chlorite partly replacing the K-mica?). The actual slip surface appears relatively narrow and straight.
# 12	155°/335°	245°	60°	Faint; disappears into the sheared dark bands of #6.
# 4	25°/205°	295°	80°	Partly filled with white minerals; possibly is an extension of #6.
# 3	20°/200°	110°	45°	Partly open, hard to follow trend; may stop at #4. As seen in thin section 122-3a, the vein is filled with adularia + quartz, with coarse-grained titanites along the sides and some void spaces in the center. Wider spots have pockets, off to the side, of very fine-grained adularia + quartz. In places, vein-filling minerals are cracked parallel to the sides.

These four fractures appear to be the oldest ones in the sample. Fractures #6, #4, and #12 may all be part of the same fracture system, and #3 may be older than #4.

Second (unknown age) group:

	Relative Strike	Relative Dip Direction	Amount of Dip	
# 5	15°/195°	285°	60°	Partly defines outer end of 122-3. Filled with white mineral; small, dark-colored (pyrite-rich?) lithics smeared out along it.

Relative Strike	Relative Dip Direction	Amount of Dip

	Relative Strike	Relative Dip Direction	Amount of Dip	
# 1 3	40°/220°	130°	50°	With #5, defines outer end of 122-3. Small, dark lithic fragments smeared out along it.

The timing of these two fractures relative to each other cannot be determined, and neither one comes close to any other fracture in the core sample.

Third (intermediate) group:

	Relative Strike	Relative Dip Direction	Amount of Dip	
# 8	110°/290°	≈200°	60°	Dense, brecciated zone, closely associated with #14.
# 1 0	115°/295°	25°	10°	Vuggy, filled parts are yellow-tinged. Similar in appearance to #14.
# 1 4	125°/305°	≈215°	≈10°	Very irregular, nearly horizontal, densely brecciated band, ≈2 cm wide. It offsets the fine-grained, dark zone of #6, and the breccia contains many fragments of the dark material. It is cross-cut in turn by #7. This breccia is very different from the porous breccias of 29-28 and 91-13.
# 9	170°/350°	80°	40°	Very vuggy in places. As seen in thin section 122-5b, it cross-cuts #6 and contains adularia + quartz + chlorite + titanite and numerous void spaces. It may also cross-cut #10, but this is not certain.

Fourth (youngest) group:

	Relative Strike	Relative Dip Direction	Amount of Dip	
# 7	100°/280°	≈10°	≈60°	Partly open, lined with tiny gray crystals. Filled part has a brecciated appearance. Cross-cuts #6; may also offset #14 in a normal sense (hanging wall down).
# 1 1	105°/285°	≈15°	≈65°	Very close to and possibly contemporaneous with #7. In thin section 122-5c, it appears as a band of brecciated tuff that heads away from sheared band #6 and also contains fragments of #6. The breccia is partly cemented with large anhydrite crystals in addition to fine-grained adularia + quartz + chlorite, but a lot of void space remains. This breccia is similar to those in 29-28 and 91-13.
# 2	110°/290°	≈20°	≈50°	Boundary between pieces 122-4 and 122-5. It is lined with a fine-grained mat of feldspar + quartz, with scattered anhydrite crystals on the surface.

	Relative Strike	Relative Dip Direction	Amount of Dip

# 1	120°/300°	≈30°	≈40°	Boundary between core pieces 122-3 and 122-4; mineralized with sintery mats of feldspar + quartz and greenish (chlorite?) patches . Fracture #6 reaches this end, and its trace is covered by the mineralization associated with #1.

49-5 (Well C)

Two roughly orthogonal fractures appear to be more or less contemporaneous and contain the same minerals. They both form mineral encrusted surfaces:

	Relative Strike	Relative Dip direction	Amount of Dip	
# 1	120°/300°	30°	≈60°	Vuggy, partly filled with minerals, found in middle of core; thin section 49-5b contains one surface of this fracture.
# 2	30°/210°	120°	75°	Mineral-lined fracture surface at top end; thin section 49-5a.

These two breaks do not intersect; the one fracture begins about where the other one ends. At the lower end of this piece of core, a complex mineralized surface may be a combination of these two orientations. As seen in thin section, the two fractures have the same mineral assemblage, dominated by quartz. Fracture #2 contains more calcite than #1; in #1, calcite is confined to a few small patches, one of them draped over some quartz crystals. Both fractures have obvious pyrite and K-mica on their surfaces; small amounts of titanite, allanite, TiO_2, and a trace of sphalerite were identified on fracture #1 by SEM.

The core also contains a series of subsidiary breaks; some have roughly the same strike as fracture #1, but the amount and direction of dip vary:

	Relative Strike	Relative Dip direction	Amount of Dip	
# 3	140°/320°	230°	≈75°	Multiple, anastomosing breaks
# 4	135°/315°	- -	Vertical	Discontinuous, irregular, anastomosing. Mineral deposits of fracture #2 cover this break at the point of intersection.
# 5	120°/300°	30°	80°	Faint, in vicinity of fracture #1

	Relative Strike	Relative Dip direction	Amount of Dip

# 6	90°/270°	0°	50°	One of a group of intersecting fractures at one end of the core.
# 7	70°/250°	340°	85°	Very faint, near fracture #1
# 8	0°/180°	90°	85°	Small sliver, partly filled with calcite; mineral deposits of #1 partly cover this fracture where they intersect.
# 9	80°/260°	- -	Vertical	Very faint; strike may vary a lot.

Fractures #3 and 4 are visible in thin section 49-5a. They intersect #2 at nearly 90° and they principally contain calcite, although all the other major vein minerals of fractures #1 and #2 are present, as well as some void spaces. Section 49-5a also displays a series of minor cracks with orientations subparallel to #3 and #4. Several of them contain at least some calcite, but the narrower and shorter ones have less calcite and more quartz and K-mica. In thin section 49-5b is a group of calcite-rich fractures that are subparallel to #1 across much of the section, but they bend around and eventually intersect #1.